Variability of radio and TeV emitting X-ray binary systems
The case of LS I +61°303

Dissertation
zur
Erlangung des Doktorgrades (Dr. rer. nat)
der
Mathematisch-Naturwissenschaftlichen Fakultät
der
Rheinischen Friedrich-Wilhelms-Universität Bonn

vorgelegt von

Lisa Zimmermann

aus
Marburg

Bonn 2013

Angefertigt mit Genehmigung der Mathematisch-Naturwissenschaftlichen Fakultät der Rheinischen Friedrich-Wilhelms-Universität Bonn

1. Gutachterin: PD. Dr. Maria Massi
2. Gutachter: Prof. Dr. Norbert Langer

Tag der Promotion: 24.7.2013
Erscheinungsjahr: 2013

Summary

X-ray binaries contain a compact object, a black hole or a neutron star, and a normal companion star. They emit strongly in X-rays, because the compact object accrets material from its companion. Some of them emit as well in radio, they are called microquasars, because they have the same ingredients as quasars, just on a much smaller scale. In a quasar, a supermassive black hole feeds from its surrounding galaxy and ejects ultra-relativistic material in so-called jets, which emit synchrotron emission in the radio regime. An even more exclusive club of X-ray binaries, only ∼5, also emits in gamma-rays. The nature of these gamma-ray binaries is strongly debated. Microquasar scenarios (all gamma-ray binaries have been detected in radio) were brought forth and a millisecond pulsar scenario. LS I +61°303 is special even among these gamma-ray binaries, first, because it emits strongly in radio, showing periodic outbursts every ∼26.5 days and secondly because of its strong and also periodic high and very high energy emission. In this thesis are studied i) the variability of the radio flux density and morphology in the gamma-ray binary LS I +61°303 and ii) the connection between the variable radio and high energy emission in order to better understand the nature of this source.

Concerning the radio and high energy connection, it is shown that earlier analysis could not have identified certain characteristics in high energy data due to the usage of too large time intervals of data with possibly different spectral information. These missing characteristics were taken as evidence against a microquasar scenario. Using radio spectral index data from LS I +61°303 and taking into account the radio periodicities, the affects of using too large time intervals of high energy data can be determined, because in a microquasar a clear connection between these two emission regimes is expected. Motivated by these analysis, high energy data was re-examined with respect to these periodicites. Preliminary results indicate that the spectral information of the time intervals are indeed different. Furthermore, very high energy data from LS I +61°303 show a correlation with X-ray data reminiscent of blazars, i.e. a microblazar. This shed a new light on the possible emission processes in a microquasar scenario for LS I +61°303, and led to a re-examination of archived data from the Very Long Baseline Array (VLBA) of LS I +61°303 in search of more microblazar clues. With an improved data reduction the radio morphology shows two- and one-sided structures with fast switches and accompanied by changes in the position angle. Furthermore, the astrometry showed that the flux density peaks of the successive maps trace a clear ellipse with a period of ∼27 days. These can be interpreted in a microquasar model as the core of a precessing steady jet with a small viewing angle, i.e. a microblazar. Total flux density and spectral analysis show behaviour expected for a microquasar and modelling of gaussian components of the two-sided radio structures give an estimate of the jet velocity.

The affects of precession on the radio flux and spectral index in addition to those expected from accretion called for a dense spectral coverage of the flare in LS I +61°303. This was obtained during its outburst at the end of March 2012 with the Effelsberg 100m telescope. A complete flux and spectral evolution of the radio flare with a sampling rate of 12 hours and at least four frequencies yield a quiescent and a complete flare spectrum. The flare spectrum is flat, suggesting a steady conical outflow, a steady jet, and is followed by several optically thin subflares, reminiscent of shocks. One of these shocks is possibly correlated with a flux rise seen in the gamma-ray regime with Fermi-LAT (Large Area Telescope).

Zusammenfassung

Röntgendoppelsterne bestehen aus einem kompakten Objekt, einem schwarzes Loch oder einem Neutronenstern, und einem normalen Begleitstern. Sie emittieren starke Röntgenstrahlung, die durch Akkretion von Materie auf das kompakte Objekt entsteht. Einige Röntgendoppelsterne emittieren auch Radiostrahlung, sie heißen Mikroquasare, weil sie aus denselben Zutaten bestehen wie Quasare. In einem Quasar akkretiert allerdings ein supermassives schwarzes Loch Materie von der es umgebenden Galaxie und schleudert in Form von so genannten Jets ultrarelativistische Teilchen hinaus ins All, welche dann Synchrotronstrahlung im Radiobereich abgeben. Ein noch kleinerer Teil der Röntgendoppelsterne, nur ∼5 sind bestaetigt, emittieren noch zusätzlich Gammastrahlung im GeV und TeV Bereich. Die Natur dieser Gammadoppelsterne ist sehr umstritten. Sowohl Mikroquasar Szenarien wurden vorgeschlagen (alle Gammadoppelsterne emmittieren auch Radiostrahlung), als auch ein Millisekunden-Pulsarmodell. LS I +61°303 nimmt hierbei einen speziellen Platz ein, weil es zum einen sehr stark im Radio- und Gammabereich emittiert, und zum anderen seine Strahlung periodisch ist. Alle 26.5 Tage zeigt LS I +61°303 einen starken Ausbruch im Radiobereich und auch im GeV und TeV Bereich ist die Strahlung moduliert. In dieser Arbeit wird sowohl die i) Variabilität der Radiostrahlung von LS I +61°303 und ihre Morphologie untersucht als auch ii) die Verbindung zwischen der variablen Radio- und Gammastrahlung, um ein besseres Verständnis der Strahlungsprozesse in dieser Quelle zu ermöglichen.

Es wird gezeigt, dass aufgrund der Verbindung zwischen Radio- und Gammastrahlung (insbesondere sanfte Gammastrahlung), bestimmte Informationen nicht entdeckt werden konnten, weil zu große zeitliche Datenintervalle betrachtet wurden, die unterschiedliche spektrale Eigenschaften aufweisen könnten. Diese fehlenden Informationen wurden als Ausschlusskriterium für ein Mikroquasar Modell für LS I +61°303 gesehen. Nimmt man aber spektrale Informationen aus dem Radiobereich zur Hand und achtet auf die Periodizitäten, ist es moeglich den Einfluss der Verwendung von zu großen zeitlichen Datenintervallen abzuschätzen, da bei einem Mikroquasar die sanfte Gammastrahlung und die Radiostrahlung aneinander gekoppelt sind. Mit Hilfe dieser Informationen wurden vorhandene Gamma-Daten neu analysiert und erste Ergebnisse weisen darauf hin, dass die Zeitintervalle tatsächlich unterschiedliche spektrale Eigenschaften besitzen. Darüberhinaus zeigen Gamma-Daten von LS I +61°303 eine Korrelation mit Röntgendaten, die an Blazare erinnert, d.h., es könnte sich bei LS I +61°303 um einen Mikroblazar handeln. Das würde neue Möglichkeiten für die Strahlungsprozesse in LS I +61°303 bieten. Aus diesem Grund wurden archivierte Daten des Very Long Baseline Arrays (VLBA) neu untersucht, um nach weiteren Hinweisen auf ein Mikroblazar Szenario zu suchen. Durch verbesserte

Datenreduktion, wurde ein höheres Signal-zu-Rauschen erzielt, wodurch in der Radiomorphology ein- und zweiseitige Komponenten entdeckt wurden, die sich schnell abwechseln. Zusätzlich offenbarte die Astrometrie der höchsten Flussdichten in den Radiobildern, dass diese eine Ellipse bilden, mit einer Periode von ~27 Tagen. In einem Mikroquasar Modell kann diese Ellipse durch einen präzidierenden Jet erklärt werden, der nur einen kleinen Winkel mit unserer Sichtlinie einschließt, d.h. ein Mikroblazar. Die Analyse der Flussdichten und des Spektralindex unterstützen ebenfalls das Mikroquasar Modell. Zusätzlich wird noch eine erste Abschätzung der Geschwindigkeit des Jets vorgenommen.
Sowohl Akkretion als auch Präzession sollten demnach bei der Analyse von Radiolichtkurven eine Rolle spielen. Um die Einflüsse genauer zu untersuchen wurde mit dem Effelsberg 100m Radioteleskop eine dichte Breitband Spektralanalyse des Radioausbruchs im Maerz 2012 durchgeführt. Alle 12 Stunden wurde das Spektrum von LS I +61°303 und so am Ende ein komplettes Radiospektrum des Ausbruchs und seiner Entwicklung gemessen. Das Spektrum des Ausbruchs ist flach, was auf einen langsamen konischen Jet hindeutet. Zusätzlich kommt es vorher und nachher zu mehreren kleinen Ausbruechen, die optisch dünn sind und auf Schocks hindeuten. Einer dieser kleinen Ausbrüche hat möglicherweise einen korrelierten Anstieg im GeV Bereich, der mit dem Fermi-LAT (Large Area Telescoope) beobachtet wurde.

Contents

List of Figures

List of Tables

Chapter 1

Introduction

1.1 X-ray binaries and microquasars

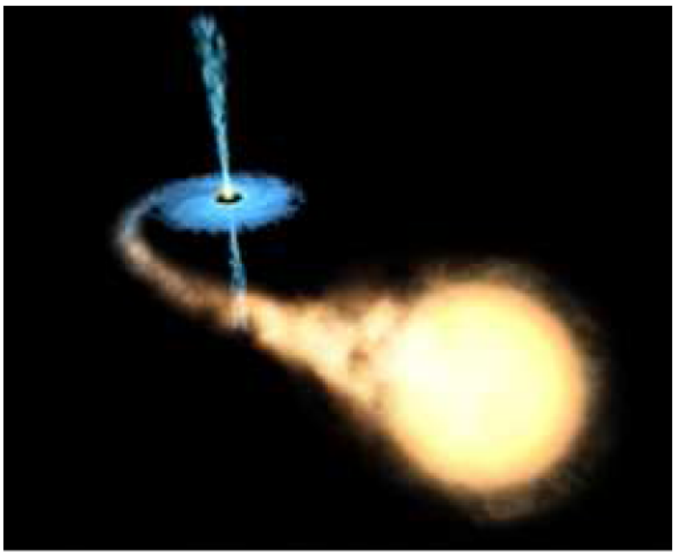

Figure 1.1: Artistic view of the accretion process in microquasars and the formation of radio jets (Mirabel 2010).

X-ray binaries are binary systems containing a star and a compact object (neutron star or black hole). Either via Roche-lobe overflow or via wind accretion, matter is accreted onto the compact object forming an accretion disk around it as shown in Fig. 1.1. This disk is heated by viscous forces to millions of Kelvin and thereby radiating strongly in X-rays. X-ray binaries were discovered in the 1960s as very bright X-ray sources. The only physical process known to be efficient enough to provide these energies is accretion, which, similiar as for the discovery of supermassive black holes, then lead to the scenario of an accreting compact object. Compared to

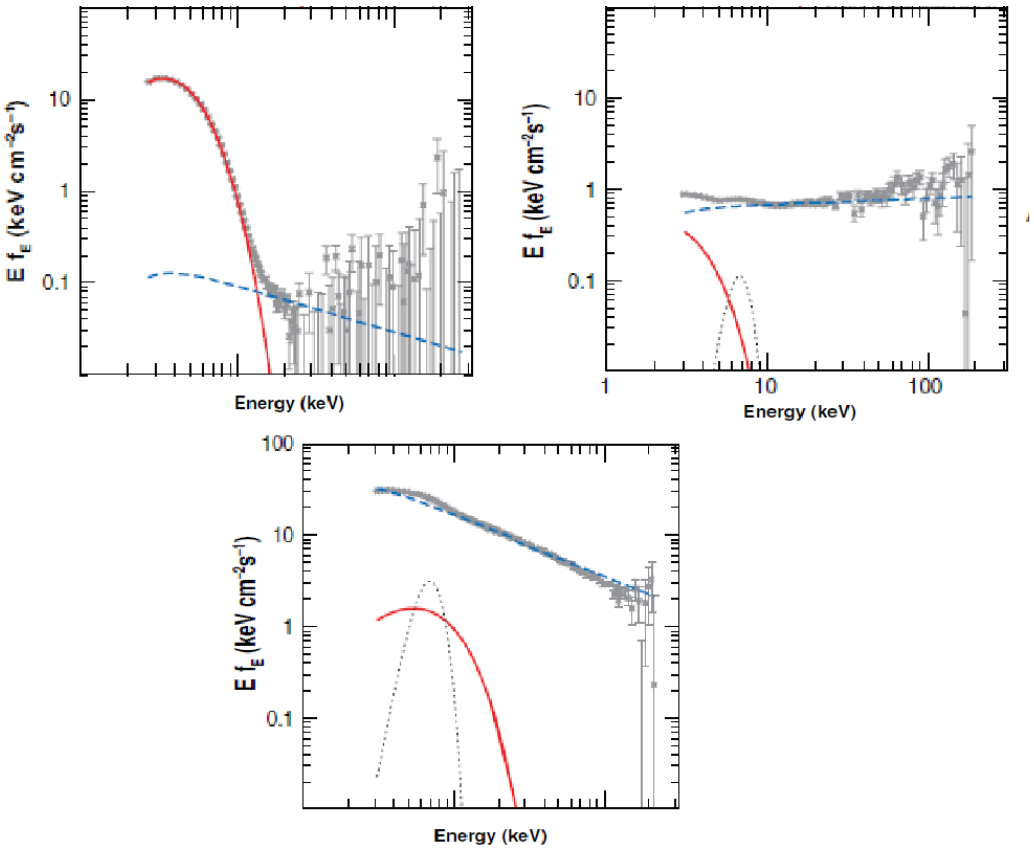

Figure 1.2: X-ray energy spectra for the high-soft (top left) , the low-hard (top right) and the transitional (steep power law) state (bottom) from the source GRO J1655-40 (Fender et al. 2004).

the analysis of supermassive black holes, these systems have a huge advantage. They are binary systems and the masses of the two stars, i.e. the compact object, can therefore, in principle, be determined through simple Keplerian laws. Also, the nature of the companion star can be discovered through spectroscopic analysis, and then the evolution of these systems can be analysed.

X-ray binaries are generally categorized by the mass of the companion star as either low (companion star earlier than B) or high mass (O or B type) X-ray binaries. Their X-ray emission shows a variety of spectral and timing characteristics, which have been summed into so called X-ray states (Fender et al 2004, Belloni 2010). These X-ray states appear in a certain cycle. The length of this cycle and the length of the states vary strongly across different sources and sometimes not all states are reached (failed state transitions, see Pottschmidt et al 2001). Furthermore, the borders between these states are not sharp. Nevertheless, some main characteristics apply for most of the sources most of the time. The main states are the high soft state, the low hard state and the transitional (steep power law) state. The physical explanation is the state the accretion disk is in, the spectral features of the states are shown in Fig. 1.2. The high soft state is dominated by soft X-rays from the accretion disk, which stretches close to the compact object

and emits a black-body spectrum with kT∼1-3.5 keV. In the low hard state, the disk is probably truncated, yielding only a mostly negligible black-body component, the spectrum is dominated by hard X-ray emission showing a power law with a spectral index of $\Gamma \approx 1.7$ (1.4 - 2.4) and a high energy cut-off around 100 keV (around 60 keV for a neutron star). The hard X-rays could come from a hot advection dominated coronal flow around the compact object. In the transitional state, which leads from the low hard to the soft state, a power law without a cut-off and spectral index of $\Gamma \approx 2.5$ is observed. The low hard and the transitional state are further characterized by quasi periodic oscillations (QPO). These QPOs disappear in the soft state (Belloni 2010). There exists a fourth state, the quiescent state, which is essentially the same as the low hard state, but with much fainter X-ray emission. It can preceed the low hard state.

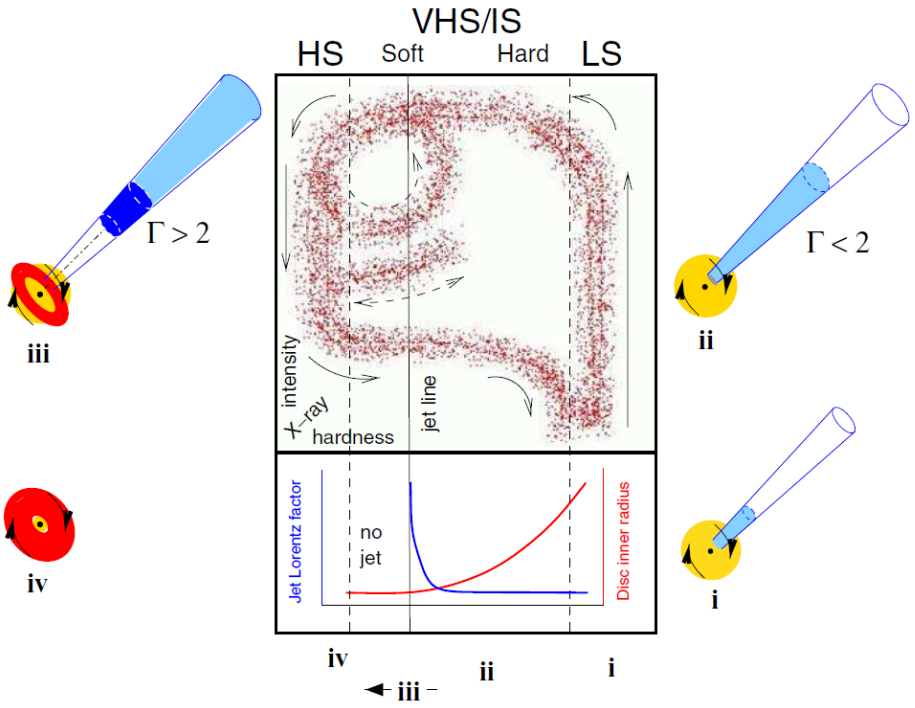

Figure 1.3: Sketch of the unified X-ray states model for radio jets. At the bottom right of the figure is the quiescent state (i), which has a low luminosity in hard X-rays and some radio emission from a steady jet. Then the intensity in hard X-rays increases as the source enters the low/hard state (ii), along with increasing radio emission from a stronger but still slow jet (small jet Lorentz factor). The accretion disk is truncated. In the steep power law state (depicted as (iii) VHS/IS) the X-rays start to become softer and the jet becomes transient with a high velocity. The jet production ceases as the source crosses the jet line. In the high soft state (iv) the X-rays are soft and the accretion disk reaches the last stable orbit (Fender et al. 2004).

Around 300 X-ray binaries are known in our galaxy. Around 30 of them also emit more or less strongly in radio. This radio emission is synchrotron emission, generated by relativistic particles

gyrating in a magnetic field. This emission is also present in supermassive black hole systems, quasars, creating large scale jets. Such jets are as well created in the radio emitting X-ray binary systems, shown in Fig. 1.1, which is why the are called microquasars.

The jets can be resolved directly sometimes, presenting themselves either as steady jets, centered onto the compact object, or as transient jets, where the emission is detached from the center (Fender et al 2004, Gallo 2010). These two radio states can also be distinguished by looking at the radio spectrum. The steady jet has a flat or inverted spectrum ($\alpha \sim<0$, with $S \propto \nu^{\alpha}$), which arises due to the superposition of synchrotron spectra with different peak frequencies along the decaying magnetic field in a conical jet (see Fig. 1.4). The transient jet in contrast has an optically thin steep spectrum (α <0) (Fender et al 2004). The emission comes only from a thin layer of a plasmoid or from behind a shock front (Gallo 2010, Tuerler 2011).

The X-ray states and the radio states are coupled as shown in Fig. 1.3. The steady jet is seen during the low hard state, the transient jet during the transitional state. This means that the radio states follow as well a cycle, coupled to the X-rays. This is established in the unified X-ray states model with radio jets shown in Fig. 1.3 (Fender et al 2004). With respect to the physical scenario, it is suggested, that the creation of a jet marks the onset of an accretion event in the low hard state, the jet carries away rotational momentum thereby allowing for matter to be accreted onto the compact object (Fender 2010, Gallo 2010). The transient jet could then be created by a shock, which destroys the steady jet and marks the begin of the radio-quiet high soft state. The radio emission coming from the jet is widely accepted, the origin of the X-rays are attributed mostly to the accretion disk, but also by some authors to synchrotron emission, i.e. to the jet (Markoff et al 2005, Markoff 2010).

1.2 Gamma-ray binaries

Early on, some of the X-ray binaries have also been detected in gamma-rays, LS I +61°303 was e.g. detected already in 1977 by Cos-B (Gregory & Taylor 1978). The club remains quite exclusive though, even with the new generation instruments such as MAGIC, VERITAS, HESS and Fermi-LAT, only seven gamma-ray binaries have been found. Only three of these sources show modulated emission at high (GeV) and very high (TeV) energies: LS I +61°303, LS5039 and PSR B1259-63 . All three of them emit in radio as well.

The origin of the gamma-rays are explained as either leptonic or hadronic. In the leptonic model, inverse Compton scattering of relativistic electrons on external photons from e.g. the donor star (external inverse Compton (EIC)) or on synchrotron photons fromt the jet (synchrotron self-Comptonization (SSC)) produce the observed gamma-ray emission. In the hadronic model, gamma-rays are produced by hadronic interactions. Pions are created by pp-interactions or pion photoproduction and then decay into two gamma-rays.

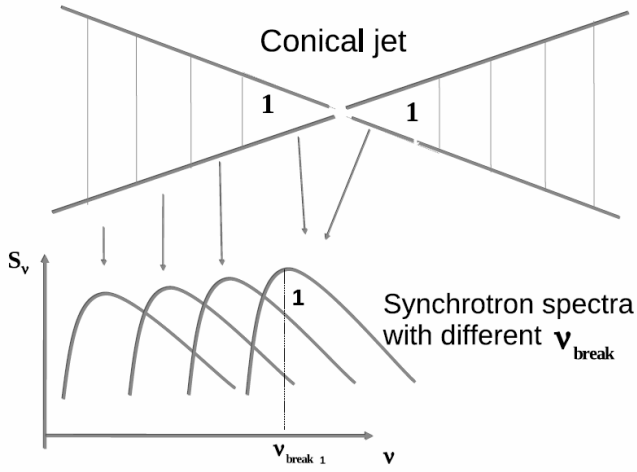

Figure 1.4: Each segment of the conical jet contributes a synchrotron spectrum with a peak frequency decreasing from the center. The observed spectrum is a composite spectrum with a flat/inverted slope (Massi 2011a).

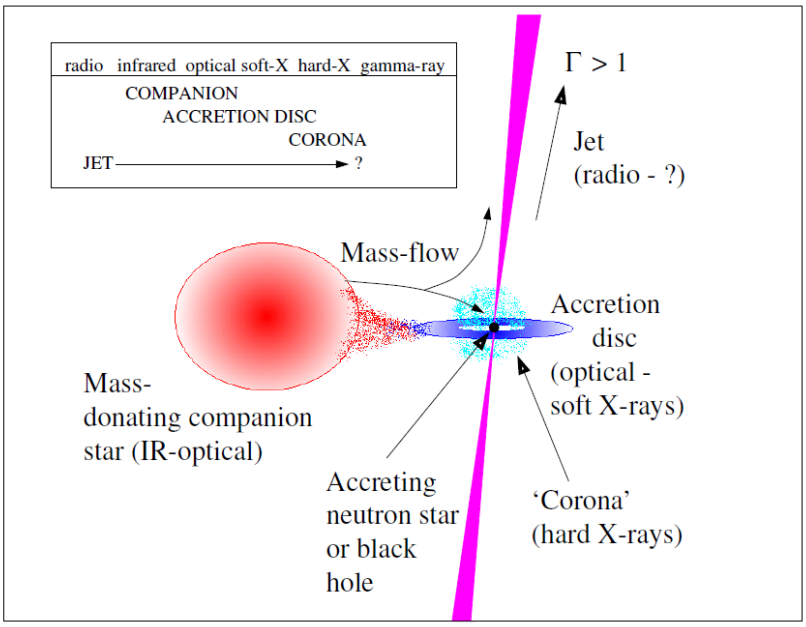

Figure 1.5: The typical components of a microquasar and the three possible external photon fields for inverse Compton scattering are shown: The mass flow from the donor star, the accretion disk and the corona (Fender & Maccarone 2004).

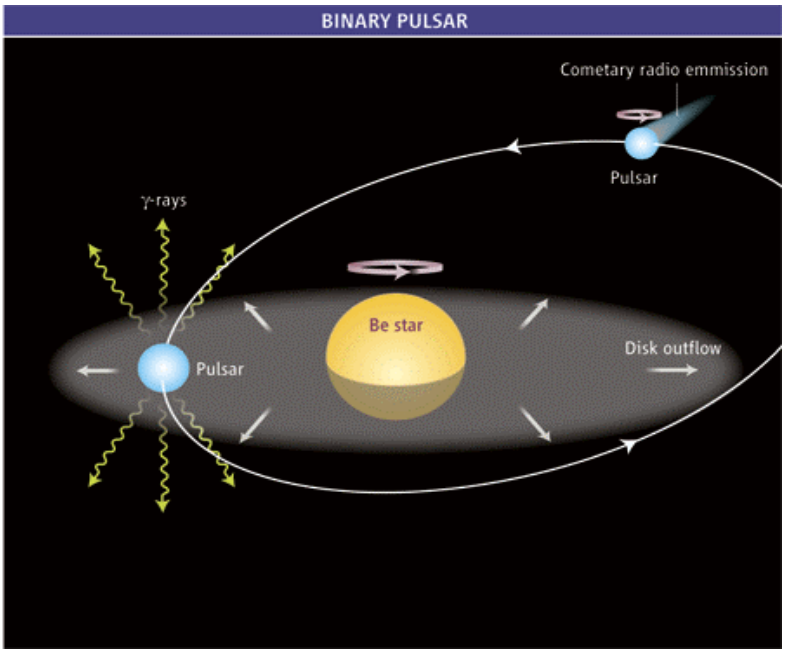

Figure 1.6: Sketch of gamma-ray emission in a binary pulsar scenario. The cometary tail of the pulsar, produced by the collision of its fast wind with the stellar wind from the companion star, always points away from the orbit. At periastron electrons, accelerated in the shock front between the pulsar and the stellar wind, upscatter UV photons from the companion to gamma ray energies (Mirabel 2006).

In order to discover the origin of the gamma-rays, these systems must first be understood. The nature of the gamma-ray binaries is a matter of strong debate, though. Especially concerning the three main sources, only one is identified unambiguously. PSR B1259-63 is a special case of an X-ray binary, where the X-rays and the radio emission do not come from accretion and ejection of material, but from a shock site, created by the collision of the wind from the companion with an ultra-relativistic wind from the compact object, which is a young, fast rotating (millisecond) pulsar (the scenario is shown in Fig.1.6) (Johnston et al 2005). PSR B1259-63 emits pulses, which are supressed for approx. 20 days around periastron due to free-free absorption (Johnston et al 2004). For LS I +61°303 and LS5039 also microquasar models have been proposed, with a scenario as shown in Fig. 1.5, where the gamma-rays arise either from EIC or from SSC. A microquasar model for LS I +61°303 will be discussed in detail in the following chapters.

1.3 LS I +61°303

LS I +61°303 consists of a compact object of unknown nature orbiting a massive companion star with a period of 26.495 days (Gregory et al 1999, Gregory et al 2002). From optical spectroscopy it is known that the companion is a rapidly rotating BO V star with a mass of 10-15 solar masses (Hutchings & Crampton 1981). Such a star exhibits a slow equatorial outflow forming a thin decretion disk and has a fast polar wind. The accretion flow onto the compact object is fed by the decretion disk. The nature of the compact object could not be established through these measurements yet. Due to the ambiguity of different observations, the inclination range of the system is quite large, (i=10-50°) allowing for a mass-range of 1.4-4 solar masses, so either a neutron star or a black hole (Hutchings & Crampton 1981, Casares et al 2005, Grundstroem et al 2007,Aragona et al 2009). The orbit of LS I +61°303 is eccentric (e=0.54-0.7)

LS I +61°303 has been detected and is variable across the whole electromagnetic spectrum and on many different time scales (see e.g. Taylor et al 1982, Paredes et al 1994, Mendelson et al 1994, Zamanov et al 1999, Paredes et al 1997, Abdo et al 2009, Acciari et al 2009). Two radio periodicties were discovered, one corresponding to the orbital period, the other being of 4.6 years (Gregory et al 1999, Gregory et al 2002). The source exhibits a strong radio outburst each orbit around the phase of apastron Φ ~0.6 ($\Phi_{periastron}$=0.230.-0.275, Aragona et al 2009). The long period though modulates the exact orbital occurence and the strength of the outburst. The two radio periodicites have also been established at other frequencies. The orbital period is established at soft gamma-rays, X-rays and optical (H-alpha). The superorbital period is seen in optical (H-alpha) (Zamanov et al 1999) and at soft X-rays (Li et al 2012, Chernyakova et al 2012). At high and very high energies, the orbital period is established, the superorbital period is hinted at, but could not yet be determined (Albert et al 2006, Abdo et al 2009, Hadasch et al 2012). An influence of the superorbital period for the analysis of gamma-ray data especially in the soft gamma-ray regime was shown by Zimmermann & Massi 2012. Nevertheless, the source is also variable on time scales other than those two periods. Quasi periodic oscillations have been reported in radio (of 84 min) and in X-rays (of 40 min) (Peracaula et al 1998, Harrison et

al 2000). Observations done with the Effelsberg 100-m telescope also clearly reveal variability in radio on the time scale of hours (see Chapter 4).

The superorbital period was only recently discovered to be most likely a result of beating between the orbital period and a second period of 26.9 days (Massi & Jaron 2013). This period was clearly revealed by timing analysis of a long radio data base and is believed to be due to precession of the jet. Results from a morphological analysis of high resolution radio maps, presented in Chapter 3, actually revealed this period first and let to the timing search, which then confirmed it (Massi, Ros & Zimmermann 2012, Massi & Jaron 2013).

Two main scenarios try to explain the emission processes in LS I +61°303: a two-peak accretion/ejection microquasar (Marti & Paredes 1995, Massi 2011b) and a millisecond pulsar model (Maraschi & Treves 1981, Dubus 2006), such as PSR B1259-63 . In Chapter 2, these two models will be reviewed with special emphasis on their implications from radio spectral index analysis. Chapter 3 will review the radio morphology for the two models and in Chapter 4 new broad band radio spectral analysis are shwon and their implications for the emission processes in LS I +61°303 discussed.

Chapter 2

High energy observations and the radio spectral index of LS I +61°303

2.1 Introduction

[Parts of this chapter are published in Zimmermann & Massi (2012).] One of the most peculiar characteristics of the X-ray binary LS I +61°303 is its clear periodicity. The orbital period, P = 26.496 days (phase $\Phi = \frac{t-t_0}{26.496\ d} - \int[\frac{t-t_0}{26.496\ d}]$ with t_0 = JD2443366.775 Gregory 2002) modulates the flux at radio, infrared, optical, H-alpha, X-rays and also gamma-rays (Taylor et al 1982, Paredes et al 1994, Mendelson et al 1994, Zamanov et al 1999, Paredes et al 1997, Abdo et al 2009, Acciari et al 2009). Moreover, there is a superorbital period of 1667 days (phase $\Theta = \frac{t-t_0}{1667\ d} - int[\frac{t-t_0}{1667\ d}]$) that modulates both, the amplitude and the orbital phase of the large radio outburst (Gregory et al 1999, Gregory et al 2002). $\Phi_{outburst}$ oscillates in the range $\Phi \simeq 0.35$ - 0.8, (see Fig. 2-c in Massi & Kaufman Bernado 2009) with a major outburst at $\Phi_{outburst} \simeq 0.6$, that is almost at apoastron ($\Phi_{periastron}$ = 0.230-0.275 Aragona et al. 2009; Casares et al. 2005). In Fig. 2.1, 6.7 yr of radio data from the Green Bank Interferometer (GBI) at 2.2 and 8.3 GHz are shown folded with this long term period of 1667 d.

This long period, Θ, also modulates the H-alpha emission line (Zamanov et al 1999) and was formerly suggested to be due to periodic shell ejections from the circumstellar disk of the Be star (Gregory & Neish 2001). Recently, Massi & Jaron (2013) have shown that this long term period ist most likely simply a beat frequency created by the orbital period of 26.5 days and a second period, revealed by timing analysis of radio data, of 26.9 days and also seen in astrometry analysis of Very Long Baseline (VLBA) data (see Chapter 3). Massi & Kaufman Bernado (2009) have shown that the radio spectral index $\alpha = \frac{log(S_1/S_2)}{log(\nu_1/\nu_2)}$ (with flux density $S \propto \nu^\alpha$) has a dependency on both periods: Θ and Φ (and consequently on the precession period as well). Aim of this chapter is to analyse, by using the α vs. Θ and Φ results, the implications of these two periodicities for the use of high energy data from LS I +61°303.

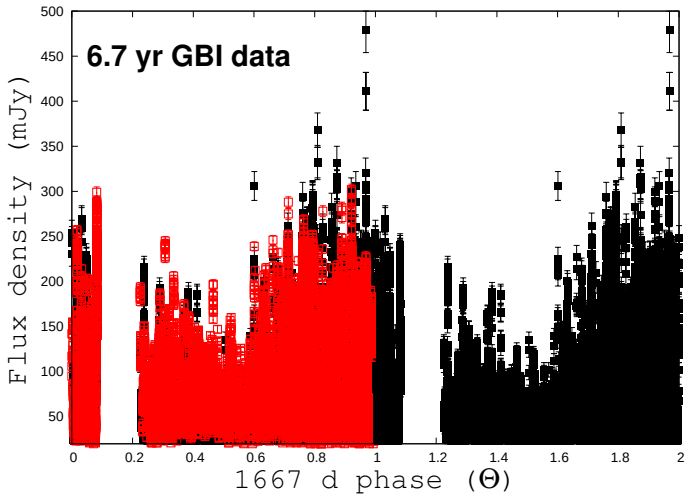

Figure 2.1: Radio light curve of LS I +61°303 from the GBI at 8.3 GHz vs. the long term (1667 days) phase Θ, reproduced from $\Theta_{i=1}$ to $\Theta_{i=2}$ for a better display. In red are given the 2.2 GHz data.

2.2 Radio and X-ray states in LS I +61°303

Any existing theoretical model for LS I +61°303 must not contradict the observational results of the largest available data base for LS I +61°303, which is provided by radio observations. The radio spectral analysis by Massi & Kaufman Bernado (2009) used 6.7 years of NASA/NRAO GBI data from LS I +61°303 at two frequencies, $\nu_1 = 2.2$ GHz and $\nu_2 = 8.3$ GHz and yields two results. One is that the large radio optically thick outburst towards apastron, where α may rise up to $\alpha \simeq$0.1-0.4, is often immediately followed by a new outburst, this time an optically thin one, where α may reach the minimum value of $\alpha \simeq -0.4$ (see Fig.2.2 here and Figs. 3, 4 and 5 in Massi & Kaufman Bernado (2009)). The second remarkable finding resulting from the radio spectral index analysis of Massi & Kaufman Bernado (2009) was that in LS I +61°303 this switch from one kind of a jet (steady jet) to the other one (transient jet) occurs twice along the orbit at the orbital phases predicted by the two-peak microquasar model. One sees a spectral transition, optically thick/ optically thin emission, first around periastron at $\Phi_{crit,1} = 0.33 \pm 0.13$ and then again towards apastron at $\Phi_{crit,2} = 0.7 \pm 0.13$. This is puzzling, because at that orbital phase only negligible flux peaks, < 50 mJy, are observed (see Figs. 3, 5 and 6 in Massi & Kaufman Bernado (2009)). Two models have been proposed for this source: the two-peak microquasar model, where the observed radio emission originates from a relativistic jet (Taylor et al 1992), and a millisecond pulsar model where the radio emission is due to electrons accelerated by colliding winds, the B-star wind and the pulsar wind (Dubus 2006).

Let us first consider the microquasar model (Massi 2010a). The accretion rate is $\dot{M} \propto \frac{\rho_{\rm wind}}{v_{\rm rel}^3}$, where $\rho_{\rm wind}$ is the density of the Be star wind and $v_{\rm rel}$ is the relative velocity between the accretor and the wind of the Be star. It has been shown by several authors (Taylor et al 1992, Marti & Paredes 1995, Bosch-Ramon et al 2006, Romero et al 2007) that the eccentric orbit

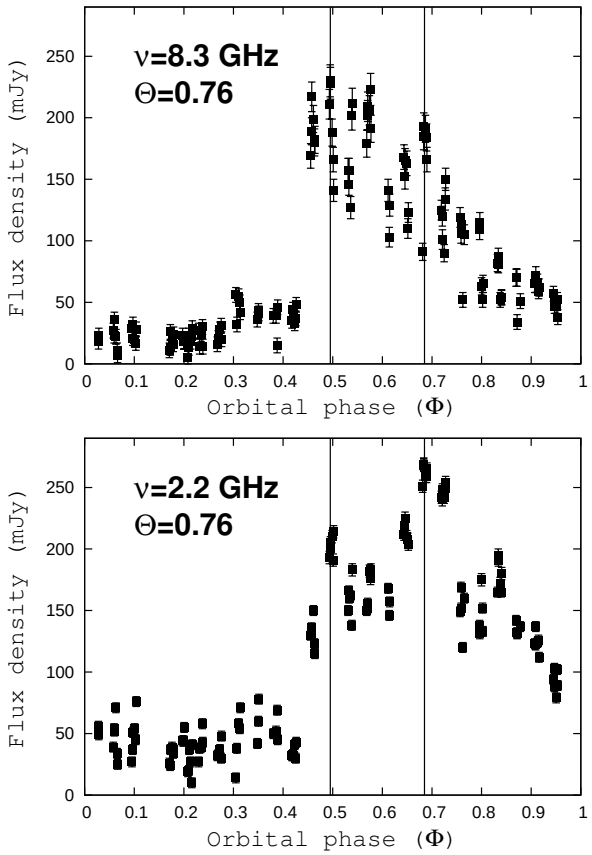

Figure 2.2: Light curves of LS I +61°303 at 8.3 GHz and 2.2 GHz of a data set from the Green Bank interferometer (GBI) of 26.5 days at Θ=0.76 (MJDa=51294). Both light curves have two peaks, marked by a continuous line, the first peak dominates at 8.3 GHz whereas the second peak dominates at the lower frequency.

of LS I +61°303 (e=0.54 − 0.7 (Aragona et al 2009,Casares et al 2005) creates two peaks in the accretion rate curve along the orbit: one close to periastron due to the high density $\rho_{\rm wind}$, and a second one where the drop in density is compensated by the decrease in relative velocity towards apoastron (Bondi et al 1952). Bosch-Ramon et al (2006) have also computed the inverse-Compton (IC) losses of the ejected relativistic particles from upscattering stellar UV photons to higher energies. Then, including energetic losses, the two-peak microquasar model predicts at periastron, where the electrons are embedded in the strong UV-radiation field, a high energy outburst and a very small radio outburst. Associated with the second accretion peak and related ejection of relativistic electrons, more displaced from the star, Bosch-Ramon et al (2006) predict a large radio outburst and a small gamma-ray peak (Fig. 2 in Bosch-Ramon et al. 2006). This prediction is corroborated by *Fermi*-LAT observations of a strong gamma-ray peak around periastron and a weaker second one shifted towards apoastron (Abdo et al 2009).

The two radio outbursts, the large and very small one, should follow the typical characteristics of microquasars: optically thick emission, i.e. $\alpha \geq 0$, sometimes followed by an optically thin outburst, i.e. $\alpha < 0$. The two different kinds of emission are attributed to two different jets: a slow moving continuous conical outflow creating a composite flat/inverted spectrum (i.e. optically thick emission) that sometimes switches into an ultrarelativistic transient jet. This transient jet is associated to shocks where the emission at lower frequencies dominates and therefore results in an optically thin outburst (Fender et al 2004, Massi 2011b). The two-peak microquasar model is therefore corroborated in its predictions by the radio spectral index results: the spectral index, being related to the ratio of flux densities S_1, S_2 at the two frequencies, is little influenced by lower flux values that result from IC losses of the emitting electrons. This is the reason, why at periastron α shows exactly the same switch from optically thick emission to an optically thin outburst (expected for microquasars) as towards apoastron.

The radio spectral characteristics for emission associated with the colliding winds of the pulsar model are completely different. Connors et al (2002) have observed in the non-accreting pulsar PSR B1259-63 in orbit around a Be star that the prolonged injection of energetic particles from the two interacting winds creates an optically thin outburst. In particular, PSR B1259-63 only exhibits a radio outburst around periastron with the emission presenting an optically thin radio spectrum throughout the outburst with a value of $\alpha \sim -0.7$ (Fig. 3 of Connors et al (2002)). The lack of an outburst at periastron in LS I +61°303 was suggested by Zdziarski et al (2010) by strong free-free absorption by the Be wind up to the distance of about 1 AU from the source. However, free-free absorption should not alter the spectrum strongly and therefore the predicted continuous optically thin emission for a non-accreting pulsar is in contradiction with the observed complex switch of the emission in LS I +61°303, from optically thick to optically thin, occurring twice along the orbit, close to periastron and again towards apoastron. The spectral characteristics will be considered again in more detail in Chapter 3 and 4.

The two radio states, a slow outflow ($\alpha \geq 0$) and the transient jet ($\alpha < 0$), are directly linked to two spectrally distinct X-ray states in the unified model of X-ray states with radio jets: the low/hard X-ray state and the steep power-law state. The X-ray states are clearly distinguishable

by their photon index Γ and the shape of their power law spectra (Grove et al 1998, Fender et al 2004, McClintock & Remillard 2004, McClintock & Remillard 2006). A steady jet ($\alpha \geq 0$) occurs in the low/hard X-ray state and its X-ray spectrum, due to IC or synchrotron emission (Remillard et al 2003), is characterized by a power law with photon index $\Gamma \approx 1.5$ and a cut-off at high energies. The high energy cut-off is different in the different sources, with some showing a folding energy $E_f \approx$115 keV (Grove et al 1998) and others, as GX 339-4, a folding energy E_f of only 66 keV (Caballero et al 2009). The transient jet ($\alpha < 0$) is associated with the steep power-law X-ray state, where the emission, probably due to synchrotron/synchrotron self Compton radiation (Massi & Zimmermann 2010), has a spectral photon index $\Gamma > 2.4$ and no cut-off is observed, thereby allowing for high energy emission. In LS I +61°303 , the radio spectral index transition is related to a transition from a very low hard - nearly quiescent X-ray state (see Sect. 5.2 in Massi & Kaufman Bernado (2009)) - to the steep power-law state, twice along the orbit (Massi & Zimmermann 2010). In fact, the very low X-ray luminosity, the observed optical modulation correlated with the radio outburst (only observable close to quiescent states) and the softening associated to a decrease in X-ray flux, observed in LS I +61°303 by Sidoli et al (2006) and consistent with accreting systems in quiescence (Corbel et al 2006, Corbel et al 2008) point towards the source exhibiting a very low hard, nearly quiescent, X-ray state.

2.3 High energy observations of LS I +61°303

In Fig. 2.3, so far published high energy observations of LS I +61°303 are given in terms of how much they cover of the superorbital period Θ. The instruments taken into account are: EGRET (Energetic Gamma Ray Experiment Telescope), INTEGRAL (International Gamma-ray Astrophysics Laboratory), Fermi-LAT (Fermi- Large Area Telescope), MAGIC (Major Atmospheric Gamma-Ray Imaging Cherenkov Telescope) and VERITAS (Very Energetic Radiation Imaging Telescope Array System). Other high energy instruments such as Swift/XRT (Swift/X-ray Telescope), MAXI (Monitor of All-Sky X-ray Image) and RXTE/ASM (Rossi X-ray Timing Explorer/All Sky Monitor) are not considered, their energy range is too low for our purposes (below 15 keV, only Swift/BAT (Swift/Burst Alert Monitor) samples until 194 keV, but is not published), because they will not sample the possible cut-off. The all sky instrument Fermi-LAT has by now covered one superorbital period completely, but the published results so far cover only 2.5 years (Hadasch et al 2012).

In the first part of the analysis, results are presented from a theoretical approach, published in Zimmermann & Massi (2012), showing that due to the periodicities in LS I +61°303, high energy observations of LS I +61°303 must be analysed with respect to these periods. In the second part, preliminary results aree shwon from the analysis of the most recent INTEGRAL data base of LS I +61°303, where this approach is implemented.

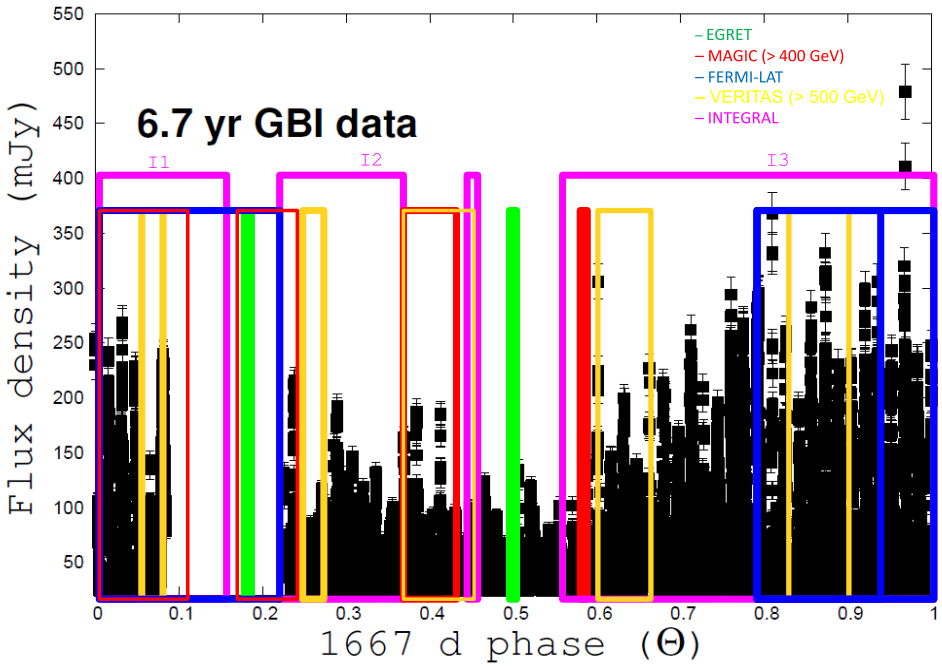

Figure 2.3: Published high energy observations of LS I +61°303 by INTEGRAL (I1,I2 and I3) shown in the context of the 1667 day radio period (Θ). The underlying light curve gives 6.7 yr radio Green Bank Interferometer data at 8.3 GHz folded with Θ (Zimmermann et al 2011).

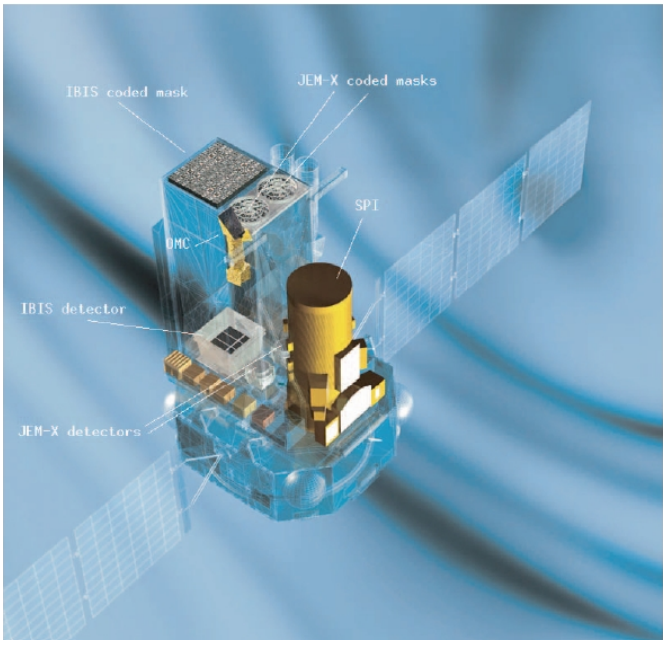

Figure 2.4: The INTEGRAL satellite with its instruments (IBIS, SPI, JEM-X) (Winkler et al 2003).

2.3.1 The International Gamma-ray Astrophyics Laboratory (INTEGRAL)

INTEGRAL is a soft-gamma ray satellite, operated by ESA and launched in 2002 (Winkler et al 2003). Two main instruments are installed upon INTEGRAL: the imager IBIS and the spectrometer SPI. Both are coded mask instruments (explain) (Ubertini et al 2003, Vedrenne et al 2003)). Two other instruments yield monitoring at X-rays (JEM-X) and in the optical (OMC). IBIS operates in the energy range 15 keV-10 MeV. It consists of two detector planes, ISGRI is sensitive between 15 keV and 1 MeV (the maximum effective area lies between 20 and 100 keV). The second plane is PICsIT, which is sensitive between 500 keV and 10 MeV. The IBIS's total field of view is 29.1 x 29.4 degrees, the coded field of view is 8.3 x 8.0 degrees. SPI covers the energy range from 20 keV - 8 MeV. Both instruments are shown in Fig. 2.4.

The data units are given in science windows (ScW), each lasting 3.5-4.5 ks (Grinberg 2010). The data are extracted and reduced with the Off-line Science Analysis (OSA) software, after being provided by the INTEGRAL Science Data Centre (ISDC) (Grinberg 2010).

2.3.2 INTEGRAL data rights proposals

In 2011 and 2012, two data rights proposals were granted (ID 0930080 and ID 1020022). When INTEGRAL observes sources in the vicinity of LS I +61°303 for a given program, this yields automatically observations of LS I +61°303 due to the instrument's field of view. The exclusive use

of these data can then be asked for through data rights proposals. Proposal 1 collects additional 0.5 Ms and proposal 2 additional 0.15 Ms of data on LS I +61°303 . Added to the existing ∼2 Ms of observations used for former analysis (Zhang et al 2010), they give a substantial increase in the data base. For the analysis in part two, only parts of proposal 1 are available, because the data are still being recorded. Data from proposal 2 will be recorded in the next observing cycle. Unfortunately, the cluster at the Erlangen Center for Astroparticle Physics (ECAP), needed for the data reduction of INTEGRAL data has been out of order since December 2012. No other computing facilties were available, therefore, the preliminary results shown in section 3.5 only use data until December 2012. Making use of the data from my proposals in the future, will then render the largest INTEGRAL data base of LS I +61°303 analysed to this date.

2.4 Implications of the radio spectral index transition for INTEGRAL data from LS I +61°303

In Fig. 2.5, only the INTEGRAL observations published until August 2011 are displayed in terms of the Θ intervals in which they were carried out (Zhang et al 2010) and denoted as I1, I2, and I3. Any spectral analysis should consider Θ, because within the energy range covered by INTEGRAL data, two states, the low hard and the steep power-law state, can be detected, when they occur.

Data from LS I +61°303 taken with the International Gamma-ray Astrophysics Laboratory (INTEGRAL/ISGRI 20-500 keV, LS I +61°303 is detectable in the 20-150 keV range), however, yielded surprising results, finding e.g., a photon index only compatible with a low hard state, but without a cut-off along most of the orbit. The photon index of the hard X-ray spectrum, furthermore, depended on how much data was averaged together and whether they were also averaged over the orbital period (Chernyakova et al 2006, Zhang et al 2010). Zimmermann & Massi (2012) explain these results by using the relationship between radio and X-ray states that allows us to predict the kind of emission expected at soft gamma-rays based on the radio emission, or viceversa. In particular, in LS I +61°303, the Θ and Φ periodicities allow us to test this relationship by using GBI data, even if no simultaneous observations are available (as is the case for INTEGRAL). From the radio spectral transitions seen in the GBI data one can infer which spectral transition is expected in X-rays and when. The combination of radio spectral index data from different Θ intervals can then help us to understand what happens when INTEGRAL data are averaged over large parts of Θ.

2.4.1 INTEGRAL observations versus Θ and Φ

In Fig. 2.6, radio spectral index curves are shown with $\Phi_{crit,2}$, i.e., the orbital occurence of the radio spectral index transition for the large radio outburst towards apastron, for Θ = 0.0-0.1 and

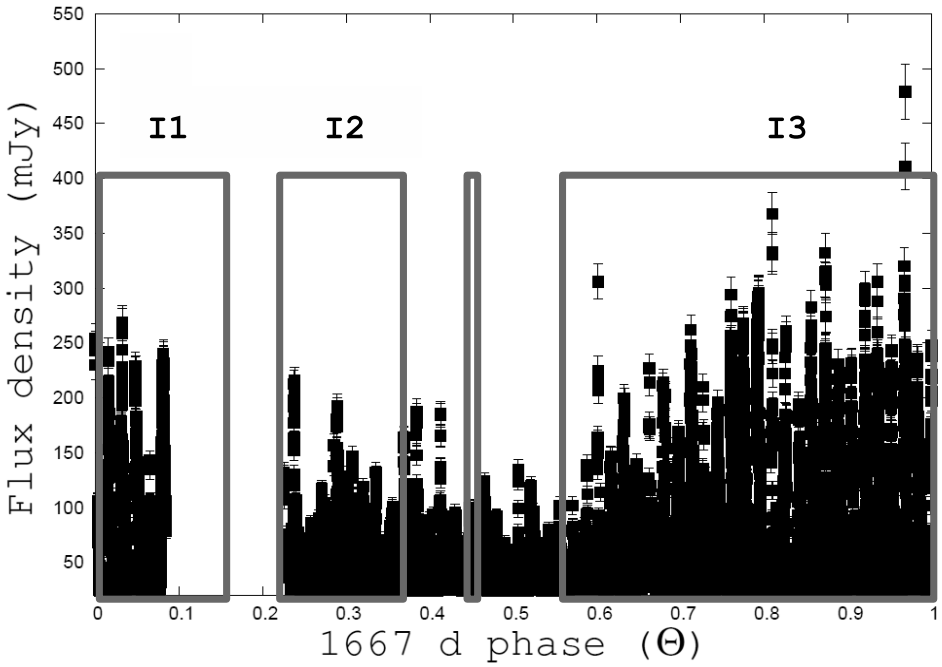

Figure 2.5: Published high energy observations of LS I +61°303 by INTEGRAL (I1,I2 and I3) shown in the context of the 1667 day radio period (Θ). The underlying light curve gives 6.7 yr radio Green Bank Interferometer data at 8.3 GHz folded with Θ. (Zimmermann & Massi 2012).

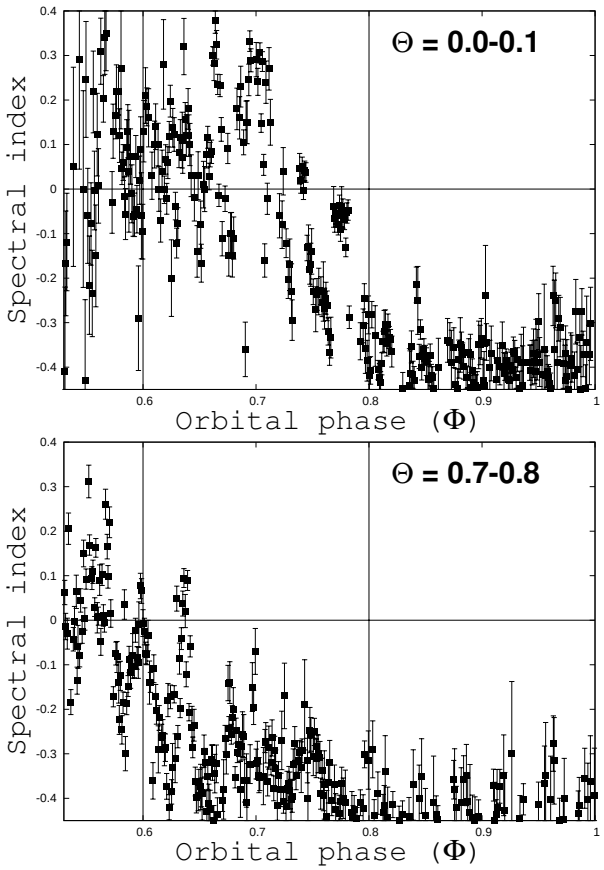

Figure 2.6: Radio spectral index for two different Θ intervals. The vertical lines mark the Φ interval where Chernyakova et al (2006) determined a photon index compatible with a steep power-law state (see Sect. 2). (Zimmermann & Massi 2012)

0.7-0.8. The orbital occurrence at phase $\Phi_{crit,2}$ of the transition from $\alpha \geq 0$ to $\alpha < 0$ lies for Θ = 0.0-0.1 around $\Phi_{crit} \approx$ 0.73-0.77, and for Θ = 0.7-0.8 it occurs around $\Phi_{crit} \approx$ 0.63-0.67. Owing to the connection between radio and X-ray states, it now becomes evident from Fig. 2.6 that, if the energy range of an instrument covers both the low hard and the steep power-law state, folding over the orbital period data of different Θs might result in the mixture of different states. The orbital phase of the transition from optically thick emission to an optically thin outburst does not remain the same over the 1667 d period and the unified X-ray state model with radio jets assumes a physical connection between the radio spectral transition and the X-ray states (Fender et al 2004). The folded data no longer provides any accurate information about the orbital occurrence of the spectral transition. As we show here, the information about one state could even be lost completely, if e.g. the sampling for one Θ interval is finer, which leads to the suppression of information from the other interval, and/or data from several different Θ-intervals, and not only the two intervals shown in Fig. 2.6, are mixed up.

Folding all data or parts of I1, I2, and I3 together in terms of orbital phase increases the sampling and the significance of the signal. In doing so, several authors established that the emission in the interval 10-100 keV is clearly modulated by the orbital phase (Chernyakova et al 2006, Hermsen & Kuiper 2007, Zhang et al 2010). Moreover, Chernyakova et al (2006), who used data from almost all of I3 (covering $\Theta = 0.57 - 0.99$) and a few data points from the beginning of I1 (covering $\Theta = 0.0 - 0.06$), have found that whereas along most of the orbit the photon index Γ was $\approx$ 1.4-1.7 (i.e., low hard state), it changed to $\Gamma = 3.6^{+1.6}_{-1.1}$ (i.e., compatible with a steep power-law state) in the orbital phase interval Φ = 0.6-0.8. This result is consistent with the radio spectral index analysis of Massi & Kaufman Bernado (2009), giving for the same Θ-intervals of I3 the transition to an optically thin outburst (a transient jet) after $\Phi = 0.6 \pm 0.1$. In Fig. 2.6, one sees that for Θ = 0.7 - 0.8 (which is part of I3) the optically thin emission dominates in the interval Φ = 0.6-0.8. Following the radio spectral index though, folding over too much of a Θ cycle could imply that, although the resulting light curves can establish the overall periodicity of the source at these energies, it mixes different spectral states. The analysis of Zhang et al (2010), who used I1, I2, and I3 together (following the same data reduction method as Chernyakova et al (2006)), thereby covering both the minimum and the maximum amplitude interval of Θ, give a hard photon index of $\Gamma \approx$ 1.4-1.9 along the whole orbit (average: 1.7), no longer finding evidence of a very soft spectrum ($\Gamma \geq 2.4$) in the interval Φ = 0.6-0.8.

How can these results be interpreted in terms of the radio spectral index analysis from above? By examining Fig. 2.6, we can see, how by folding together data of two Θ intervals, optically thin and thick emission can be mixed, because the orbital occurrences of $\Phi_{crit,2}$, and therefore of the transition between optically thin/thick emission, differ for the Θ intervals. The optically thin emission then no longer dominates the orbital interval Φ = 0.6-0.8. When averaging over the intervals I1, I2, and I3, optically thick and thin emission get mixed together in the Φ interval of interest. Therefore, the measured photon index must not be directly interpreted as a continuous low/hard state of the source, because it represents the combination of different states. Moreover, we note that this mixing also occurs, when only one Θ interval is selected and the data is averaged over the whole orbit. As one sees in Fig. 2.6, optically thick and thin emission occur alternately

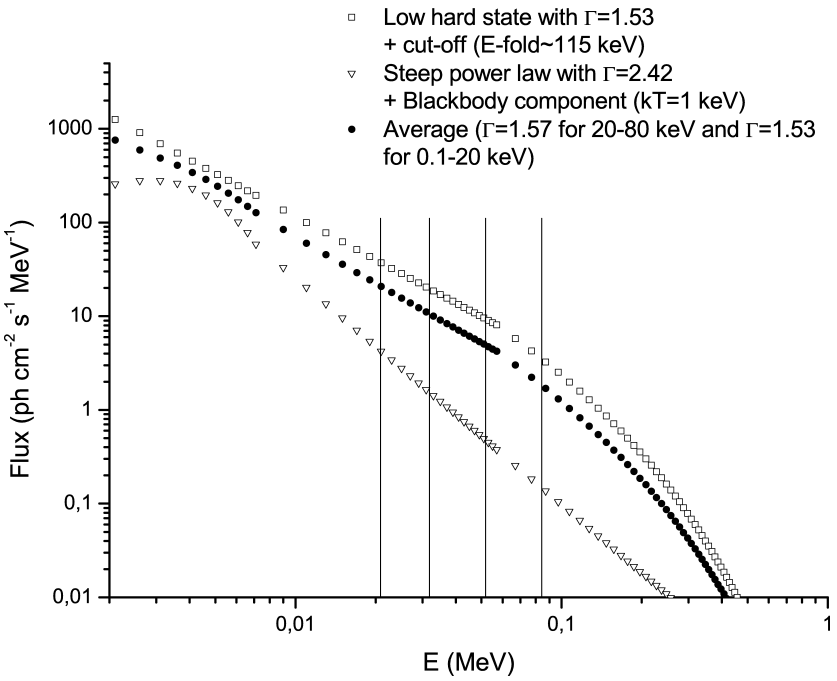

Figure 2.7: Model spectra for the low/hard state (power-law plus cut-off, open squares), the steep power-law state (open triangles) together with a black-body disk component with kT∼1 keV and the average of the two states (filled circles) (Zimmermann & Massi 2012).

during the orbit. When averaging the spectrum across the whole orbit, Chernyakova et al (2006) find again an average photon index of $\Gamma \approx 1.6$ but no cut-off at high energies.

2.4.2 Model spectra

An example of the effect of this mixing of X-ray states is shown in Fig. 2.7; here we show one spectrum for a low/hard state (open squares) and one spectrum for a steep power-law state (open triangles) and the spectrum for the low/hard state is

$$f(E) = \begin{cases} E^{-\Gamma} & E < E_c \\ E^{-\Gamma} \exp\left(-(E - E_c)/E_{fold}\right) & E > E_c, \end{cases} \tag{2.1}$$

where E_c is the cut-off energy and E_{fold} the folding energy, which is in Grove et al (1998) assumed to be approximately twice E_c. We use as an example the source GRS 1716-249 with $E_{fold} = 115 \pm 8$ keV, because this source, analysed by Grove et al (1998) in both spectral states, results in a steep power-law state of significantly lower luminosity. This might also hold for LS I +61°303, as suggested by the results of Chernyakova et al (2006) (i.e. dominance of the low hard state when mixing the data). In Fig. 2.7, we superimpose an average of the two curves (filled circles). The four vertical lines indicate the four points of the averaged (over both Φ and Θ) spectra derived by Chernyakova et al (2006). The fit to these points resulted in a photon index

Γ consistent with a low hard state, but no cut-off at high energies was found. This example shows how an average could yield a curve, where the photon index of the power-law below the cut-off energy ($E_c \approx 115/2$ keV) is consistent with a low/hard state although the steep power-law is part of the data. In addition, we see in this example for GRS 1716-249 that only the last point, among the four ones by Chernyakova et al (2006), samples the average curve after the cut-off and lies, with around 84 keV, still quite close to the cut-off energy ($E_c \approx 115/2$ keV). It would be difficult under this condition to detect the cut-off. For GRS 1716-249, Grove et al. (1998) indeed established that there is exponential decay with $E_{fold} = 115 \pm 8$keV for very well-sampled data up to 300 keV. However, if the cut-off in LS I +61°303 were to occur well before the assumed one, the contribution of the steep power-law would strongly bias the analysis of the averaged data.

2.4.3 Results

For the energy range covered by INTEGRAL data, both X-ray states can be detected, when they occur. From the analysis here, I conclude that folding data over too large Θ intervals could mix up data from different states so that the resulting spectra can no longer be unambiguously interpreted and mimic a persistent low hard state. For data from the energy range accessible to INTEGRAL, even if the data were not folded on Θ, averaging across Φ will destroy any information about the different states. I have pointed out that the lack of a cut-off in the power-law for data averaged all over the orbit, means that if LS I +61°303 has a cut-off well below $\sim$ 115/2 keV, the contribution of the steep power-law will strongly bias the analysis of the spectrum of the averaged data. However, I have shown that a higher cut-off requires highly sensitive sampling, extending well beyond the used range of up to 100 keV. The INTEGRAL results published so far are then explainable with two X-ray states alternating along the orbit in parallel to the two radio states, as expected in the microquasar scenario.

In the next section, this knowledge will be used to slice the existing INTEGRAL data base into suitable intervals and compare spectra and lightcurves for these intervals with the corresponding intervals from the GBI radio spectral index data.

2.5 INTEGRAL observations of LS I +61°303

The INTEGRAL data base of LS I +61°303 consisted in 2010 of ~2 Ms. Data from our data rights proposals will increase this data base, nevertheless, the first part of the analysis was done with the data base until 2010. LS I +61°303 is not very bright at soft gamma-rays, its average brightness is around 0.5 counts/s (compared with one of the brightest sources in this energy range, Cygnus X-1, which has around 1000 counts/s (1000 or 100??)). This is the reason why most analysis so far used the MOSA_SPEC TOOL to extract the spectra (Chernyakova et al 2006, Zhang et al 2010).

As explained in the section above, the amount of data, even when all folded together, yields only four spectral bins, otherwise the significance per bin is too low. Therefore, our aim was to collect as much additional data as possible and re-try, every time new data was available, if the spectral resolution improves substantially. The first results yielded the same four spectral bins as in former publications, but still a distinguishable difference between the four Θ intervals, which were chosen for the analysis (see next paragraph) is visible.

The data reduction was performed at the Karl-Remeis Sternwarte in Bamberg, which is part of the Erlangen Center for Astroparticle Physics (ECAP), in collaboration with Victoria Grinberg.

2.5.1 Radio spectral index data

The INTEGRAL data until 2010 was analysed on four Θ intervals. These intervals where chosen based on two criteria: First, the switch between optically thick and optically thin had to lie in a reasonably similar interval to avoid mixing. Second, the thereby chosen intervals where adapted according to the data coverage of INTEGRAL to allow for a significant analysis. The intervals chosen are Φ=0.1-0.3, 0.3-0.6, 0.6-0.85, 0.85-1.1.

As seen in Fig. 2.8, the two peaks are most pronounced during Θ=0.85-0.1. Both peaks always lie within the interval Φ=0.2-0.7. The switch from optically thick to thin in the second peak lies around Φ=0.5-0.6 for Θ=0.6-0.85, then moves to Φ=0.6-0.7 for the following Θ intervals. During the minimum, Θ=0.3-0.6, the switch is not detected.

2.5.2 Spectra

In Fig. 2.9, preliminary INTEGRAL/ISGRI spectra of LS I +61°303 are given for the four respective Θ intervals. To produce the spectra, all publicly available observations of LS I +61°303 until 2010 were divided into the four Θ intervals and then averaged on Φ. Since the source is faint ($\sigma_{det} \approx 11$ in the 20-40 keV energy band for 2 Ms overall exposure), the spectral extractions were performed with the MOSA_SPEC TOOL, which extracts the spectra from the mosaic images at a given position on the sky (note: spectral points are slightly shifted in energy for viewing purposes) (Zimmermann et al 2011).

Folding, sampling and the flux during the spectral states determine the extend of mixing. Averaging across Φ will as well mix the different outburst episodes, but if not folded too strongly on Θ, the spectral results might indicate, at ~50 keV, a difference in the contribution of the states (see Fig. 2.9). The characteristics of the four intervals are given in Table 2.1 (Zimmermann et al 2011).
In Figs. 2.10, 2.11 and 2.12 preliminary results using all INTEGRAL data until December 2012 are shown. Here, the Θ intervals are only 0.6-0.95 and 0.95-0.3, but different from before, they are also analysed on two Φ intervals, 0.2-0.7 and 0.7-0.2. More science windows per Θ interval

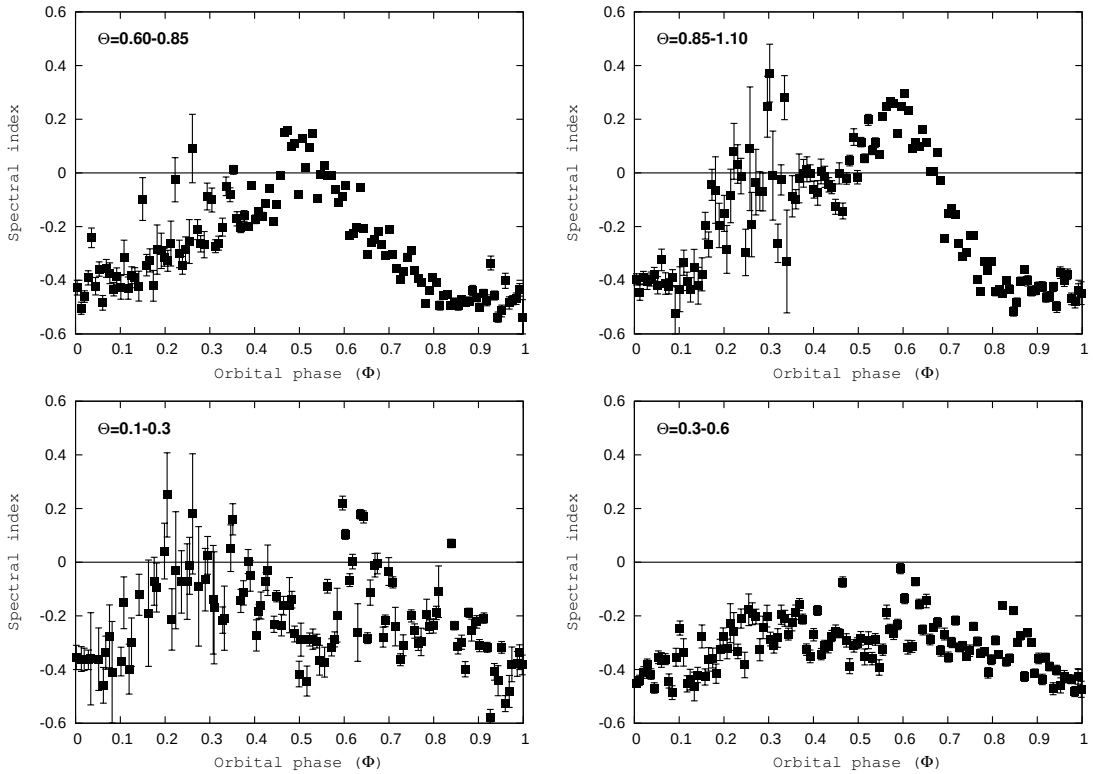

Figure 2.8: Radio spectral index from 4.6 years of GBI data for the four different Θ intervals (Zimmermann et al 2011).

Θ	0.1-0.3	0.3-0.6	0.6-0.85	0.85-0.1
science windows	335	163	242	293
exposure [ks]	686	345	496	578
χ^2	0.3	1.8	1.7	0.46
Γ	1.2	1.7	1.6	1.5
Γ_{min}	0.9	1.0	1.0	1.0
Γ_{max}	1.5	2.6	2.4	2.1

Table 2.1: Spectral characteristics of the four Θ intervals. The spectral index is slightly higher for Θ=0.3-0.6 and Θ=0.6-0.85. The data are still averaged along the orbit, though, which can mix the states as well.

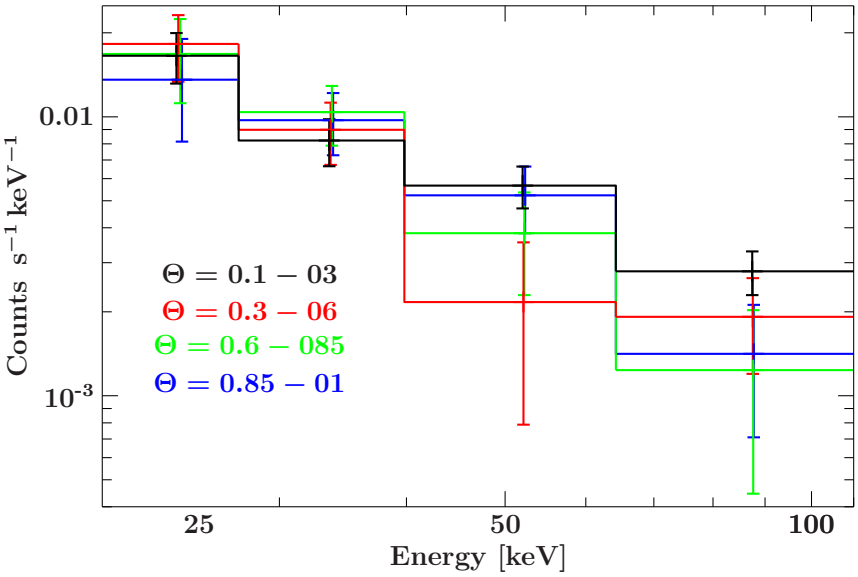

Figure 2.9: INTEGRAL spectra for the four different Θ intervals (Zimmermann et al. 2011). In the first two energy bins (20-40 keV), the spectra do not seem to differ much, but above 50 keV, the values are different, but the error bars are also large. This behaviour is reflected in the spectral index Γ shown in Table 2.1.

are needed for this approach, this leads to the different intervals. From the theoretical approach, also folding across Φ mixes the states, cutting the data into two Φ intervals, but this leads to further reduction in the amount of data per interval. With the data until 2010, this was not possible at all. In Fig. 2.10 the spectra are fitted with simple power-laws. The fits show higher spectra indices for Φ=0.2-0.7 for both Θ intervals as expected, because the main outburst always takes place during this interval. Nevertheless, the χ^2 of the fits shows, that they are not too suitable. A more refined fit analysis needs to be done in the future.

2.6 Conclusions and discussion

I have investigated the implications of the radio spectral index transition, $\Phi_{crit} = f(\Theta)$, in LS I +61°303 for the analysis of INTEGRAL data. In microquasars, this transition is directly linked to the transition between two spectrally distinct high energy states that cover the energy range from X-rays to gamma-rays (Grove et al 1998), but which are here simply referred to as X-ray states: the low hard X-ray state and the steep power-law X-ray state. The INTEGRAL results are then explainable with two X-ray states alternating along the orbit in parallel to, as expected in the microquasar scenario, the two radio states.

What does this imply for the analysis of the HE/VHE data? Most important, it raises the question whether the unbroken powerlaw associated with the steep power law state could explain the

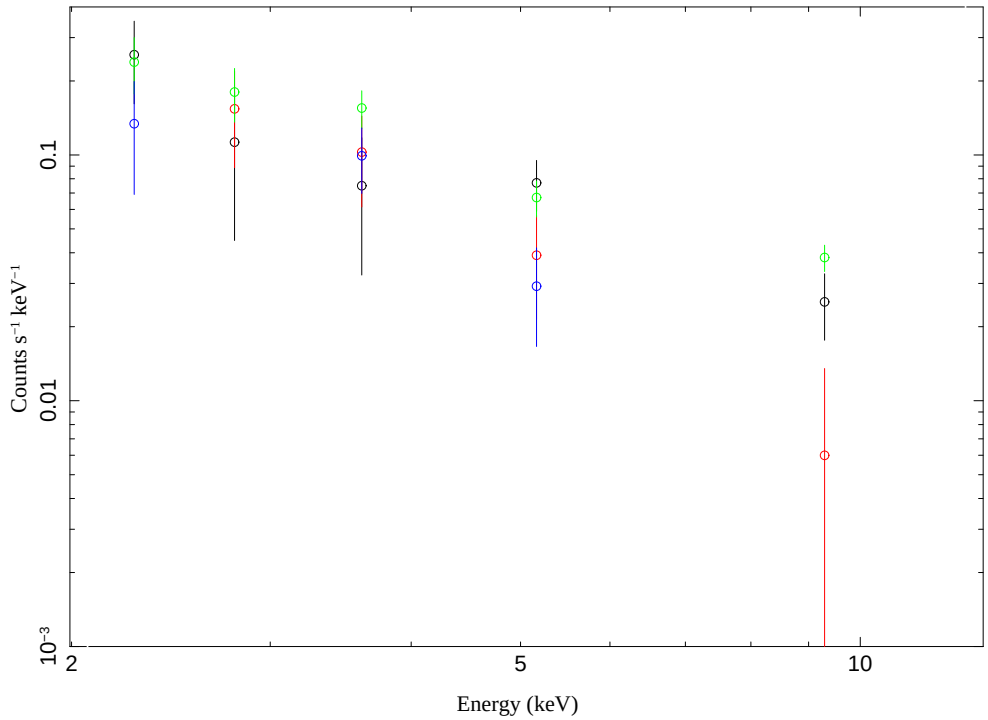

Figure 2.10: Spectra from all INTEGRAL data until December 2012 for Θ=0.6-0.95 and 0.95 to 0.3 for Φ=0.2-0.7 and 0.7-0.2 respectively. Black: Θ=0.6-0.95, Φ=0.2-0.7, Red:Θ=0.6-0.95, Φ=0.7-0.2, Green: Θ=0.95-0.3, Φ=0.2-0.7, Blue: Θ=0.95-0.3, Φ=0.7-0.2. (Note: the energy axis was multiplied by 0.1 and correspondingly the counts/s*keV axis multiplied by 10.)

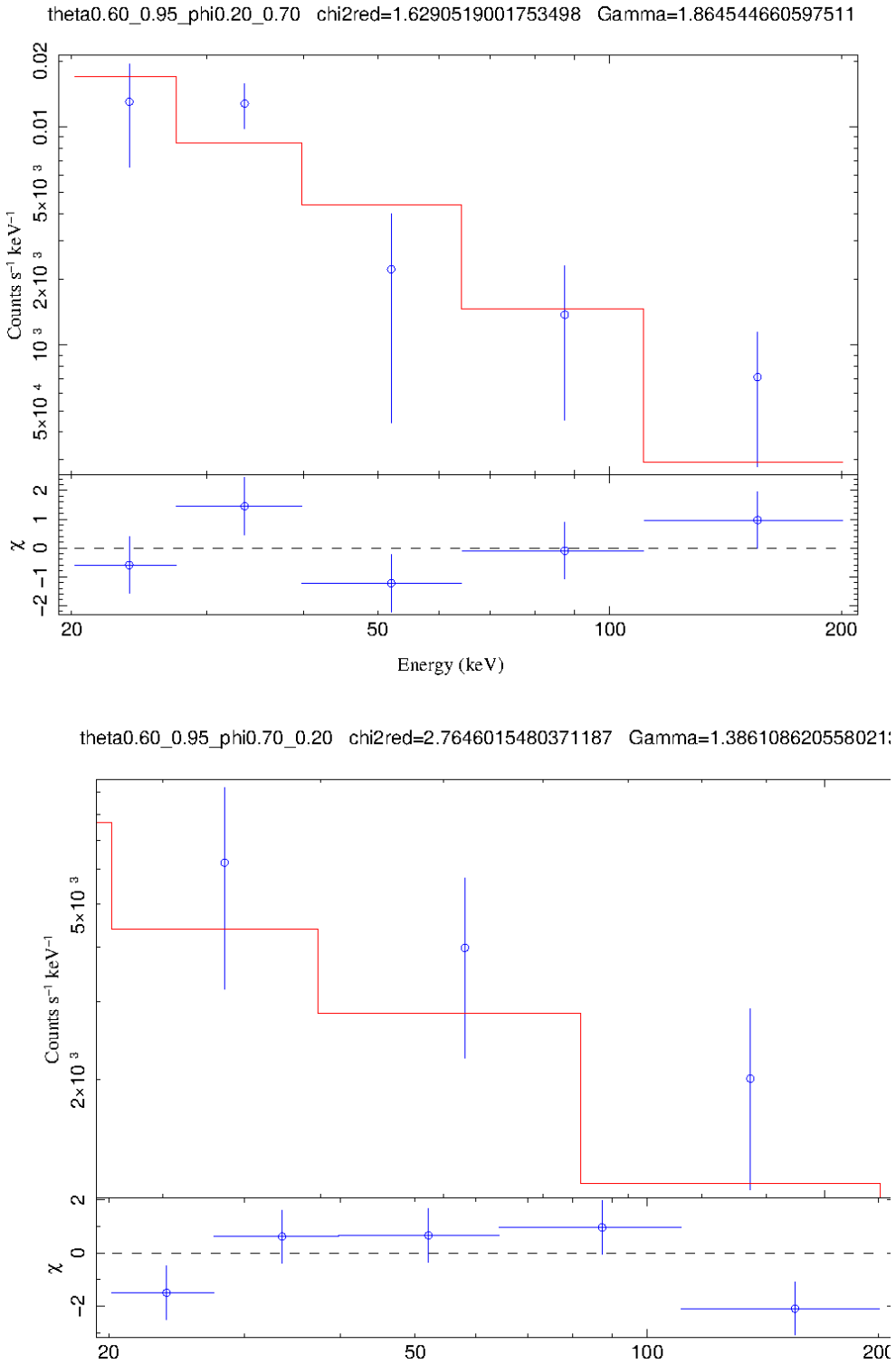

Figure 2.11: Spectra and simple power-law fits from INTEGRAL data until December 2012 for Θ=0.6-0.95 and Φ=0.2-0.7 and 0.7-0.2.

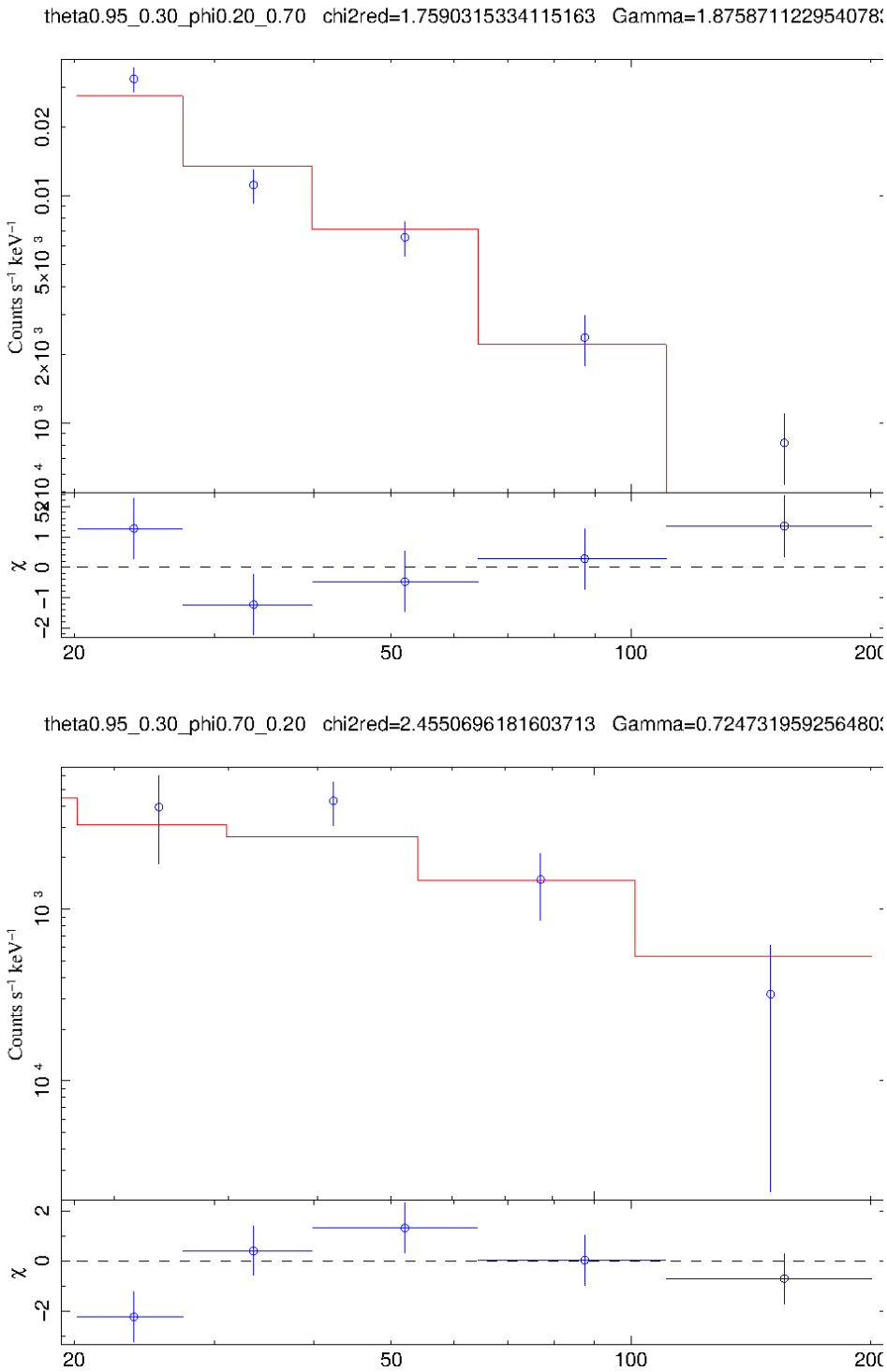

Figure 2.12: Spectra and simple power-law fits from INTEGRAL data until December 2012 for Θ=0.95-0.3 and Φ =0.2-0.7 and 0.7-0.2.

HE/VHE emission seen in LS I +61°303. In fact, for VHE, when LS I +61°303 is detected by MAGIC or VERITAS, its spectrum is always well fitted with a photon index of $\gtrsim$2.4 (Albert et al 2009, Acciari et al 2011a, Aleksic et al 2012), which is the same as expected during the steep power law. In this context, the observations by Anderhub et al (2009) are of special interest. They have observed simultaneously X-ray and VHE emission from LS I +61°303 and found a correlation. Massi & Zimmermann (2010) noticed that for these observations the two fluxes result in $F_{\rm VHE} \propto F_{\rm X}^{\eta}$ with $\eta = 0.99$ in agreement with the correlation observed in blazars (Katarzynski et al 2010), where the X-ray emission is due to synchrotron, and VHE is synchrotron self-Compton (SSC) (Katarzynski et al 2005). As mentioned in the beginning, the micro-blazar nature for LS I +61°303 was suggested by its one-sided jet radio morphology, typical for blazars (Kaufman Bernado et al. 2002, Massi et al. 2004). Concerning the photon index of Blazar emission, Acciari et al 2011b report that during a bright flaring event of the Blazar 1ES 2344+514, VERITAS measured a photon index of $\Gamma = 2.43 \pm 0.22$, whereas for the X-ray emission, RXTE and Swift-XRT measured a hard photon index of 1.86-1.97. This is in the same range as the photon index of the X-ray emission measured by Anderhub et al (2009) for LS I +61°303. In fact, the VHE detected by MAGIC had a $\Gamma = 2.7$ and the X-ray emission detected by *XMM-Newton* and Swift-XRT a harder photon index of 1.54-1.87. For LS I +61°303, several authors have explained the X-ray excess around apastron with synchrotron emission and the VHE with either external inverse Compton (EIC) or SSC emission (Gupta & Boettcher 2006, Zabalza et al 2011a). Zabalza et al (2011a) demonstrated that the X-ray/VHE correlation observed by Anderhub et al. (2009) is compatible with a one-zone leptonic particle population producing the emission. Their models use the observed X-ray photon index (1.55-1.67) and can reproduce the observed lightcurves quite well. Interestingly, this is also comparable to the photon index expected for the low hard state and could be mistaken as such. The soft X-ray synchrotron emission during the steep power law state can then explain actually two facts: First, the VHE emission by invoking SSC and, second, the absence of an accretion disk blackbody component in the soft X-rays (0.1-10 keV) expected during the steep power law state, if the jet points close to our line of sight as in Blazars and overshines the disk. Due to the lack of simultaneous hard X-ray/TeV observations of LS I +61°303, it remains open, if the jet component extends into the hard X-ray regime.

Concerning high energy emission in the GeV range, detected e.g., with *Fermi*-LAT, the picture is more diverse. The steep power law might not be the only emission process, as the GeV emission is seen all along the orbit. Electrons from the steady jet can always upscatter stellar UV photons to GeV energies (i.e., EIC see Bosch-Ramon et al. 2006). Nevertheless, more energetic particles from the transient jet could in addition also produce GeV emission via EIC and SSC. The first eight months results of *Fermi*-LAT observations from August 2008 until March 2009 show a strong γ-ray peak around periastron and a weaker second one shifted towards apastron (Abdo et al 2009). These two peaks can be well explained in the two-peak microquasar model (see e.g. Massi (2011b) or Bosch-Ramon et al (2006)) with external IC (EIC) losses from upscattering of stellar UV photons by the same particles responsible for the radio synchrotron emission (also seen all along the orbit) . Nevertheless, the comparison in Massi (2011b) between the *Fermi*-LAT observations with the GBI radio archive data relative to the identical Θ interval (but in different periodic cycles) has shown an association of the two γ-ray peaks with the two α peaks (Fig. 4 in

Massi 2011b), which could imply that parts of the GeV emission also arise from the steep power law state. Intriguingly, the spectrum measured by *Fermi*-LAT shows, in addition to a power law with a cut-off around 6 GeV, upper limits possibly compatible with the spectrum measured with MAGIC and VERITAS (see e.g., Fig. 2 and 3 in Hadasch et al 2012).

In any case, due the connection between the radio and the HE/VHE emission, the analysis done here for INTEGRAL can and should in principle be extended to other high energy instruments, if the Θ coverage is good enough. In particular, the recent flux evolutions at HE/VHE imply that this data should be analysed on as short Θ intervals as possible. As discussed in Massi & Kaufman Bernado (2009), the two peak shape of the α vs. Φ curve varies with Θ. During the long period, it is most pronounced in Θ=0.0-0.1 and 0.9-1.0, appreciable at Θ=0.2-0.3 and 0.7-0.9 and absent at Θ=0.3-0.6 (see Fig. 5 in Massi & Kaufman Bernado 2009). In addition, the distance of the two peaks varies with Θ. These variations in the accretion curve are predicted by the two-peak microquasar model of Marti & Paredes (1995) by incorporating changing wind velocities for the Be star (see their Fig.6), although the recent findings by Massi & Jaron (2013) explain Θ entirely with beating. Nevertheless, in any case a reflection of this behaviour at other wavelengths due to the connected emission processes can be expected. As a matter of fact, there is an interesting increase in the overall flux level observed with *Fermi*-LAT after March 2009 ($\Theta \approx 0.92$) together with a broadening of the peak shape (Hadasch et al 2012). The up to now observed *Fermi*-LAT variations are therefore consistent with the fact that α varies with Θ. Similarly, strong variations are observed at very high energies. The source went from being detected around apastron with VERITAS and MAGIC (VERITAS: Θ=0.38, 0.4-0.47; MAGIC: Θ=0.17-0.25, 0.37-0.44, 0.59-0.6) to becoming quiescent between 2008-2010. No detection was reported by VERITAS for Θ=0.83-0.08, but weak detection by MAGIC for Θ=0.05-0.11 around apastron. VERITAS detected it again in October 2010 corresponding to Θ=0.26, but this time around periastron (Albert et al 2009, Acciari et al 2011a, Aleksic et al 2012). Nonetheless, at the moment the insufficient Θ coverage of these instruments does not allow for a more closer comparison. Still, the observations clearly indicate that for the analysis of such data, Θ should be considered to avoid a possible mixing of the outbursts.

Using these insights for the analysis of the currrently available INTEGRAL data set of LS I +61°303 , preliminary results are given here. Folding, sampling and the flux during the spectral states determine the extend of mixing. Averaging across Φ will as well mix the different outburst episodes, but if not folded too strongly on Θ, the spectral results might indicate, at ~50 keV, a difference in the contribution of the states (see Fig. 2.9).

The microblazar clues reached here from the X-ray and gamma-ray data lead us to investigate more closely a precession scenario for LS I +61°303. For this, the currently longest available high resolution radio data set from the VLBA, taken in 2006, was re-examined (Massi, Ros & Zimmermann 2012) with regards to its morphology. These results are presented in the next chapter followed by a thourough flux density and spectral analysis as well as modelling of gaussian components to determine upper limits of the jet velocity.

Chapter 3

VLBI jet components in LS I +61°303

3.1 VLBI images of the precessing jet of LS I +61°303

This section has been published in Massi, Ros & Zimmermann (2012).

3.1.1 Introduction

In 1993, a VLBI observation of LS I +61°303 showed that the radio emission had a structure of milliarcsecond (mas) size corresponding to a few AU at the distance of 2.0 kpc (Massi et al 1993, Frail & Hjellming 1991). The complex morphology in successive VLBI observations (Peracaula et al. 1998, Paredes et al. 1998, Taylor et al 2000, Massi et al 2001,2004) highlighted the unlikelihood of an interpretation in terms of a microquasar with a constant position angle. The radio morphology not only changes position angle, but it is even sometimes one-sided and at other times two-sided. This suggested the hypothesis of LS I +61°303 being a precessing microblazar (Kaufman Bernado et al. 2002, Massi et al 2004). A microblazar, i.e., a microquasar with radio jets forming a small angle, θ, with respect to the observer's line of sight, has been proposed to be the Galactic version of extragalactic blazars. Doppler boosting enhances the radiation from material that is moving towards the observer, and attenuates it when it moves in the opposite direction. In cases of substantial flux attenuation in the receding jet (i.e., attenuation to a level fainter than the sensitivity of radio images), the structure will appear as a one-sided jet. A precession of the jet leads to a variation in the angle, θ, and therefore variable Doppler boosting. The result is both a continuous variation in the position angle of the radio-emitting structure and of the flux density ratio of the approaching to the receding jet (Massi 2007).

In known precessing X-ray binaries, the timescale for tidally forced precession of the accretion disk around the compact object, induced by the companion star, lies within the range $8-22$ times the orbital period (Larwood 1998, Massi & Zimmermann 2010). In this context, the peculiarity of the variations in LS I +61°303 is their short timescale with respect to the orbital period of 26.496 d. Massi et al. (2004) found that MERLIN images revealed a surprising variation of 60° in position angle in only one day. Even if quantitatively the relationship between position

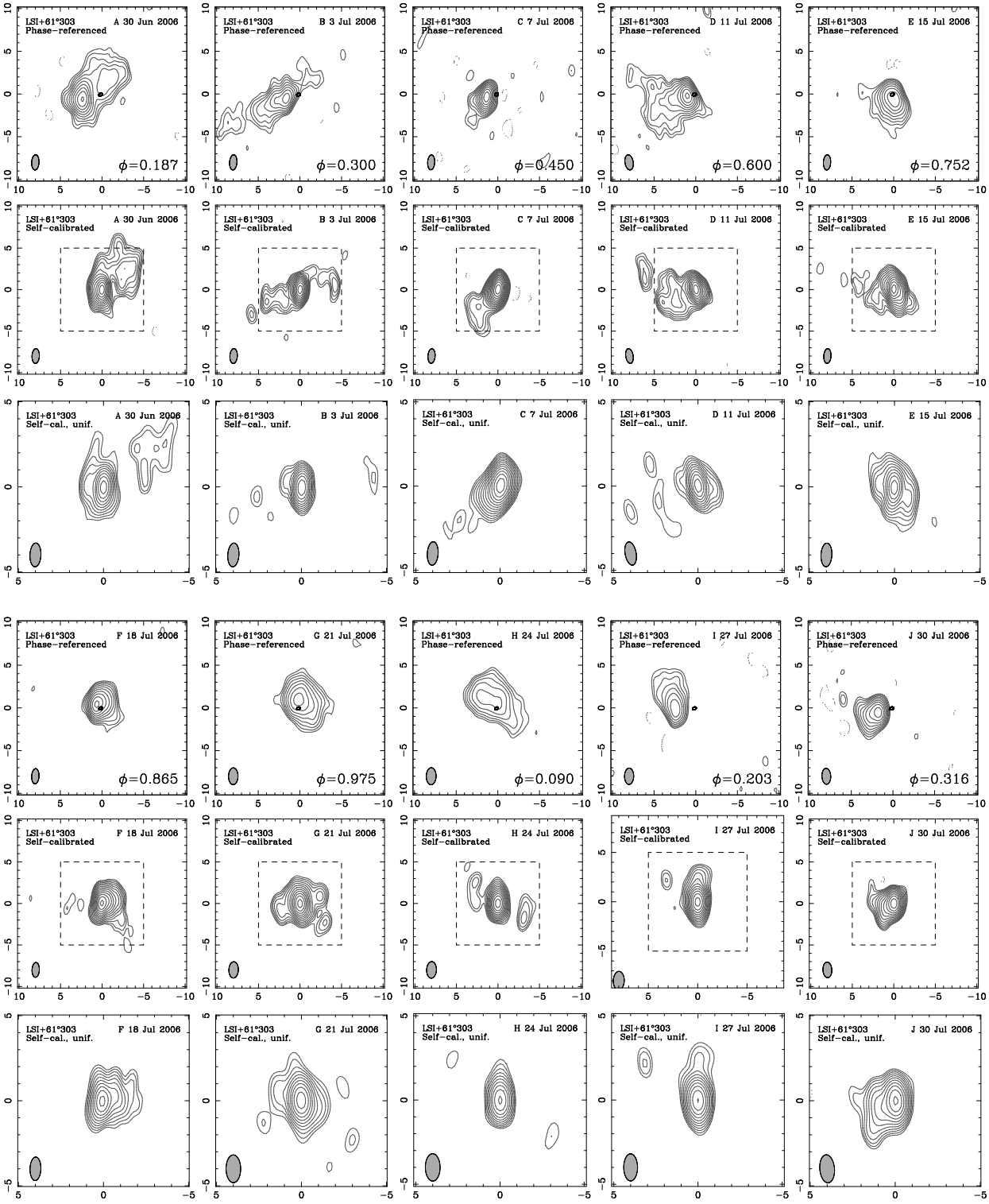

Figure 3.1: Images of VLBA runs A-J at 8.4 GHz (3.6 cm) of LS I +61°303. The units on the axes are milliarcseconds (mas). For each run, three maps are presented, the phase-referenced map (beam of 1.8 - 2.0 mas × 0.9 - 1.1 mas, shown in the bottom left corner), the self-calibrated map at the same resolution, and the self-calibrated map with a beam of 1.4 - 1.6 mas × 0.6 - 0.9 mas. Contour levels for all maps are -4, 4, 5.66, 8, 11.3, 16, 22.6, 32, 45.2, 64, 90.5, 128, 181 σ (with 1σ=0.1 mJy/beam for the top and bottom maps, $1\sigma \simeq 0.07$ middle maps). At the center of the phase-referenced images, we trace, in scale, the orbit.

angle in the image and the viewing angle θ is not straightforward, a rapid variation in the position angle implies nevertheless that there is clearly a rapid variation in θ. The fast position angle variation has been confirmed by VLBA observations. Dhawan et al. (2006) measured in VLBA images a rotation of the inner structure of roughly 5° -7° in 2.5 hrs, that is again a variation of almost 60° /day, but suggested that the variations were due to a cometary tail of a pulsar. If the compact object is a pulsar, the interaction between its relativistic wind and the equatorial wind of the Be star is predicted to create a bow-shock around the pulsar with a sort of cometary tail, i.e., a one-sided structure, extending away from the Be star (Dubus 2006). However, the analysis of the radio spectral index by Massi & Kaufman Bernado (2009) prove that LS I +61°303 displays the typical characteristic of microquasars of an optically thin outburst after an interval of optically thick emission. In microquasars, the so-called transient jet associated with the large optically thin outburst, is related to shocks travelling in a pre-existing steady jet, that is a slow-moving continuous conical outflow with a composite flat/inverted radio spectrum (i.e., optically thick emission) (Fender et al. 2004, Massi 2011a,b). The remarkable finding for LS I +61°303 is that, during the maximum of its long-term periodicity (4.6 yr) the alternance between optically thick and optically thin emission, occurs twice during the orbit, first around periastron and then again, shifted by almost 0.3-0.4 in orbital phase (0.3-0.4 × 26.496 d = 8-11 d after periastron), i.e. towards apastron (Massi & Kaufman Bernado 2009). This agrees with the well-known "two-peak accretion/ejection model", which has been applied by several authors to LS I +61°303, predicting, for large mass accretion rate, $\dot{M}$, two events: one around periastron and the second shifted about 0.3 in orbital phase towards apastron (Taylor et al. 1992, Marti & Paredes 1995, Bosch-Ramon et al. 2006, Romero et al. 2007).

The radio spectral index data corroborate the microquasar model for LS I +61°303. The most important uncertainty is therefore the process that could produce the observed fast precession. An essential step in any investigation is to establish the precessional period. This parameter could be derived by the reanalysis of the VLBA observations. These observations were performed by Dhawan et al. (2006) every 3 days over 30 consecutive days, towards the minimum of the long-term periodicity. Dhawan et al. (2006) suggested that the peaks of the maps trace an erratic ellipse. In a precessing microblazar, as explained below, the core component of the steady jet describes an ellipse, whereas the transient jet adds random shifts. To determine important precession parameters, e.g. the period, we therefore reanalyzed the set of VLBA observations performed by Dhawan et al. (2006).

3.1.2 Data reduction and results

LS I +61°303 was observed by the VLBA on ten different days from 2006 June 30 (segment A) to 2006 July 30 (segment J). The observations (code BD117) included data at 2.3 GHz and 8.4 GHz. We performed the post-correlation data reduction using AIPS. The phase and amplitude calibration were performed in a standard way: corrections for residual Earth orientation parameters in the correlator model and ionosphere—in the latter case those derived from GPS data—were introduced; the digital sampling amplitude corrections (ACCOR) were applied; sys-

tem temperature and gains were applied to get the amplitude calibration (APCAL); delay offsets between sub-bands were corrected using pulse-tones measured during the observations (APCOR); a parallactic angle correction was introduced; and the final delay and rate calibration across the observing band was performed using the FRING routine. After these procedures, the data for the phase reference calibrator, J0244+6228, were exported to be imaged in Difmap. We read the image back into AIPS and calibrated the amplitudes and phases for the source and produced a hybrid map of the source with IMAGR within AIPS, that matched the results obtained with Difmap. After that, the delay and rate were calibrated again with FRING after dividing the data by the clean-component model produced by IMAGR for this source to get structure-free solutions for J0244+6228. The structure-free solutions obtained were then interpolated to the target source, LS I +61°303, and those data were exported to be imaged.

Analysis and results of the 8.4 GHz data

The 8.4 GHz phase-referenced images (with respect to J0244+6228) shown in Fig. 3.1, closely reproduce the Dhawan et al. (2006) structures. At their center, we show the orbit with a semi-major axis of $(0.22 - 0.23)$ mas ($\simeq 0.7 \times 10^{13}$ cm at a distance of 2 kpc), that was derived from the third Keplerian law for $P = 26.496$ d with a mass for the B0 star of 17 $M_{\odot}$ and a mass for the compact object of $1.4M_{\odot} - 4M_{\odot}$, and traced using Casares et al (2005) orbital parameters. The orbit is not only much smaller than the radio-emitting region, but also smaller than the interferometric beam of the VLBA at this wavelength. We make this remark because the zoomed orbit in Fig. 3 by Dhawan and collaborators (zoomed to show more clearly the orbital phase of each run) may unfortunately produce the wrong impression that the orbit is resolved when it is not, and only the accuracy of the astrometry, which is 0.04 mas at 8.4 GHz, is of a smaller scale than the orbit (see: Analysis and results of the 2.3 GHz data). For each run, we present in Fig. 3.1 both the phase-referenced and the self-calibrated images. Self-calibrated images were produced with the automatic procedure Muppet of the Caltech Difmap imaging package (Sheperd 1997). Using self-calibration, the information on absolute flux density and absolute position are lost, but the removal of residual calibration errors improves the dynamic range by up to a factor of four for our maps (Cornwell & Fomalont 1999). Muppet starts with a point source as an initial model then automatically selects the clean boxes around peaks with signal-to-noise ratio (S/N) values ≥ 6, and switches on amplitude plus phase self-calibration after phase-only self-calibration cycles have converged. The high limit of the signal-to-noise ratio S/N ≥ 6 prevents the risk of creating artifacts, which are only introduced when self-calibrating below S/N < 4 (Marti-Vidal & Marcaide 2008). For epoch G, there is a significant difference between the phase-referenced image and the self-calibrated image at the same resolution (see Fig. 3.1). Therefore, for this epoch, we also self-calibrated the data manually. Figure 3.2 shows an intermediate image after eight manual iterations of hybrid mapping starting with a point source and using phase-only self-calibration. The two images of Fig. 3.2 clearly show the same structures only with different flux densities. This difference depends upon further iterations of amplitude self-calibration performed by Muppet.

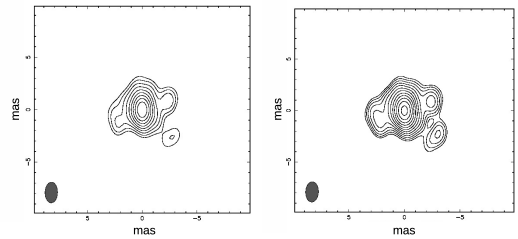

Figure 3.2: Left: Intermediate self-calibrated image of run G, at 8.4 GHz, after eight manual iterations of hybrid mapping with phase-only self-calibration. The beam is 1.96 mas × 1.14 mas at -2° . Contour levels are -4, 4, 5.66, 8, 11.3, 16, 22.6, 32, 45.2, 64 σ, with 1σ=0.18 mJy/beam. Right: Output of automatic hybrid mapping by Muppet. Muppet switches on amplitude plus phase self-calibration after phase-only self-calibration cycles have converged. The beam is 1.96 mas × 1.14 mas at 1 ° . Contour levels are -4, 4, 5.66, 8, 11.3, 16, 22.6, 32, 45.2, 64, 90.5, 128, 181 σ, with 1σ=0.08 mJy/beam.

The determination of the peak position in the phase-referenced maps is an issue, especially if the source is not Gaussian-like or symmetric, as was the case in some epochs. The first approach is to determine the location of the brightest pixel with IMSTAT, then three different methods were applied to fit the position either in the image plane with JMFIT and MAXFIT, or in the visibility plane, with modelfit in Difmap. All results from the four applied methods coincide within $(1-3)\,\sigma$, trace an ellipse over time, and show that the peak of run E is displaced from the other peaks. However, the Gaussian fits have asymmetric residuals, which indicates that the brightest parts of the images are asymmetric. As discussed in Sect. 3, the core of the steady jet for a microblazar is clearly not Gaussian, because of Doppler boosting: the redshifted part should be fitted with a smaller half ellipse than the blueshifted part. For consistency, we use for Fig. 3.3 the results for IMSTAT (coincident within $1\,\sigma$ with MAXFIT). It is evident that the peaks of the consecutive images clearly trace an ellipse 6−7 times larger than the orbit. Galactic scattering at 8.4 GHz, as discussed in the next section, gives rise to an error of 0.04 mas. This value is slightly smaller than the average value of 0.05 mas estimated for the astrometric accuracy of a full track phase-referenced VLBI experiment (Pradel et al. 2006).

In the images, the larger dynamic range of the self-calibrated maps show in the image of run A a double-component structure. This is clearly unlikely to correspond to a pulsar nebula, whereas it could be compatible with either the approaching and receding component of a transient jet, or with variable Doppler boosting along a one-sided twisted jet. Image B already shows in the phase-referenced map with natural weighting a double-sided morphology difficult to reconcile with the pulsar nebula. The self-calibrated map shows an intriguing twisted jet as expected for a fast precession. Runs C, F, I, and J show a one-sided jet or alternatively a pulsar cometary-tail but again runs D, E, G, and H show the double-sided jet structure.

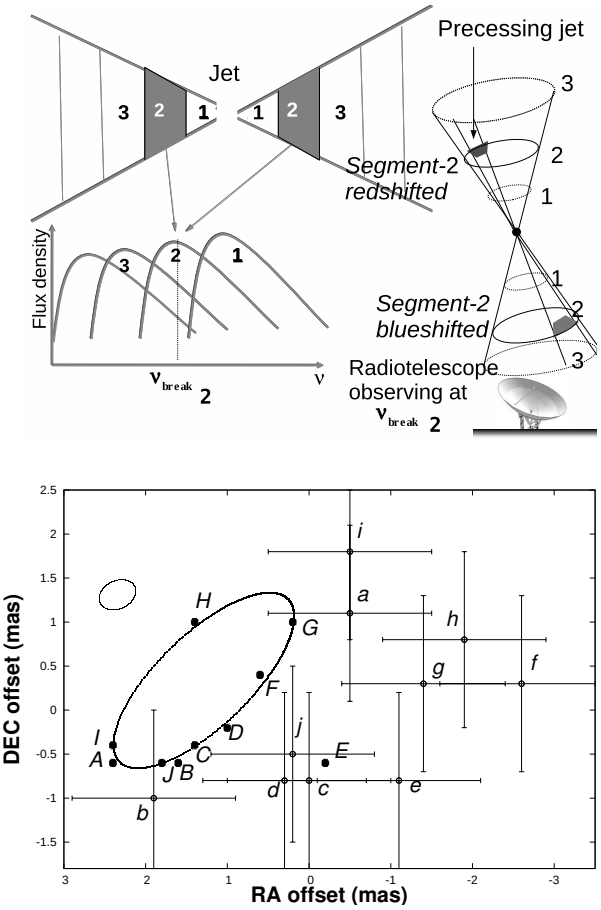

Figure 3.3: Top-left: Superposition of individual spectra, each with a different $\nu_{\rm break}$, associated with different segments of a steady jet. Top-right: For a precessing microblazar, the core component, dominated by the approaching jet contribution because of Doppler boosting, will describe an ellipse during precession. Bottom: Astrometry of consecutive peaks of VLBA 8.4 GHz maps (capital letters) and 2.3 GHz maps (small letters) for runs A-J with the orbit drawn to scale at an arbitrary distance. East is to the left. Peak of 8.4 GHz map E, even if displaced from the other ones, which is therefore likely affected by the approaching component of the transient jet, is at a position angle that is consistent with the other peaks. The small error of 0.04 mas for the astrometry at 8.4 GHz is indicated by the filled squares. That the precessing compact object moves in an orbit with semimajor axis of ∼0.2 mas introduces additional variations. Errorbars of 1 mas for the astrometry at 2.3 GHz represent only a lower limit to the error associated with large Galactic scattering and low resolution (see Sect. 2.2).

Analysis and results of the 2.3 GHz data

In Fig. 4 of Dhawan et al (2006), the 2.3 GHz astrometry seems to show a shift of up 2 mas from the 8.4 GHz astrometry. In practice, no hypothesis can be made lacking the points of error bar. We show in this section that, whereas the accuracy associated with the peaks at 8.4 GHz is 0.04 mas, that associated with the peaks at 2.3 GHz is more than one order of magnitude higher. We re-examined the 2.3 GHz data. Large amounts of Galactic scattering at this frequency affects the data, broadening the images. This effect is discussed in detail in the astrometric works of Lestrade and collaborators (Lestrade et al. 1985, 1999), who attributed the size of 4.1 mas, determined at 1.62 GHz, to broadening caused by interstellar scattering. Therefore, at 2.3 GHz the broadening, which is proportional to λ^2, is 2.2 mas (whereas at 8.4 GHz, it is only 0.16 mas). The additional complicating factor is that refractive interstellar scintillation will cause the apparent source position to wander, and the magnitude of this wandering is hard to calculate (see, e.g. Rickett (1990).

We were able to estimate the quality of the astrometry from the scatter in positions of the check source observed in project BD117, namely J0239+6005, that is 2.5° apart from the calibrator J0244+6228. We determined the astrometric stability of that check source at 8.4 GHz and 2.3 GHz and used the results to assign error bars to the astrometric measurements at both frequencies. First, we performed the phase-referencing analysis of the source J0239+6005 with respect to the phase reference calibrator J0244+6228, and then determined the peak position in the maps of J0239+6005 for the consecutive runs. As shown in Fig. 3.4, when there is no precession and one expects all results to coincide within their errors, the points at 8.4 GHz indeed overlap and have a dispersion of 0.08 mas. The result at low frequency is completely different. The scatter is huge: the dispersion in the points at 2.3 GHz is 1.2 mas. The astrometric error scales with separation from the phase reference calibrator (Pradel et al 2006). J0239+6005 is 2.5° apart from the calibrator J0244+6228, whereas LS I +61°303 is 1.4° away from J0244+6228. Therefore, the 0.08 mas rms for 8.4 GHz data and the 1.2 mas rms for 2.3 GHz data of J0239+6005 scales to 0.04 mas and 0.7 mas, respectively, for LS I +61°303. Moreover, at 2.3 GHz, besides the already large error of 0.7 mas associated with the scattering, there is also the error due to the low resolution. In fact, at 2.3 GHz, LS I +61°303 is unresolved/barely resolved with the VLBA (see Fig. 5). In the large beam, 4 mas × 7 mas, the optically thin emission of the extended jet may contribute substantially and, depending on its brightness, displace the peak out of the core position, especially in the case of one-sided structures. At some low level, we can test this effect with the data at 8.4 GHz, in a similar way as done in Fig. 4 by Dhawan et al. (2006) where one can see peak and "centroid" positions for 3.6 cm (i.e. 8.4 GHz). We strongly tapered the data at 8.4 GHz to reproduce the large beam at 2.3 GHz. We then fitted the peak positions in the low resolution maps obtained and compared them with those fitted in the maps of Fig. 1 (i.e. the points along the ellipse of Fig. 3). This test at 8.4 GHz, which can obviously not take into account resolved larger structures, measures differences between positions with a dispersion of 0.6 mas. This error adds quadratically to the error of about 0.7 mas associated with the scattering, resulting in the total error of ∼1 mas for the astrometry of LS I +61°303 given in Fig. 3-bottom. We note that with this value, which represents, however, only a lower limit to the error bars, there

is an overlap at each epoch at 2.3 GHz of the results from the different fitting programs, which can differ by up to 2 mas. We note that the 2.3 GHz astrometry has a general shift with respect to that at 8.4 GHz. This, as discussed in the next section, would correspond to the predictions of the core-shift effect. Owing to this effect, the peak of the emission (i.e. core) representing the optically thick part of the jet at one observing frequency, is predicted to have a shift from the center that is different for the different frequencies (Fig. 3-Top). This shift can also be seen in the 2.3 GHz astrometry of Dhawan et al. (2006) without the error bars. As in our case, Dhawan et al. ascribed the shift to a synchrotron opacity gradient along the emitting structure. However, in that case the structure is not thought to be a precessing jet but a cometary tail. Anything more than a general trend cannot be inferred from the 2.3 GHz data. As a result of our analysis of the data at 2.3 GHz, it is indeed clear that any quantitative comparison between the astrometry at 8.4 GHz and at 2.3 GHz (as well as between the orientation of the radio structures at the two frequencies) is unfortunately prevented by the very large Galactic scattering and the low resolution.

3.1.3 Precessing microblazar

Figure 3.3-bottom shows the results of the astrometry for the ν= 8.4 GHz data: the peaks of the consecutive images clearly trace an ellipse. Here, we show that this ellipse could be the cross-section of the precession cone, at the distance of the 3.6 cm-core (ν= 8.4 GHz) of the steady jet.

A magnetized plasma containing energetic electrons with a power-law energy distribution will produce a synchrotron power-law spectrum. However, below a critical frequency ($\nu_{\rm break}$), the radiating electrons will re-absorb some of the photons and as a result the typical spectrum of a uniform synchrotron source will show a peak at $\nu_{\rm break}$. Changes in the electron energy distribution and the decay of the magnetic field along the conical outflow forming the steady jet, imply that the critical frequency varies along the jet (Marscher 1995, Massi 2011a).

In microquasars, the $\nu_{\rm break}$ for the part of the steady jet closest to the engine (i.e., $\nu_{\rm break_1}$ in Fig. 3) lies in the infrared (Russell et al 2006), whereas in AGNs the observed turnover lies in the millimeter range (Marscher 1995). Observing at longer wavelengths than the infrared, i.e. in the radio band, gives rise to two results: a flat spectrum and the "core shift". Multi-wavelength observations result in the flat/inverted spectrum discussed in the introduction, which is typical of a steady jet. Imaging a steady jet at one observing frequency, $\nu_{\rm obs}$, gives rise to the effect known as "core shift", where the displacement from the center is a function of the observing frequency $\nu_{\rm obs}$. At $\nu_{\rm obs}$, the emission of the segment will dominate, whose spectrum peaks at that frequency plus small contributions from neighboring segments (see Fig. 1 in Markoff (2010)). With the engine being close to the "infrared-core", it is clear that the 3.6 cm-core can be displaced away from the orbit (as segment 2 is in Fig. 3 top-left). If a jet is pointing towards us (i.e., a microblazar as in Fig. 3 top-right), the core will be dominated by the approaching jet, because of Doppler boosting. If the jet is precessing, then the core will describe an ellipse (see Fig. 3 top-right). A transient jet, in contrast, can undergo any shift from the center, depending on the velocity and the time elapsed from the transient. The peak of map E, even if displaced away from the others,

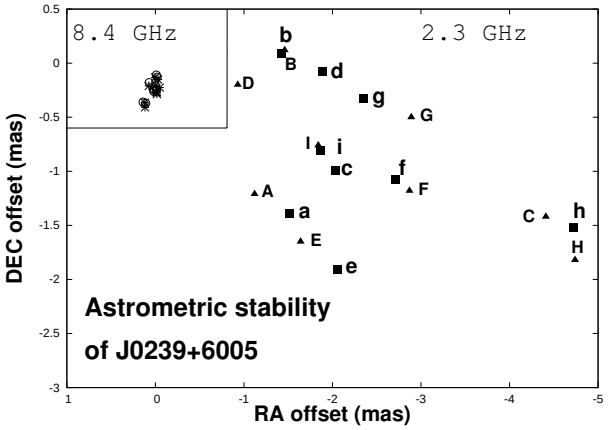

Figure 3.4: Control astrometry on the secondary calibrator. Relative positions of J0239+6005 with respect to J0244+6228, 2.5° apart. The astrometry at 2.3 GHz is indicated by squares (JMFIT) and triangles (MAXFIT); that at 8.4 GHz is indicated by crosses (JMFIT) and circles (MAXFIT).

and therefore likely affected by the approaching component of the transient jet, is at a position angle which is consistent that the other peaks. After 27 d, the peak of run I is rather close to completing the cycle, i.e. to overlapping with the peak of the starting run A. The same occurs for the peak of run J, that is 27 d after run B, a peak that nearly overlaps with peak B. The peak of run J, 30 d after run A, is clearly displaced from the A peak. The period therefore seems to be in the range 27-28 d.

3.1.4 Conclusions

Dhawan et al (2006) suggested that their VLBA observations of LS I +61°303 could probe the cometary tail of the pulsar model and that the peaks of all images traced an erratic ellipse. In this paper, we have re-analyzed this data set and have shown that

1. The larger dynamic range of the self-calibrated maps reveals that the radio emission has in several images a double-sided structure.

2. Our fit analysis show that the peaks of the images at 8.4 GHz trace a well-defined ellipse over a time interval of about 27-28 d.

The pulsar model explains neither the double-sided morphology nor the change from a double-sided to a one-sided structure. The microquasar model can explain them in terms of variable Doppler boosting, i.e., with a precessing jet. The cm-core of a precessing steady jet pointing close to our line of sight, as in a microblazar, is expected to describe an ellipse during the precession. In the transient jet phase, there will be an additional shift due to the approaching jet

component. We conclude therefore that the precession period is the time of about 27-28 d necessary to complete the ellipse.

As shown in Fig. 3.3, owing to the core-shift effect, the core at 2.3 GHz is expected to lie at a larger distance from the system center than at 8.4 GHz. However, because of the large scattering a proper astrometric analysis at 2.3 GHz is impossible. Future observations should be done at high frequencies. By measuring core positions at many frequencies in the AGN M87, it was possible to determine the frequency dependence of the shift and find the converging location of all observing-wavelength dependent cores. The six frequency observation of M87 proved that ν_{break_1} is at 43 GHz and that the 43 GHz-core is located within 23 Schwarzschild radii from the system center (Hada et al 2011). Similar observations for LS I +61°303 would be particularly interesting not only to prove whether ν_{break_1} is in the infrared as expected for microquasars, but in particular to test whether the different cores at the different frequencies all trace ellipses with different sizes and all with the same period, as shown in the sketch of Fig. 3.3. An accurate determination of the period is mandatory to establish the physical process responsible for precession. Massi & Zimmermann (2010) computed the precessional period for the accretion disk in LS I +61°303 under tidal forces of the Be star ($P_{\rm tidal-forces}$) and under the effect of frame dragging produced by the rotation of the compact object ($P_{\rm Lense-Thirring}$). By using those equations, we find that $P_{\rm tidal-forces}$ of 28 d would require the unrealistic value for the size of the accretion disk of $R_{\rm out} = 0.5 - 0.8 \times 10^{13}$ cm, i.e, nearly the semimajor axis, and can therefore be ruled out. In contrast, $P_{\rm Lense-Thirring} \simeq 28$ d would be realistic because it only implies a slow rotator with dimensionless spin parameter of $a_* = 0.5 \times 10^{-3}$. However, whereas our study firmly rules out tidal forces, there could be other processes than frame dragging at work in LS I +61°303 , which require a more accurate determination of the precessional period to be investigated. The orbital period is known with great accuracy and is P = 26.4960 ± 0.0028 d (Gregory 2002), whereas our determination of the precessional period indicates a period of about 27-28 d. Therefore, it is important to establish, with future observations, whether the two periods, orbital and precessional ones, are indeed similar but still different.

Addendum

These re-analysis by Massi, Ros & Zimmermann (2012) then corroborate the microblazar scenario with a precessing jet. Open issues are the production of the observed fast precession in a microquasar. The estimated period seems to be rather short - on a timescale of days - and as shown by Massi & Zimmermann (2010) not compatible with tidal effects of the companion star. Instead, Massi & Zimmermann (2010) propose General Relativity effects to play a role in the precession process, finding Lense-Thirring precession to be a feasible candidate. Lense-Thirring precession arises, when the space-time around a rotating compact object is dragged along inducing precession in an accretion disk/jet that is tilted with respect to the rotation axis of the compact object.

Independent timing analysis of 6.7 yr archival GBI data have now clearly revealed, apart from

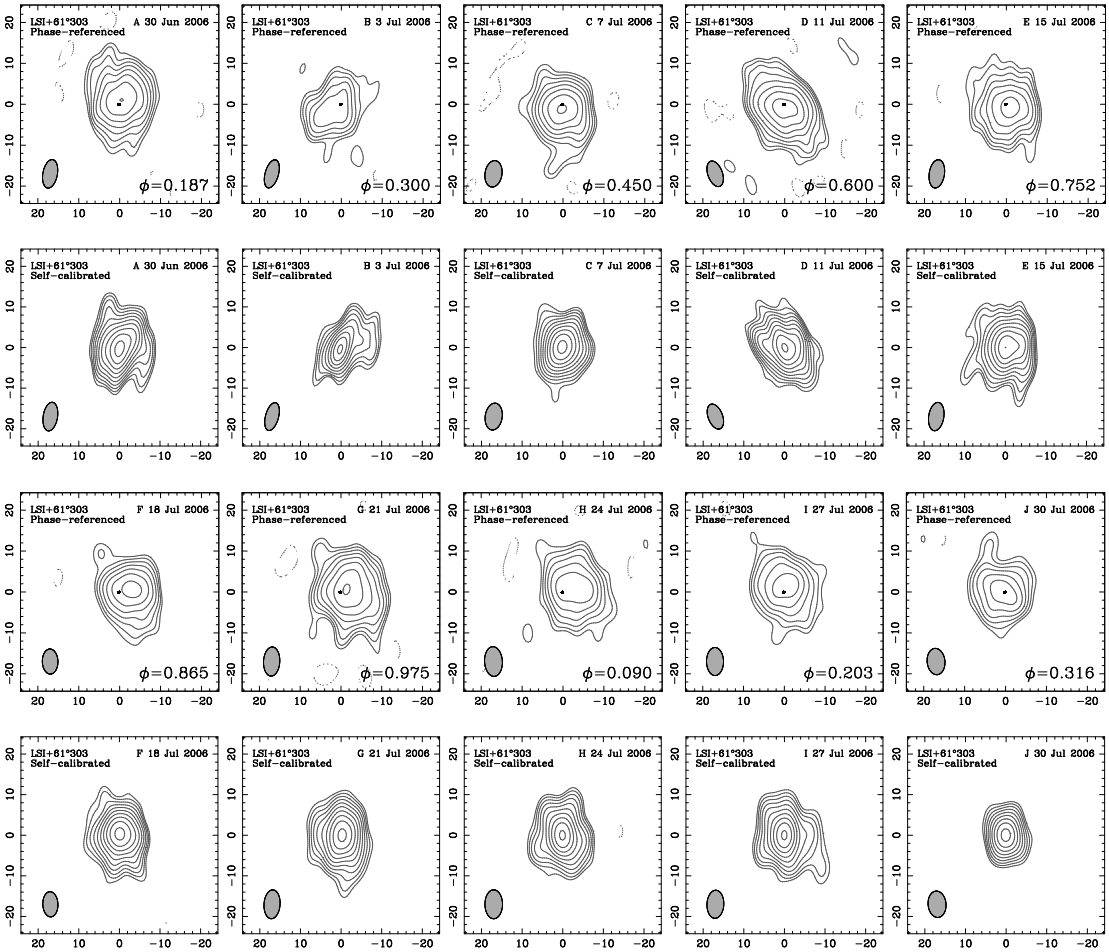

Figure 3.5: Top: Images of VLBA runs A-J at 13 cm (2.3 GHz) of LS I +61°303. For each run, two maps are presented, the phase referenced map and the self-calibrated map. Both maps are produced with uniform weight and the beam is 3.5 - 4.1 × 6.9 - 7.2. Contour levels for all maps are -4, 4, 5.66, 8, 11.3, 16, 22.6, 32, 45.2, 64, 90.5, 128, 181 σ (with 1σ=0.4 − 0.6 mJy/beam for phase-referenced maps, and 1σ =0.3 mJy/beam for self-calibrated maps.)

the orbital period of 26.45 ± 0.07 d, a second period of 26.92 ± 0.07 d (Massi & Jaron 2013). This is the same as the possible precession period as measured from VLBA observations (Massi, Ros, Zimmermann 2012). In fact, it shows that this second period of 26.92 ± 0.07 d is not the same as the orbital period of 26.45 ± 0.07 d. Intriguingly, the beat frequency of these two periods corresponds exactly to the long radio period of 4.6 yr (Massi & Jaron 2013).

In the next section, the VLBA data from BD117 are further analyzed with respect to the total flux density and the spectral index evolution during the observations. With this information, an attempt is made at identifying the jet components in the radio maps and at determining their parameters.

3.2 Spectral analysis of 2006 VLBA data

3.2.1 Total flux density evolution

The total flux density at 2.2 and 8.4 GHz was measured by comparing different methods. The first method measures the flux density from the baselines. An interferometer always bears the problem of zero spacing, which means that due to the systematic of an interferometer, no matter how good the u,v coverage, there remains a hole in the u,v plane, not sampled. This is particularly dramatic for very long baseline interferometers, while for tight arrays such as the VLA, it becomes negligible. This is why often single dish telescopes are used complementary to VLBI measurements to get total flux density measurements. This was not the case here. Two methods yield an estimate of the total flux density. The first estimate comes from measuring the flux density on the shortest baseline, which is the closest approximation to a single dish or a tight array. For the VLBA, the shortest baseline is the one between Los Alamos (LA) and Pie Town (PT), it is 236 km long. This baseline was included in all runs A-H, not in I and J. For runs I and J, the next shortest baseline, between Los Alamos and Fort Davis (FD), was evaluated, which is 608 km long. It yielded values comparable to the second method and is included in the error bars. The total fluxes densities on baseline LA-PT for runs A-H for 2.2 and 8.3 GHz are given in Fig. 3.6.

The second method uses the radio map to measure the total flux density. A clean window at the region including all relevant expected flux density is created (TVWIN in AIPS or left mouse click in Difmap). Statistics are run on this window (with IMSTAT in AIPS and key X in Difmap), which yields the peak flux density and its errors within the window. This is done for both frequencies. At 8.4 GHz, the source is clearly resolved. To make sure that this did not yield flux density losses, the flux density at 8.4 GHz was measured in a map created with the small beam (high resolution) and with a larger beam yielding the same resolution as for the 2.2 GHz data. The flux densities were compared and the differences included in the error bars in Fig. 3.7.

The total flux density at 8.4 GHz has a clear peak in run C, the rise is from B to C. In B the flux

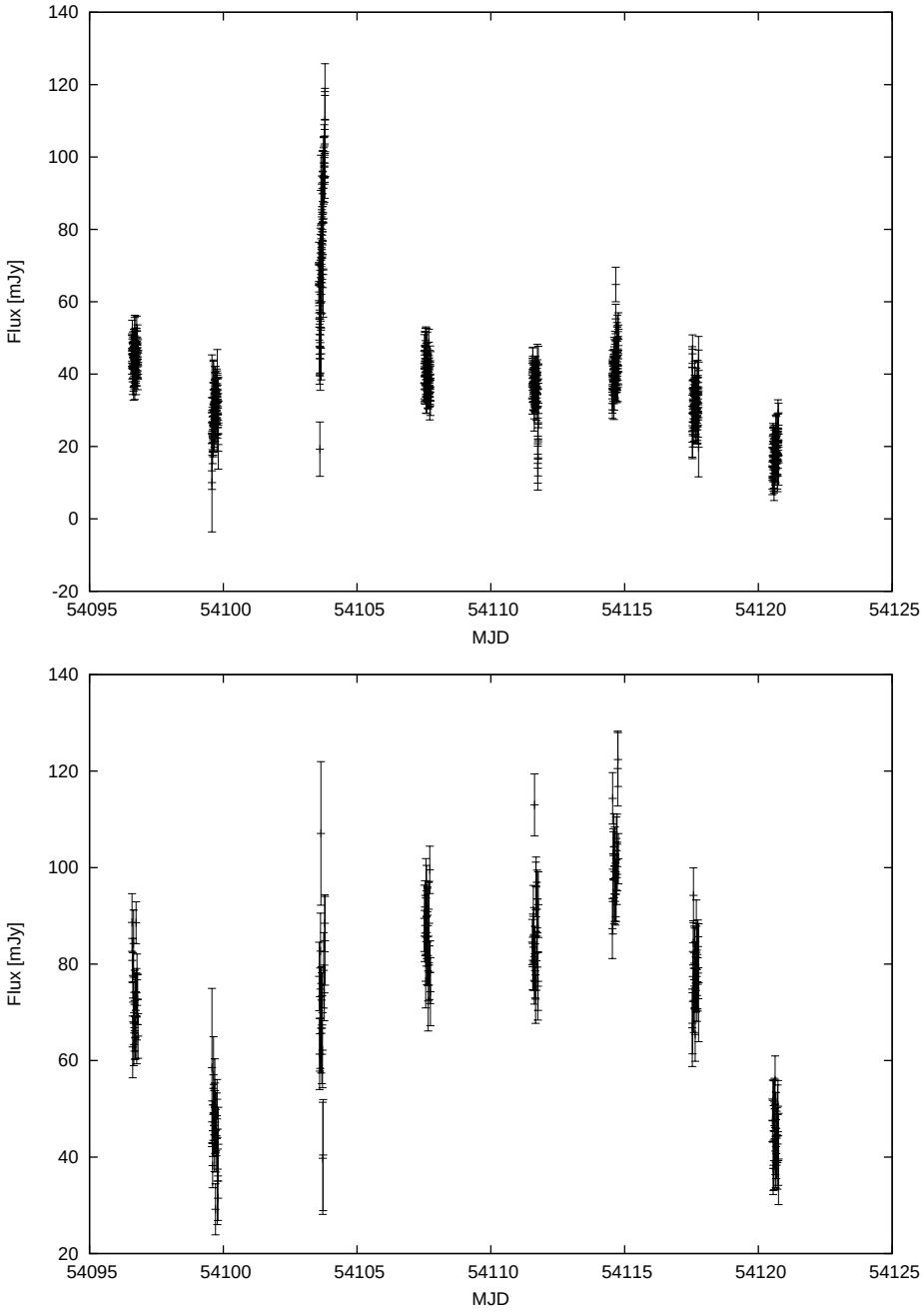

Figure 3.6: Total flux density measured on the shortest baseline LA-PT at 3.6 (top) and 13 cm (bottom) for runs A-H plotted against continuous orbital phase Φ.

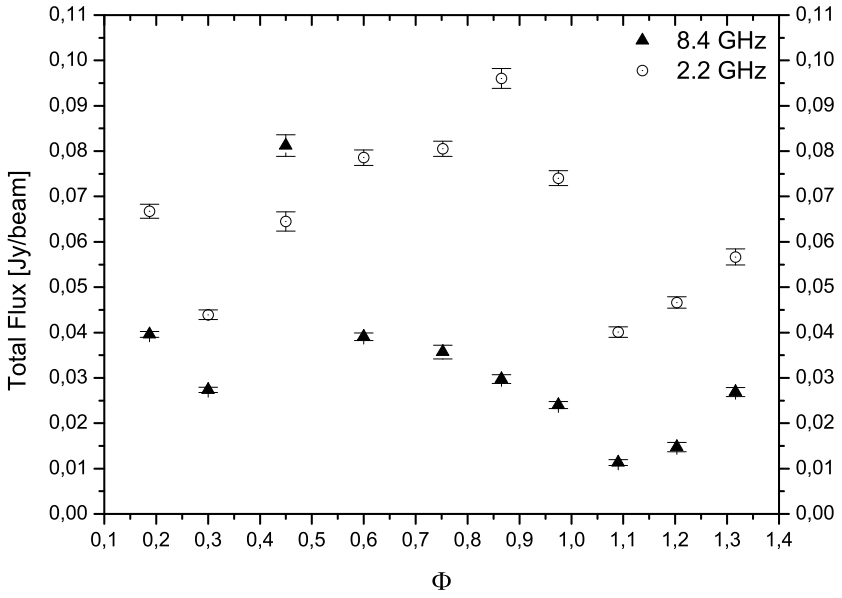

Figure 3.7: Total flux density for runs A-J plotted against continuous orbital phase Φ (Zimmermann, Massi & Ros 2012).

density lies around 25-30 mJy, in C it lies around 80 mJy. Then the flux density diminishes until the end of the orbital period (in runs I and J, not depicted in the figure), only a small rise is seen from run E to F. At 2.2 GHz, the evolution is different, the rise begins as well after run B, with a flux of around 45 mJy, but culminates only in run F, with a flux density of around 95 mJy. This is 9 days after run C. The flux density peak at 2.2 GHz is higher than at 8.4 GHz.

In comparison to the flux density measured on the shortest baseline (see Fig. 3.6), the flux densities are comparable. The baseline measurement has a large scattering, the average of the flux densities show nevertheless the same evolution as seen in Fig. 3.7. Run C lies around 80 mJy and run F around 100 mJy. The large scattering and the apparent switch in spectral index in run C demand a closer look though and will be investigated in more detail in the next section.

3.2.2 Spectral index evolution

The spectral index α was derived from the total fluxes S_1 (8.4 GHz) and S_2 (2.2 GHz) via:

$$\alpha = \frac{log(S_1/S_2)}{log(\nu_1/\nu_2)} \tag{3.1}$$

The errors $\Delta\alpha$ were calculated from gaussian propagation of uncertainty:

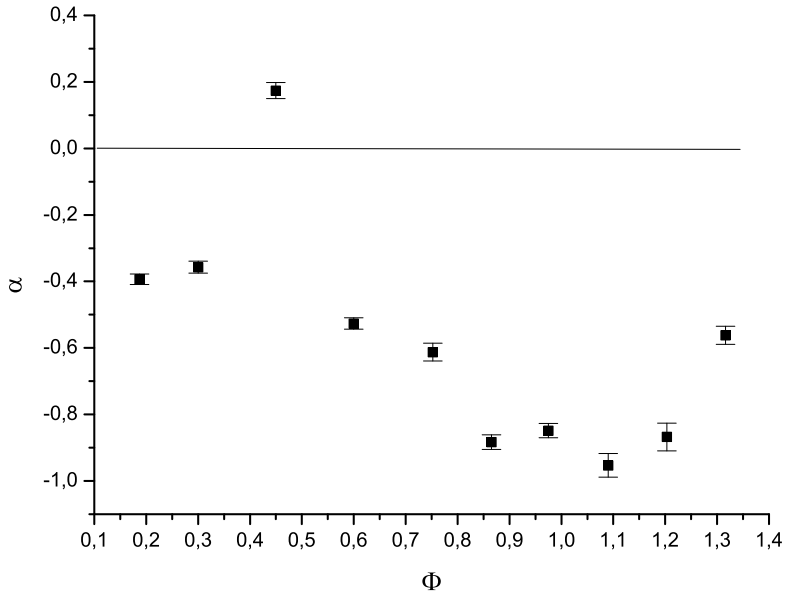

Figure 3.8: Radio spectral index α for runs A-J plotted against continuous orbital phase Φ (Zimmermann, Massi & Ros 2012).

$$\Delta\alpha = \frac{0.434}{log(\nu_1/\nu_2)} \sqrt{(\frac{\Delta S_1}{S_1})^2 + (\frac{\Delta S_2}{S_2})^2} \tag{3.2}$$

The spectral evolution given in Fig. 3.8 shows what was already hinted at in the total flux density evolution, the first flux peak is optically thick, the second one is optically thin. Without the total flux density, this result alone is not neccessarily due to two different particle populations. The high flux density at 2.2 GHz, higher than or at least equal to the peak at 8.4 GHz, nevertheless, corroborates this. As was noted before, in run C, the total flux density undergoes strong variations at both frequencies. Therefore the spectral index is also calculated in detail for the evolution during run C and the result is shown in Fig. 3.9 together with a more resolved look at the total flux density in run C on the baseline LA-PT.

Fig. 3.9 shows that the large scattering seen in Fig. 3.6 is due to the flare taking place during run C. During these six hours, the flux density rises from around 60 to 120 mJy. This yields then the average measured by both methods of around 80 mJy. This sheds a new light on the above argumentation. The flux density at 3.6 cm is now as high as the flux density nine days later at 13 cm during run F (the resolved evolution is given in Fig. 3.10). This weakens the argument that this second peak could not be due to adiabatic expansion. Nevertheless, a highly collimated jet would be neccessary to explain that after nine days the flux density has not decreased towards the lower frequency and this is contradicted by the radio maps. The steady jet is obviously destroyed

already in run E, where the central flux density is far away from the ellipse.

3.3 VLBI jet components

In this section, a closer look is given to the resolved structures at 8.4 GHz of the 2006 VLBA data. With the above attained knowledge of the spectral index, information about the upper limits of the velocity of the jet can be derived. There are two methods to do this, explained in the next paragraph. For one of the methods, it is neccessary to try and identify components of the receding and approaching jet. Gaussian components are therefore fit to the 8.4 GHz data in the following.

3.3.1 The apparent jet velocity

In a binary system, the jet points towards us at an angle θ, yielding an apparent jet velocity dependent on that angle. For the approaching and the receding component, the apparent velocity is:

$$\beta_{app} = \frac{\beta \sin\theta}{1 - \beta\cos\theta} \tag{3.3}$$

$$\beta_{rec} = \frac{\beta \sin\theta}{1 + \beta\cos\theta}, \tag{3.4}$$

where β is the actual jet velocity and θ the angle between the jet and the line of sight. The highly relativistic motion of the jet produces Doppler boosting of the emission, the relativistic Doppler factor again depends on the jet velocity and the angle between the jet and the line of sight θ:

$$\delta = \frac{1}{\gamma(1 - \beta\cos\theta)}, \tag{3.5}$$

with $\gamma = \frac{1}{\sqrt{1-\beta^2}}$ the usual relativistic factor. The angle θ determines the strength of the Doppler boosting and it is therefore negligible for large angles, but becomes highly relevant the closer the jet points in our direction (cite). The flux of the approaching and the receding jet component then becomes:

$$S_{app} = S_0[\frac{1}{\gamma(1 - \beta\cos\theta)}]^{k-\alpha} \tag{3.6}$$

$$S_{rec} = S_0[\frac{1}{\gamma(1 + \beta\cos\theta)}]^{k-\alpha}, \tag{3.7}$$

where α is the spectral index and k the jet parameter with k=2 for a steady and k=3 for a transient jet. The jet velocity β can then be derived by two methods. The first method works by estimating the flux in the receding and the approaching components of the jet through:

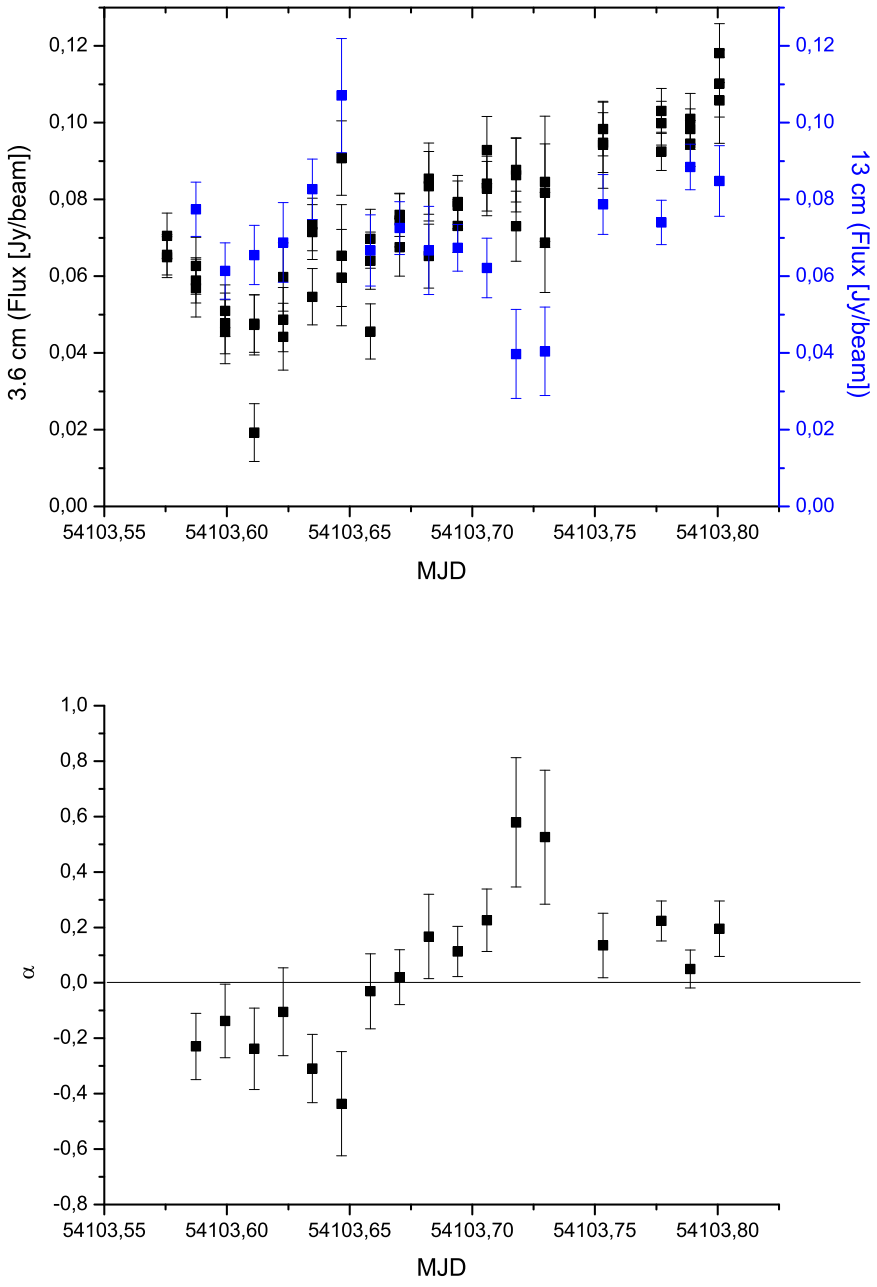

Figure 3.9: Top: Total flux density for run C from LA-PT at 3.6 and 13 cm. Bottom: Radio spectral index α for run C.

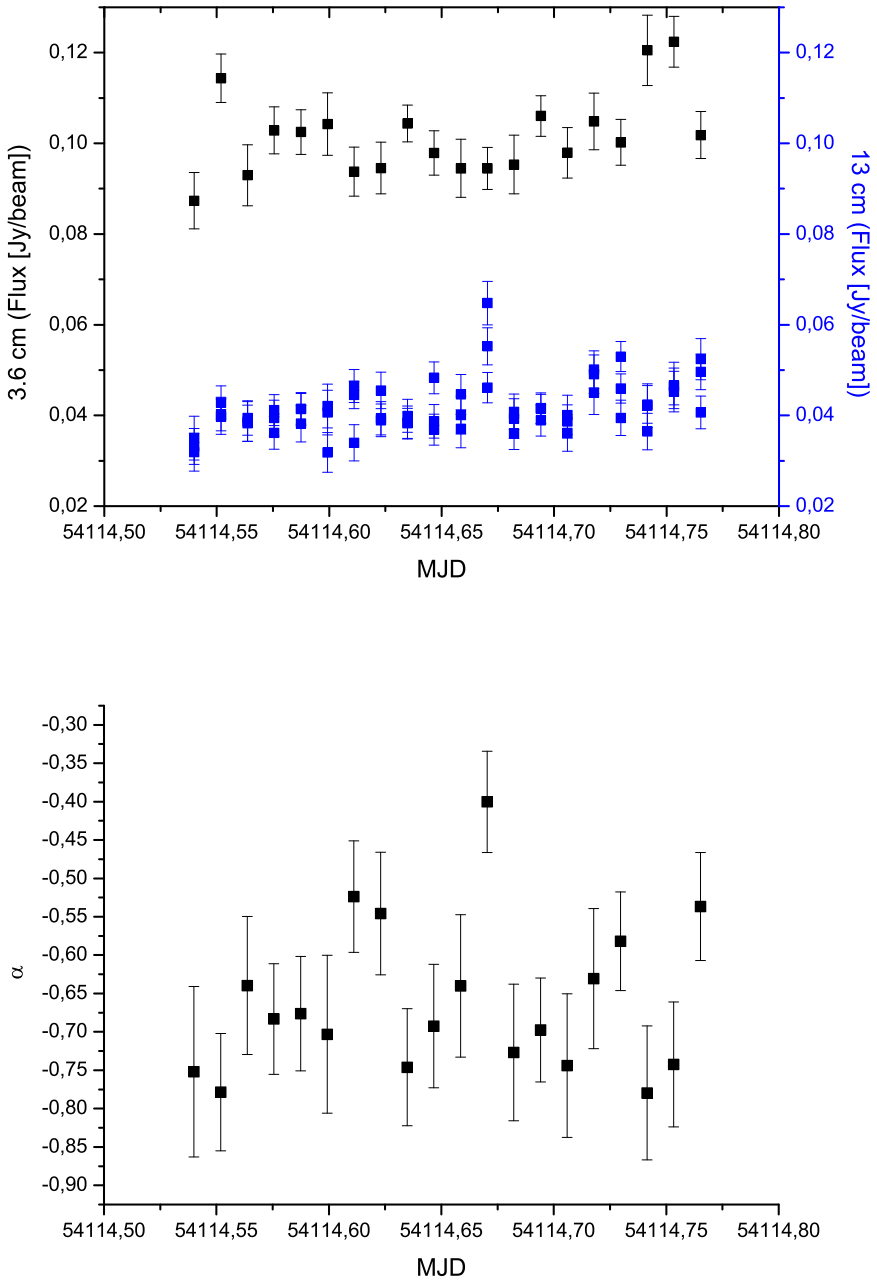

Figure 3.10: Top: Total flux density for run F from LA-PT at 3.6 and 13 cm. Bottom: Radio spectral index α for run F.

$$\frac{S_a}{S_r} = (\frac{1+\beta\cos\theta}{1-\beta\cos\theta})^{k-\alpha} \tag{3.8}$$

$$\Leftrightarrow \beta\cos\theta = \frac{(S_a/S_r)^{1/k-\alpha}-1}{(S_a/S_r)^{1/k-\alpha}+1} \tag{3.9}$$

where S_a is the flux density of the approaching and S_r the flux density of the receding jet component.
The second method uses the apparent length of the approaching (d_a) and the receding component (d_r), the apparent motion of the jet on the sky. Inserting

$$\beta_{app} = d_a \cdot \frac{D}{c} = \frac{\beta\sin\theta}{1-\beta\cos\theta}, \tag{3.10}$$

where D is the distance between the source and the observer and c the speed of light, into equation 3.3 yields:

$$d_a \cdot \frac{D}{c} \cdot (1-\beta\cos\theta) = \beta\sin\theta \tag{3.11}$$

Inserting respectively from equation 3.4 $\beta\sin\theta = \beta_{rec}\cdot(1+\beta\cos\theta) = d_a \cdot \frac{D}{c}(1+\beta\cos\theta)$, then yields:

$$\beta\cos\theta = \frac{d_a - d_r}{d_a + d_r}. \tag{3.12}$$

Nevertheless, without a concrete knowledge of the angle θ only upper limits of the velocity can be derived (for θ=0).

3.3.2 Theory of model fitting

After imaging a source through CLEAN and applying some self-calibration to improve the images, a model of components in the image can be done by fitting gaussian distributions to the believed components and evaluating their fit to the image (in AIPS) or directly to the visibility data (in Difmap). The difference between the model intensity distribution and the real intensity distribution I is determined by the maximum-likelihood method, yielding $\sigma^2 = \sum (M-I)^2$ (Fomalont 1999). The components are characterized by the position of the center of the gaussian component, its semi-major axis, its angle of the semi-major axis with respect to the north direction (which is declared 0) and its integrated intensity (Fomalont 1999).

Modelfitting with DIFMAP

In DIFMAP, the self-calibrated map is inspected visually and gaussian components are fitted by hand to the peak of the map and the suspected components. As a first step, only the core is fitted as a point source. The resulting position, flux density and size ratio is kept fixed in the following fitting process. After determining additional components, the residual map is inspected, if any

emission is missing. A least square fit is then run, minimising χ^2, where the parameters are the size and the flux density of the the gaussian components. The position and the size ratio of the components are kept fixed. Of course, the shape of the gaussian components are not determined, they could be circular or elongated. But DIFMAP tends to elongate existing gaussian components to fit diffuse emission, therefore the shape is kept fixed and assumed as circular as a first assumption (only run E was always fitted better with elongated components). The model can then be inspected via the map and also compared directly with the visibility data. If the residual map now shows emission left out, additional gaussians can be fit and the modelfit run again to improve the overall fit. This iterary process yielded the components as given in the next paragraph.

Modelfitting with AIPS

Within the task JMFIT up to three gaussian components can be fit to the radio map. The parameters of the gaussians can be entered directly into the input of the task. Fitting parameters like circular gaussians can be entered. The restriction to three components is the biggest disadvantage for fitting with AIPS, the modelfit within Difmap showed that not all runs cold be fitted with only three components without missing essential emission. Therefore, the following analysis were done with the components fitted with DIFMAP.

3.3.3 Gaussian components for the 2006 VLBA data

Tables 3.1 and 3.2 present the flux density of the gaussian components. The components fitted for runs A-J are shown in Fig.3.11 and 3.12. The components are identified as approaching or receding by following the argumentation that the approaching component should be stronger than the receding. The core is always by definition part of the approaching jet. Therefore, the flux density of the components in one direction (without core) are summed up and the components with the larger sum are then identified as approaching in Table 3.1 and 3.2 and added to the core component, which is always Ca1. The flux density errors of the components sum is calculated from the four sigma level of the radio maps in Fig. 3.11 and 3.12 via gaussian error propagation.

In Fig.3.13 the flux density from the modelled components at 8.4 GHz is compared for each run with the respectively measured total flux density. The flux densities are comparable, the cumulative flux density from the components tends to be slightly higher then the total flux density. The total flux density is measured in a map which is more resolved, which can lead to flux density losses.

	A	B	C	D	E
Φ	0.187	0.3	0.45	0.6	0.752
Ca1 [Jy]	0.0126	0.0143	0.0769	0.01607	0.0119
Ca2 [Jy]	0.007	0.0056	0.0143	0.0028	0.0148
Ca3 [Jy]	0.0188	0.0042		0.01357	
Ca4 [Jy]		0.0019			
Sum Ca [Jy]	0.0384	0.026	0.0912	0.03244	0.0267
Cr1 [Jy]	0.0092	0.0004		0.00386	0.0107
Cr2 [Jy]		0.0041		0.00087	
Sum Cr [Jy]	0.0092	0.0045		0.00473	0.0107
Sum Cp [Jy]	0.0476 ±0.0006	0.0305 ±0.0004	0.0912 ±0.0012	0.0372 ±0.0004	0.0374 ±0.0006

Table 3.1: Flux density of the gaussian components of the approaching (Ca) and receding (Cr) components for run A-E.

	F	G	H	I	J
Φ	0.865	0.975	1.09	1.203	1.316
Ca1 [Jy]	0.025	0.0148	0.0144	0.0178	0.0237
Ca2 [Jy]	0.013	0.0047	0.013	0.0032	0.0054
Ca3 [Jy]		0.0054	0.0018		0.0094
Ca4 [Jy]					
Sum Ca [Jy]	0.038	0.0249	0.0175	0.021	0.0385
Cr1 [Jy]	0.0017	0.0049	0.0013		
Cr2 [Jy]		0.0028	0.0007		
Sum Cr [Jy]	0.0017	0.0077	0.002		
Sum Cp [Jy]	0.0397 ±0.0006	0.0326 ±0.0006	0.0195 ±0.0004	0.0311 ±0.0012	0.0385 ±0.0004

Table 3.2: Flux density of the gaussian components of the approaching (Ca) and receding (Cr) components for run F-J.

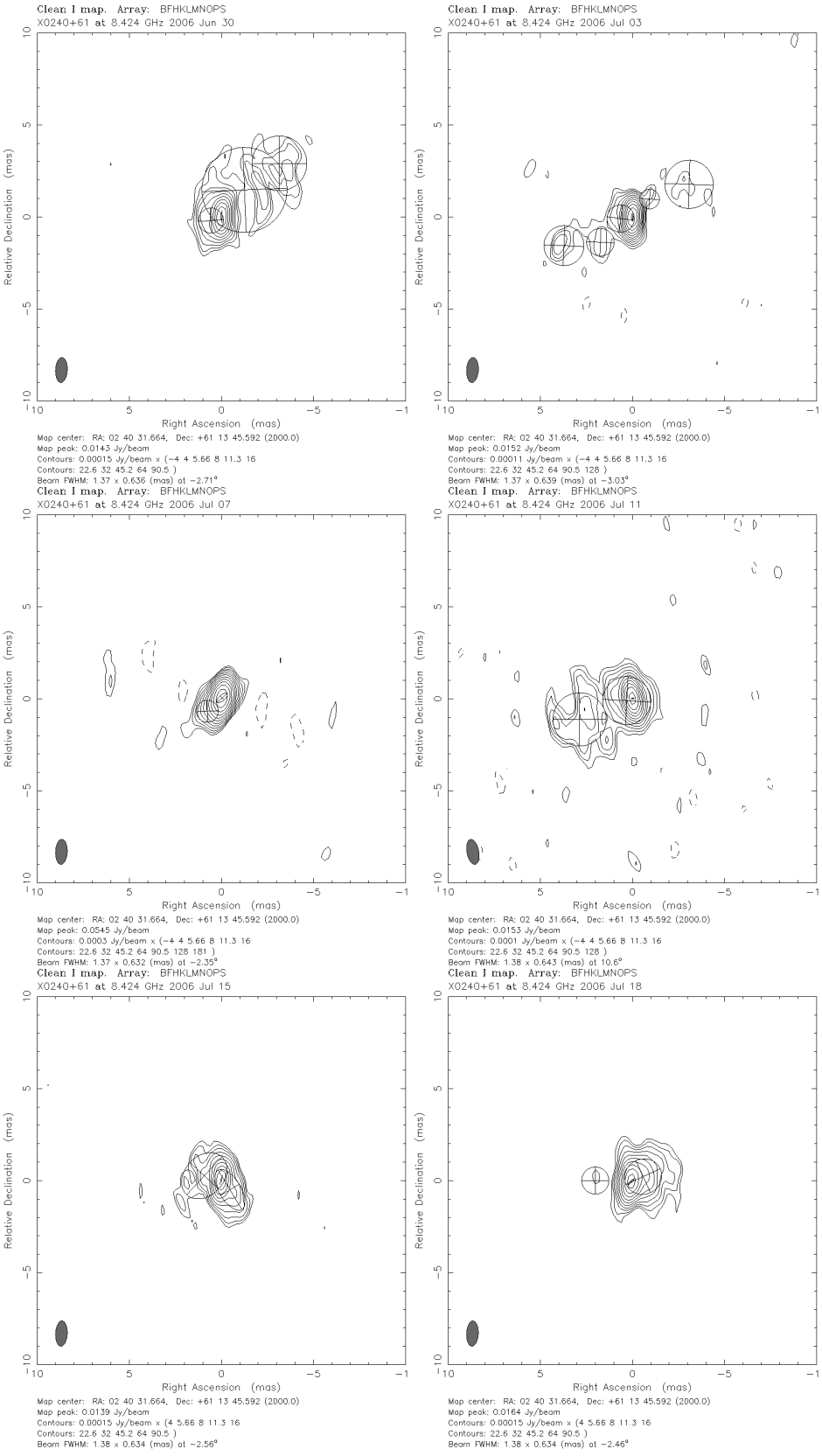

Figure 3.11: Self-calibrated mages of VLBA runs A-F at 8.3 GHz (3.6 cm) of LS I +61°303with modelled gaussian components for each run. The units on the axes are milliarcseconds (mas). Contour levels for all maps are -4, 4, 5.66, 8, 11.3, 16, 22.6, 32, 45.2, 64, 90.5, 128, 181 σ.

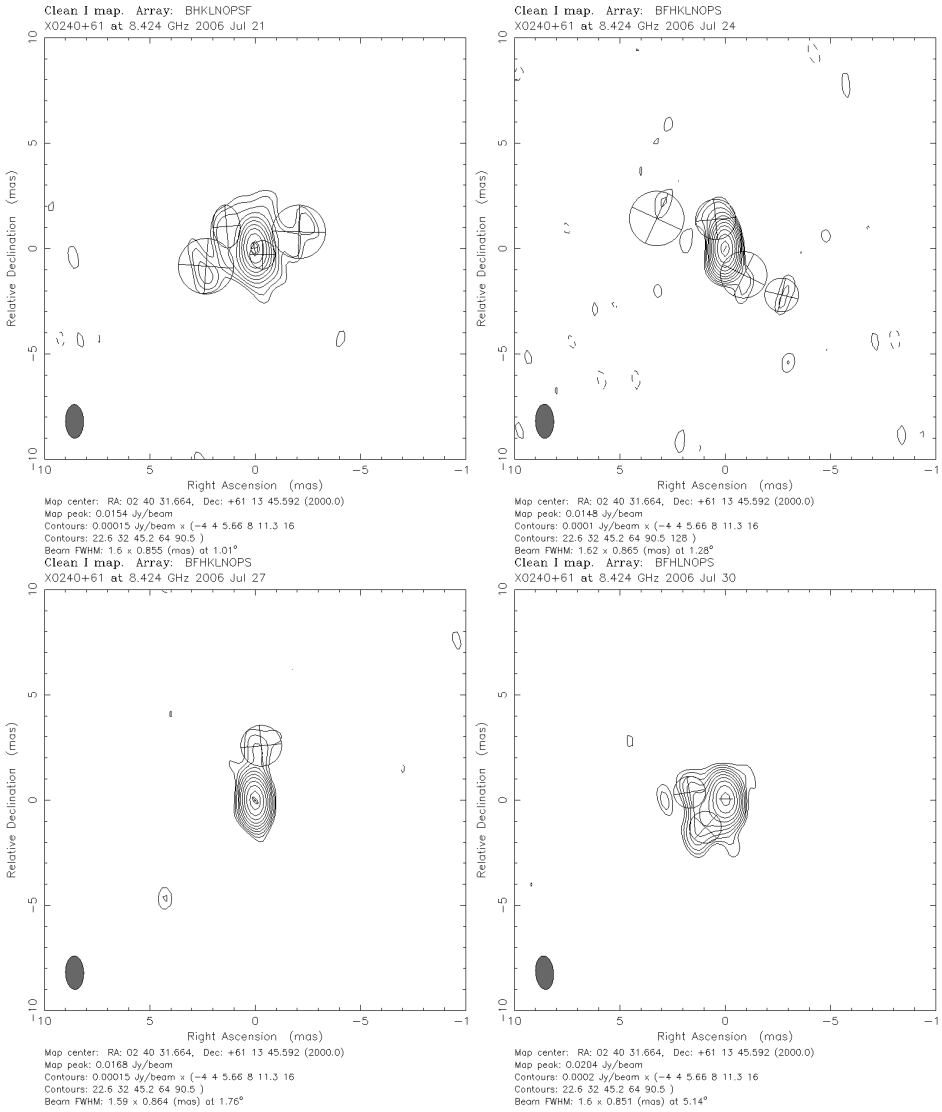

Figure 3.12: Self-calibrated mages of VLBA runs G-J at 8.3 GHz (3.6 cm) of LS I +61°303with modelled gaussian components for each run. The units on the axes are milliarcseconds (mas). Contour levels for all maps are -4, 4, 5.66, 8, 11.3, 16, 22.6, 32, 45.2, 64, 90.5, 128, 181 σ.

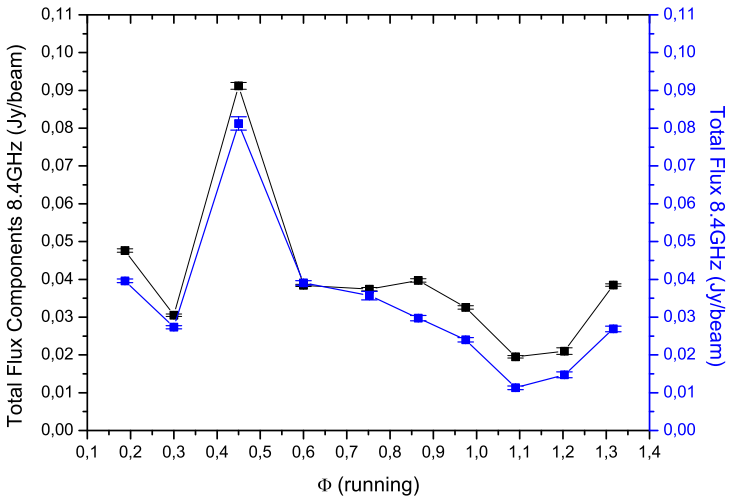

Figure 3.13: Total flux density vs. cumulated flux density of the modelled components (Sum Cp) at 8.4 GHz.

3.3.4 Measuring $\beta \cos \Theta$

Method 1

As explained above, the first method uses the flux density from the approaching (S_a) and receding components (S_r). Using S_a/S_r as given in Table 3.1 and 3.2, $\beta \cos \theta$ is derived and given in Figure 3.14 for k=2 and k=3. Two things must be noted. Even though run E was identified as a possible transient event, it is not possible to label any of the runs as transient or steady, especially as the components by themselves would need identification. Therefore, $\beta \cos \theta$ is calculated both for transient and steady parameters.

Method 2

To determine $\beta \cos \theta$ via method 2, the distance of the length of the receding and the approaching component needs to be identified. This method is of course only applicable for maps with two-sided structures, because the length of the receding component cannot be estimated. Fig. 3.1 is taken for the measurement of the pixel positions. There are now multiple ways what could represent the lenghts d_a and d_r. As the center, the core of the innermost gaussian component was chosen for all measurements. Then one can determine the length from i) the brightest feature to the middle, ii) from the outer edge to the middle, iii) from the middle between core and outer edge to the middle. Furthermore, this method can be applied to the phase-referenced and the self-calibrated pictures (natural and uniform weighting). The differences between these procedures yield the error bars for this method.

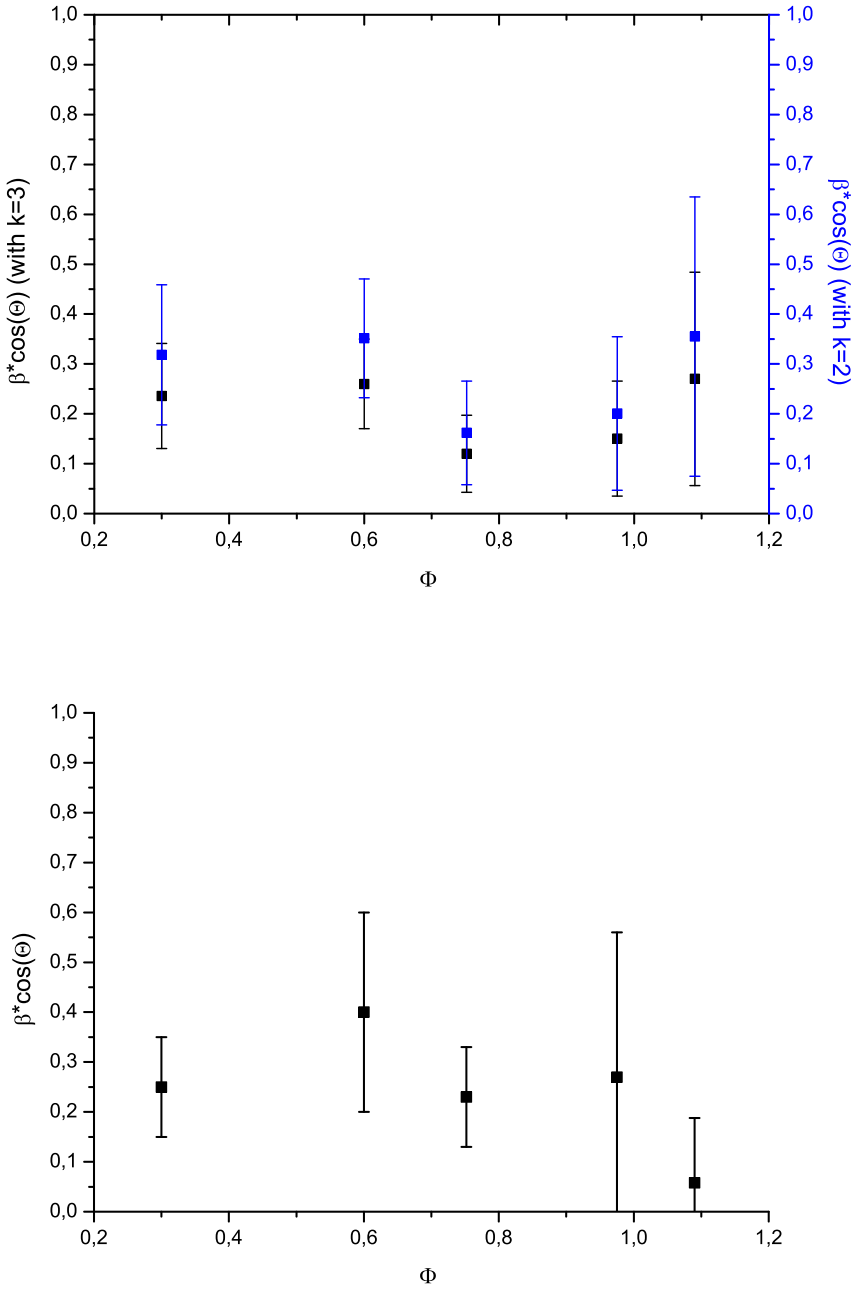

Figure 3.14: Top: $\beta \cos\theta$ estimated from method 1 for a steady (k=2) and a transient jet (k=3) for runs B, D, E, G and H. Bottom: $\beta \cos\Theta$ estimated from method 2 for runs B, D, E, G and H.

Comparing method 1 and method 2

In Fig. 3.14, the values of $\beta \cos\theta$ estimated from method 1 and method 2 are presented with error bars. The general evolution is the same for both methods. For the last run (run H) their is a higher discrepancy, but they are comparable within the error bars. From both methods, it becomes clear that $\beta \cos\theta$ never rises above ~0.65.

3.4 Conclusions and Discussion

Re-analysis of the morphology analysis and astrometry of the radio features seen in the 2006 VLBA data give strong evidence for a microblazar nature of LS I +61°303, where the jet is precessing with a period of ~27 days. In addition, the total flux density and spectral evolution of the 2006 VLBA data from LS I +61°303 at 8.4 and 2.2 GHz was analysed and possible jet components modelled. An estimate of the value for $\beta \cos\theta$ for each of the ten runs A-J gives an upper limit for $\beta \cos\theta$. To derive these values the spectral index needed to be derived from measuring the total flux density at the two frequencies, 8.4 and 2.2 GHz. It was shown that the spectral index undergoes an evolution along the orbit, not unlike the one seen in the radio spectral index analysis by Massi & Kaufman Bernado (2009) from GBI data. The radio spectral index switches from optically thin to a flat/inverted spectrum around $\Phi = 0.4$ characterized by an outburst dominated by the high frequency signal. After this the spectral index becomes negative again dropping to ever lower values. This is accompanied by a rise in the total flux density at 2.2 GHz, which reaches higher/equal values than the optically thick outburst. This excludes the origin of the second outburst to be caused by adiabatic expansion. On the contrary it fits the characteristics of an optically thin outburst, expected for microquasars after a sequence of optically thick emission (Fender et al. 2004). In fact, this sequence of an optically thick outburst followed by an optically thin outburst has been observed in LS I +61°303 before by Massi & Kaufman Bernado (2009). They furthermore find that this sequence is observed twice along the orbit during the maximum of the superorbital radio period of 4.6 yr. During the minimum though the ejection behaviour is less clear, though optically thin outburst and occasional optically thick outburst are seen as well. This is consistent with our findings, as the 2006 VLBA data was taken during the minimum of the superorbital period between Θ=0.32-0.33.

In the microquasar scenario, the radio spectral index behaviour observed by Massi & Kaufman Bernado (2009) is consistent with the two-peak accretion/ejection model proposed by, e.g., Marti & Paredes (1995), Bosch-Ramon et al. (2006), Romero et al (2007). During the minimum of the superorbital period, the two peaks are not expected to be strongly evolved, while during the maximum they are. Nevertheless, we find an optically thick ejection shortly after periastron, while the optically thin outburst occurs around apastron. Zooming in on the flux density behaviour in the six hours of run C, one sees that the the optically thick outburst seems to be preceeded by a small optically thin flare. The flux density evolution after the optically thick outburst is not recorded, and the existence/non-existence of an optically thin outburst or an adiabatic expansion

peak at lower frequencies can not be commented. It is possible though that the rise of the flux density at 2.2 GHz, seen in the following run three days later in D, could be due to adiabatic expansion, because it represents a plateau/small peak.

Even though Massi & Jaron (2013) confirm the existence of a second period corresponding to the ellipse's period at 8.4 GHz in the 2006 VLBA data, an independent measurement of the ellipse at another frequency is needed for several reasons. 1. To confirm that the cm-core traces an ellipse independently of frequency and observational period. 2. To again measure whether this ellipse has a period of 26.92 ± 0.07, in order to unambiguously relate the ellipse's period to the one measured in the timing analysis. 3. To investigate whether the ellipse becomes smaller at higher frequencies. The VLBA observations by Dhawan et al. (2006) were in fact done at two frequencies, but unfortunately, as seen in Fig. 2-Right, at 2.2 GHz the error bars are too large (∼1 mas) to fit an ellipse, due to large galactic scattering (see astrometry on the check source in Fig.3-Right). Following the idea of the core shift, when observing the source in the future at a frequency higher than 8.4 GHz, the steady jet in LS I +61°303 should trace a smaller ellipse within the same period of 26.92 ± 0.07, while at a lower frequency, the ellipse should be larger. A higher frequency, though, also yields a higher resolution, and indeed LS I +61°303 has never been imaged at a frequency higher than 8.4 GHz with the VLBI technique. Observing LS I +61°303 at a high frequency can then both measure the ellipse and its period with a high precision and image the radio morphology at very high resolution. By determining the parameters of the two ellipses at the two frequencies we can then derive with our model the precession angle and the distance of the radio cores from the central engine.

Chapter 4

Broad-band radio spectral analysis of LS I +61°303 with the Effelsberg 100m telescope

4.1 Radio spectral analysis of LS I +61°303

Previously, Strickman et al. (1998) analysed multifrequency VLA observations covering sparsely one orbit and found deviations in the radio spectrum from a simple power law during the outburst. The radio spectral analysis by Massi & Kaufman Bernado (2009) used 6.7 years of NASA/NRAO GBI data from LS I +61°303 at two frequencies, ν_1 = 2.2 GHz (13 cm wavelength) and ν_2 = 8.3 GHz (3.6 cm wavelength) and yield two results. One is that the large radio outburst towards apoastron consists of an optically thick outburst, where α may rise up to $\alpha \simeq$0.1-0.4, and is sometimes immediately followed by a new outburst, this time an optically thin one, where α may reach the minimum value of $\alpha \simeq -0.4$ (with $S \propto \nu^{\alpha}$). The other result of the radio spectral analysis is that this α evolution from mostly positive to negative values, not only occurs during this large 100-500 mJy outburst, but also close to periastron passage. This is puzzling, because only negligible flux peaks are observed at that orbital phase .

From Chapters 3 and 4, it follows that the radio spectral index is a unique tool to investigate the real nature of this enigmatic radio-TeV source. The aim was therefore to extend these analysis to several radio frequencies in order to get new and complete spectral index information (in contrast to the archived GBI data at only two frequencies) and to compare those with the continuously running observations at high energies (e.g. with *Fermi*-LAT). Here, are presented the spectral results from 25 observations carried out with the 100m-Effelsberg telescope during one orbit of LS I +61°303 at 4-7 wavelengths: 0.9, 1.3, 2.0, 2.8, 3.6, 6.0 and 11cm (32, 23, 14.6, 10.5, 8.4, 4.85, 2.6 GHz).

The broad band radio spectral analysis, done by Strickman et al. (1998) using the VLA, covered more than one entire orbit (from 0.97-0.07). The sampling though differed between $\Delta\Phi$=0.03

and 0.2 and this biggest gap, 5 days, lies during the rise of the outburst. From our observations we see that the complete rise of the flare occurs within only 3 days, a 5-day gap means that the peak of the outburst could have already started to decay before the next measurement was taken. Alltogether, 16 observations with the VLA were carried out, 14 observations at 5 or 6 frequencies and 2 observations at 3 frequencies (Strickman et al 1998). This led us to apply for a multi-frequency monitoring with a denser sampling covering a full outburst with the Effelsberg 100m telescope. We tried for a strictly regular sampling of one observation each 12 hours for the first 10 days at cm- to mm-wavelengths. This was successful within 2-3 hours (Φ=0.01). In order to be able to detect spectral changes/switches as well as delays between frequencies, such a sufficiently dense time sampling is required. From Fig. (Flux), one sees that the onset of the outburst has a duration of roughly $\Delta\Phi = 0.1 \approx 2.6$ d with even faster variations superimposed. Observations every 12 hours are therefore the minimum to cover the expected delay among frequencies during the spectral evolution in the outburst. In terms of the superorbital period Θ, our observations were during Θ=0.59-0.6, while Strickman et al during Θ=0.69-0.7.

4.2 Observations and data reduction

4.2.1 Single-dish vs. interferometer

LS I +61°303 lies close to the large W4 HII region (see Fig. 3 in Marti et al 1998). Several radio sources, associated with this HII region are found in a vicinity of arcmin of LS I +61°303 (see Fig. 2 in Marti et al. 1998). Their emission is mostly thermal free-free emission (Marti et al 1998). Therefore, up till now, LS I +61°303 has been observed with radio interferometers, because with their high resolution they manage to solely observe the weak emission from LS I +61°303. The small beam (resolutions of milli-arcseconds for the VLA and the VLBA) does not sample the surrounding emission from the HII region. A single dish telescope like Effelsberg has a lower resolution and runs the risk of sampling this additional emission. Now these observations here show that due to the scan technique used with Effelsberg, applicable even for such a weak source like LS I +61°303, a clear baseline can be identified, which allows to measure the comparably weak flux without confusion. Only at 11cm, the large beam and respectively long scan length pose a problem at certain scanning angles.

4.2.2 Observations with the Effelsberg 100m telescope

The clearly defined radio periodicities in LS I +61°303 allowed us to directly schedule observations to cover the large radio outburst around apastron. The long period Θ modulates the flux and the orbital occurence of the outburst. The switch from an optically thick to an optically thin spectrum was expected to occur in the orbital phase interval 0.3-0.7. The observations were then scheduled in March and April 2012, starting on March 26th (Φ=0.28) and finishing on April 19th (Φ=0.2).

Epoch	MJD	S_{110mm} [mJy] 2.6 GHz	S_{60mm} [mJy] 4.85 GHz	S_{36mm} [mJy] 8.4 GHz	S_{28mm} [mJy] 10.5 GHz	S_{20mm} [mJy] 14.6 GHz	S_{13mm} [mJy] 23 GHz	S_{9mm} [mJy] 32 GHz	Phase Φ
1	56012.704		19.5 ± 1.1	14.4 ±0.7	16.1 ±0.3	17.5 ±1.8	73.8 ±13.1		0.28
2	56013.201		21.1 ±0.8	21.5 ±0.6	20.2 ±1.6	17.6 ±1.3	69.3 ±7.3	15.2 ±3.5	0.3
3	56013.790	43.5 ±3.2	56.7 ±1.2	55.5 ±0.9	53.3 ±2	47.6 ±2.7	61.8 ±10.3	68 ±29.5	0.32
4	56014.173	115.3 ±3.8	113.4 ±1.5	107.7 ±2.5	100.6 ±	79.5 ±5.5	76.1 ±14.2		0.33
5	56014.741	107.6 ±2.9	129 ±1.7	114.8 ±1.5	100 ± 2.6	90.6 ±5.5	80.5 ±13.9		0.35
6	56015.187	140.6 ±3.1	120.4 ±1.7	109.5 ±1.5	110.9 ±3.6	89.4 ±4.2	108.2 ±12.3	71 ±20.7	0.37
7	56015.696	154.4 ±3.1	161 ±1.9	134.4 ±1.8	125.9 ±3.4	109 ±5	142.1 ±26	89.9 ±13.4	0.39
8	56016.165	167.4 ±3	179.7 ±2.2	168 ±3.9	159.1 ±4.7	126.6 ± 11.3	125.6 ±23.5	83.9 ±19.2	0.41
9	56016.698	184.9 ±3.8	191.9 ±2.5	185.6 ±4.5	176.1 ± 4.3	151.6 ± 8.3	157.3 ±28.8	87 ±13	0.43
10	56017.210	160.4 ±3.4	165.3 ±2.2	157.5 ±2.9	168.7 ±3.8	152.8 ±7			0.45
11	56017.721	163.3 ±4.2	180 ±1.9	152.5 ±2.8	134.6 ±3.8	87.3 ±4.4			0.47
12	56018.077	163.6 ±3.7	156.3 ±2.1	109 ±2.9	111.5 ±5.1			64.9 ±7.5	0.48
13	56018.745	135.7 ±3.4	131.2 ±1.9	118.8 ± 2.5	116.6 ±4	104.9 ±4.8	116.7 ±28.2	113.8 ±41.8	0.50
14	56019.737	125.9 ±3.4	112.6 ±1.8	87 ±	78.1 ±2.7	61.1 ±3	43.1 ±11	49.2 ±12.6	0.54
15	56020.145	109.6 ±2.1	92.5 ±1.8	78.6 ±2.2	67.7 ±2.6	37.5 ±3		45.5 ±7.5	0.56
16	56020.676	118.9 ±3.2	110.5 ±1.7	89.4 ±1.3	76.1 ±2.5	59.5 ±3.1	45.2 ±11.3	36.2 ±12.3	0.58
17	56021.145	122.6 ±3.3	111.1 ± 1.6	109.1 ± 1.6	87.7 ±2.7	77.4 ±3.6	78.8 ±18.4		0.6
18	56021.713	107.6 ±2.9	98 ±1.4	74.6 ±1.1	64.7 ±2.4	53.9 ±2.9	76.5 ±13.8		0.62
19	56022.194	86.2 ±1.5	78.9 ± 1.5	62.8 ±0.9	57.3 ±2.1	43.5 ±2.2	45.8 ±12.1	58.1 ±14.7	0.64
20	56023.152	80.2 ±2	66.7 ±1.2	60.5 ±0.9	76.9 ±2.2	88.1 ±4.1			0.67
21	56024.080		98.8 ±	83.8 ±1.2	74.1 ±2.9	57.3 ±3.2			0.71
22	56025.089		78.8 ±	58 ±1	52.9 ±1.8	50.9 ±3.7			0.74
23	56025.953		64 ±1.1	51.1 ±0.9	45.9 ±2	31.1 ± 2.4			0.78
24	56030.146	59.7 ±1.9	49.1 ±1.1	35.2 ±0.8	32.9 ±2.2	26.8 ±2.3			0.94
25	56037.208		20.2 ±0.8	13.5 ±0.6	12.1 ±2.2	12.9 ±2	49.2 ±18.9		0.2

Table 4.1: Log of the Effelsberg observations in March/April 2012. The corresponding orbital phases have been computed using the formalism in Gregory (2002).

LS I +61°303 was observed on 11 consecutive days roughly every 12 hours (see Table 4.1 for exact dates) at four core wavelengths (6, 3.6, 2.8 and 2 cm) with the Effelsberg 100m telescope, covering the large radio outburst of the source towards apastron. On most of these days, we obtained also measurements at 11, 1.3 and 0.9 cm wavelength. After these 11 days, 6 additional days were granted to us upon request to cover the complete decay of the outburst. The log of the observations is given in Table 4.1. On MJD 56019, only one measurement was taken in 24 hours, because unfortunately due to a technical problem, the telescope was out of order for several hours. The epoch was added at the end of the observations (MJD 56022.194).

The flux density measurements at the Effelsberg 100m radio telescope of the MPIfR are described in detail in Fuhrmann (2004) and Fuhrmann et al. (2008). LS I +61°303 is a rather weak source with a flux density ranging from less then 20 mJy during quiescence to up to more then 200 mJy during its outburst. This was nevertheless sufficiently strong in the observed frequency range to allow for flux density measurements using cross-scans (azimuth/elevation direction) with the number of sub-scans matching the source brightness at the given frequency (see Heeschen et al., 1987; Quirrenbach et al., 1992; Kraus et al., 2003, for details). The source is scanned in azimuth and elevation over a distance of approximately 4 times the beam width. The resulting distribution is a convolution of the telescope beam with the source brightness distribution. This yields an intensity curve, which can be fitted with a gaussian profile to derive the amplitude, because the target source LS I +61°303 and all the calibrators are pointlike within the telescope beam. The number of neccessary cross-scans depended on the brightness of the source, which varied strongly during the observations. Especially at the beginning and the end of the observations, where the flux was very low, the number of cross-scans was enhanced strongly to guarantee a sufficient signal-to-noise ratio.

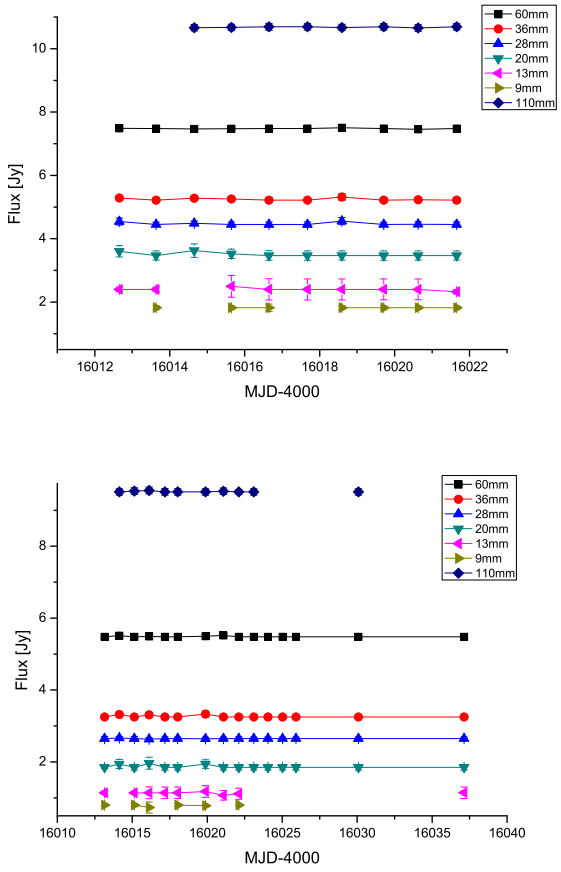

Figure 4.1: Top: Flux density of the main calibrators 3C48 during the observations. Bottom: Flux density of the main calibrator 3C286 during the observations.

During each epoch, first a calibrator and then LS I +61°303 was observed consecutively at all four core wavelengths (in the order 2, 2.8, 2.6 and 6 cm (14.6, 10.5, 8.4 and 4.85 GHz)) and if time and conditions allowed also at 11, 1.3 and 0.9 cm wavelength (2.6, 23 and 32 GHz). A second calibrator was observed at the end of an epoch, if time allowed. Each epoch lasted about 2-3 hours.

4.2.3 Data reduction

The data reduction was then done in the standard manner, and is described in e.g. Kraus et al. (2003); Fuhrmann (2004) and Fuhrmann et al (2008). The first step of the data reduction of the flux density measurements were performed with the software TOOLBOX, provided by the MPIfR. TOOLBOX fits each subscan with a gaussian curve and subtracts the baseline.

This fit can then be inspected for all individual subscans. The criteria for a good fit are the full width half maximum (FWHM), the pointing offset and the amplitude. Overall, offsets/differences from more than +- 10% would in general end in flagging of the subscan. Nevertheless, with LS I +61°303 being such a weak source, this flagging was done very carefully, as with each flag information was also lost. After inspection of each subscan, the subscans (and afterwards consecutive scans) were averaged for a better signal-to-noise ratio and the final fit was obtained. In the next step, the data was corrected for pointing offsets, which corrects the amplitude of the gaussian fit, and then corrected for atmospherical disturbances using the CORR_POINT program. These opacity corrections were based on five year opacity data from the F-Gamma program, yielding average values for good, average and bad weather.

The final calibration was then applied by first correcting the remaining systematic gain-elevation and then the measured antenna temperatures for each observed source were linked to the absolute flux-density scale, using the frequent primary calibrator measurements (Baars et al., 1977; Ott et al., 1994). The flux densities for the primary calibrators for the frequencies used in the experiment are given in Table 4.2. Owing to the weakness of the source, the individual flux density errors derived during the calibration process were compared with the repeatibility errors from five years of the F-Gamma monitoring program and the calibration factor variance of our observations. The most conservative approach was then chosen, in order not to underestimate the flux density errors.

For the data reduction, the small wavelengths posed the biggest challenge, because of the overall low fluxes and the strong dependence on wheather conditions. Additionally, on the first two days, the 1.3 cm and 0.9 cm wavelength receiver were not working properly. The high flux densities measured for 1.3 cm in Epoch 2, 3 and 4 (MJD 56013.20, 56013.79 and 56014,17) should therefore not be overinterpreted. The measurements at 0.9 cm look alright in terms of the scan quality, but nevertheless the calibration factor in Epoch 3 is very high, demanding again a careful interpretation of these data points. The rather high value at 1.3 cm in the last epoch, 25 (MJD 56037.2), is difficult as well, as the cloud coverage changed substantially during the observations, which is not much of a problem until 2 cm, but again, at 1.3 cm this makes enough difference, especially for the very low quiescent fluxes. Measurements at 1.3 cm wavelength that could not be fitted due to weather conditions were obtained in Epoch 11, 12, 13 and 15 (MJD 56017.72, 56018.07, 56018.74 and 56020.14), for 2 cm wavelength, only Epoch 12 (MJD 56018.07) was not fittable. Measurements at 0.9 cm wavelength were not always available, because of time restrictions. When available, they were always of good quality.

The measurements at 11 cm wavelength posed an additional challenge due to the large beam width at this wavelength (260 arcsec). In some epochs the large beam sampled additional emission, which led to a non-symmetric profile of the subscans. Most of the times only one scan direction was strongly affected, depending on the position angle during the cross-scans. In these cases, only the unaffected direction was used for the data reduction. A pointing correction was then not possible, because both directions are needed. But the pointing offset was below 5% in all cases.

Calibrator	$S_{110mm}[Jy]$	$S_{60mm}[Jy]$	$S_{36mm}[Jy]$	$S_{28mm}[Jy]$	$S_{20mm}[Jy]$	$S_{13mm}[Jy]$	$S_{9mm}[Jy]$
3C286	10.69	7.48	5.22	4.45	3.47	2.40	1.82
3C295	12.46	6.56	3.47	2.60	1.69	0.89	0.55
3C48	9.51	5.48	3.25	2.65	1.85	1.14	0.8
3C161	11.35	6.60	3.88	2.95	2.12	1.25	0.83

Table 4.2: Primary calibrator values used for the observations (cite).

In Fig. 4.2, 4.3, examples for flux density scans at 6 cm wavelength are given for the quiescent (before the flare) and the high state (during the flare). In Epoch 2 (MJD 56013.20), the flux density at 6 cm is weak (Fig.4.2), but the source is seen in all the scans, even if not all single scans are fitted and in some cases the baseline is crocked. Flagging of such subscans (subscan 20, 22 or 23) does not yield a better fit of the average scans, though. Therefore all scans were included in the final fitting. For Epoch 9 (MJD 56016.69), in the middle of the flare, the subscans at 6 cm show a clear signal and the average as well (Fig.4.3).

In Fig. 4.1, the flux densities of the two main calibrators 3C48 and 3C286 are shown for the observations. The flux density shows no significant variability over the observations.

4.3 Data Analysis and Results

4.3.1 Total flux density variability

The total flux density evolution at all and at the four main wavelengths are shown in Fig. 4.4. After Φ=0.3 (Epoch 2, MJD 56013.20), the flux rises steeply from around 20 mJy to around 100 mJy within 24 hours (until Epoch 4, MJD 56014.17), remains at that level and then after another 24 hours (from Epoch 7, MJD 56015.69), it rises yet again to the highest level of around 200 mJy. Then follows the slow decay of the outburst intersected by smaller rises in Epoch 13, 17 and 20 (MJD 56018.74, 56021.14 and 56023.15). In Epoch 25 (MJD 56037.20), corresponding to Φ=0.2, the flux has again reached the level from the beginning of the observations.

4.3.2 Spectral index

The main goal of the observations was to follow in detail the broad-band spectral evolution during the radio flare. To analyse the spectral index evolution, the spectrum was derived for each epoch using a polynomial fit ($y = b * x^a$). As a fitting program, gnuplot was used. In Fig. 4.5, 4.6 and 4.7, the spectra and the spectral fit for each epoch are shown, covering 25 days (from Φ=0.27 to Φ=0.2). In Fig. 4.8-Top the spectral indices from these fits are given. The average spectral index from these values is $\alpha = -0.2 \pm 0.17$. The maximum value is α-0.0012 and the

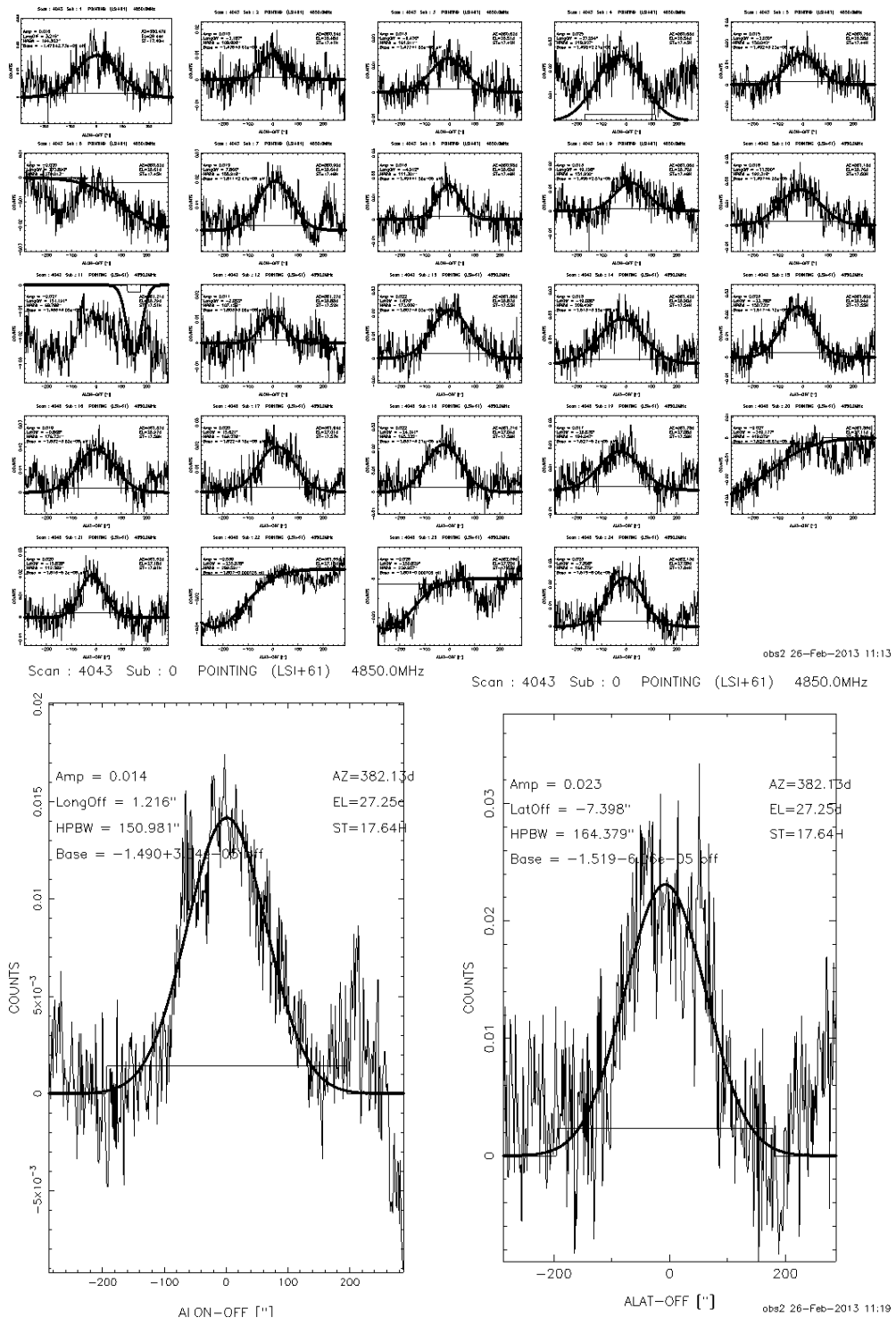

Figure 4.2: Scans at 6 cm wavelength from Epoch 2 (MJD 56013.20). Top: All subscans in elevation and azimuth. Bottom: Average over each direction

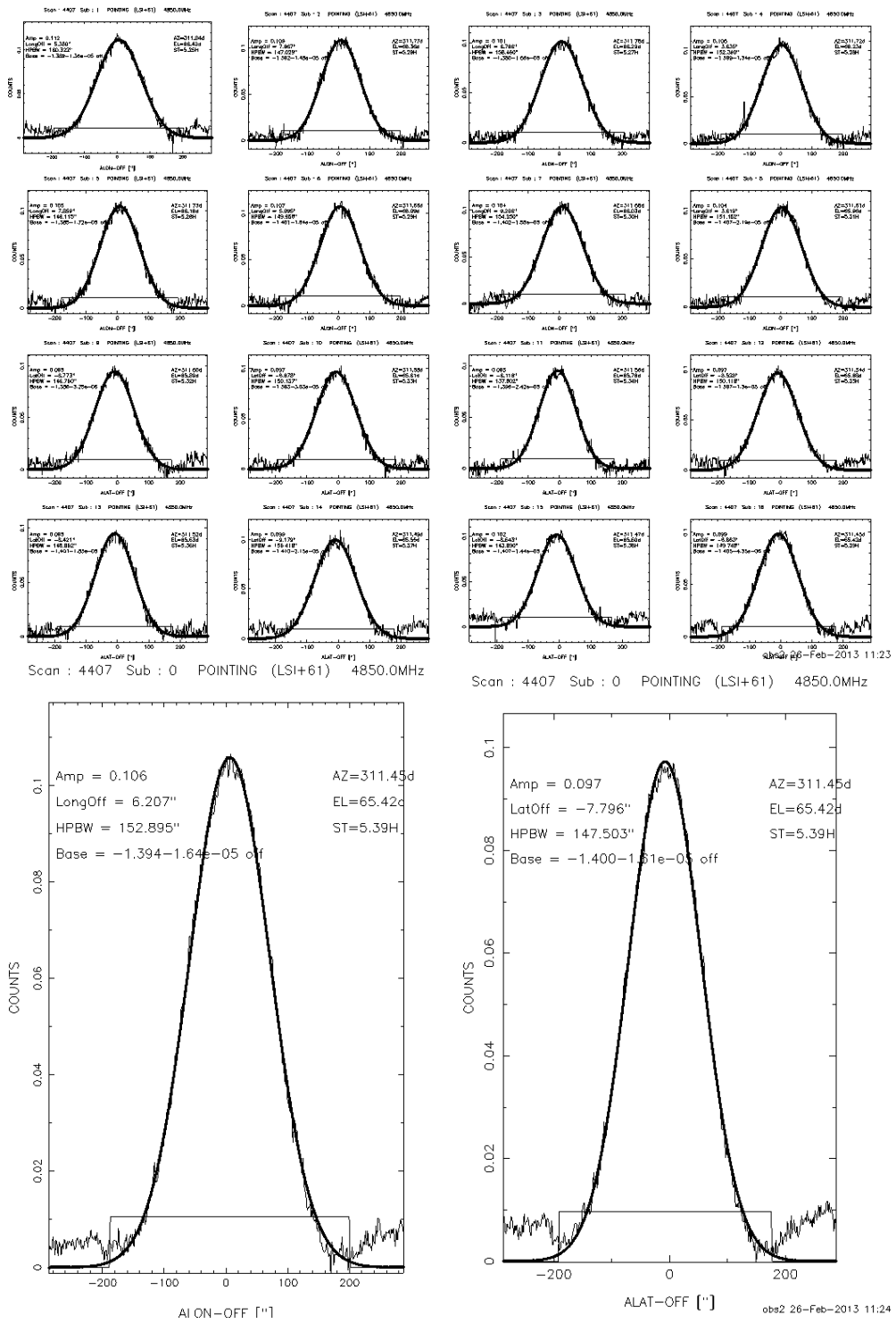

Figure 4.3: Scans at 6 cm wavelength from Epoch 9 (MJD 56016.69). Top: All subscans in elevation and azimuth. Bottom: Average over each direction

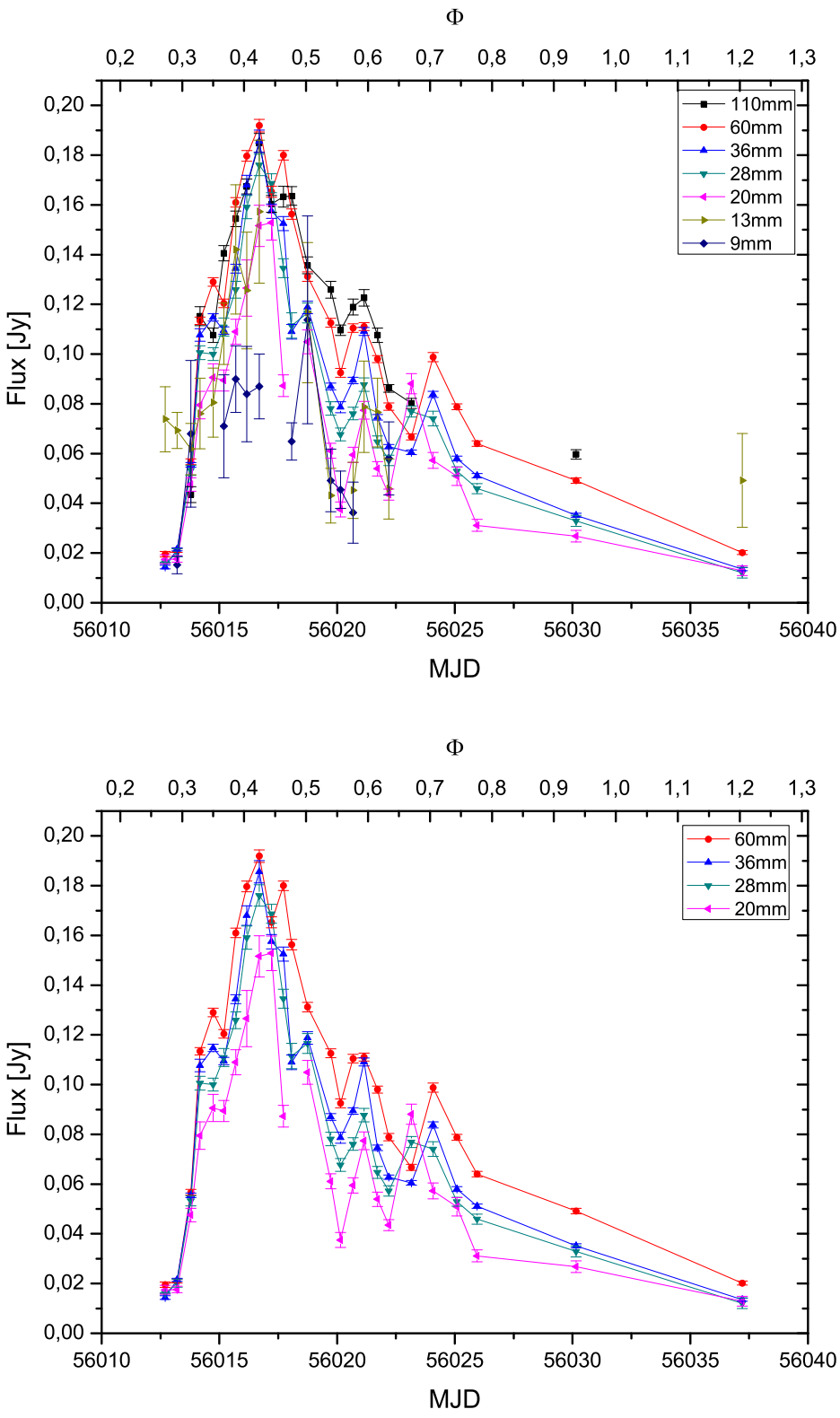

Figure 4.4: Top: Radio light curve (Flux density in Jy plotted against MJD and Φ taken with the Effelsberg 100m telescope at 11, 6, 3.6, 2.8, 2, 1.3 and 0.9 cm.Bottom: Radio light curve (Flux density in Jy plotted against MJD and Φ taken with the Effelsberg 100m telescope at 6, 3.6, 2.8 and 2 cm.

maximum α=-0.651. The shape of the spectra shows that overall the spectrum is steep after 6 cm. Strickman et al. (1998) measured the flux density at 90, 20 and 6 cm wavelength (see their Fig. 5). Massi & Kaufman Bernado (2009) show that the spectrum becomes already flat for spectral indices measured between 13 and 3.6 cm, putting the break in this range. In our case, the spectrum shows flattish characteristics between 11 and 6 cm (2.6 and 4.85 GHz). Nevertheless, the flux at 11 cm is likely to be underestimated, which would put the flat end of the spectrum above 11 cm and not below. In our observations the spectrum is also flattish between 6 and 2 cm during the rise of the flare. This rise is not sampled in Massi & Kaufman Bernado (2009) and only sparsely by Strickman et al. (1998). It needs to be discussed then what a flattish spectrum up to wavelengths around 2 cm during the rise of the flare could imply (see next section).

The spectra in Fig. 4.5, 4.6 and 4.7 do not always seem to be fitted well with just one spectrum. Therefore, the fitting was done as well for frequency selections: i) over the four main frequencies (14.6, 10.5, 8.4, 4.85 GHz; 2, 2.8, 3.6, 6 cm) and ii) over three frequency selections: low (2.6, 4.85, 8.4, 10.5 GHz; 11, 6, 3.6, 2.8 cm), middle (8.4, 10.5, 14.6 GHz; 3.6, 2.8, 2.0 cm) and high (10.5, 14.6, 23, 32 GHz; 2.8, 2.0, 1.3, 0.9 cm). The spectral index for the fit of the four main frequencies is given in Fig.4.8-Bottom. The spectral indices for the low, middle and high frequency selection are given in Fig. 4.9. Because not all frequencies were observed during each epoch, only two frequencies were available for some spectra. In these cases, the errors were calculated using the gaussian error propagation used in Chapter 3. Fig. 4.10 again show the spectral indices for all the frequency selections separately for a better comparison.

The spectral indices show a similar evolution. In the beginning of the flare, the spectrum is almost flat (α ~0 to -0.1), the variations are almost completely within the error bars. The small plateau, which is reached after the first four epochs, is optically thin in the four frequency selection. After the outburst, the spectral index becomes optically thin with an average α ~ -0.4 to -0.5, but superimposed are the three subflares during the decay, which are all accompanied by a rise in the spectral index again (up to α ~0 to -0.1). The last of these three subflares appears to be special in this sense. Here, an inversion takes place at the higher frequencies (10.5 and 14.6 GHz), where $\alpha \geq 0$, while the lower frequencies still yield an optically thin index. In the data from the Fermi-LAT instrument, a steep rise is observed during this same epoch (see next section for a deeper discussion). After this last discernible subflare the spectral index drops to α ~-0.5 to -0.6.

4.3.3 Spectral variability and flare analysis

For a better comparison, Fig. 4.11 shows the rise and decay of the outburst in flux and spectral index separately. The last epoch of the rise and the first epoch of the decay are the same one, Epoch 10 (MJD, 56017.21,Φ=0.45). The first two and the last epoch represent the quiescent state with overall fluxes below 20 mJy (apart from 23 GHz (1.3 cm), see data reduction). The spectrum of the first two epochs is quite flat. Then in Epoch 3 (MJD 56013.79) the flux rises steeply to around 60 mJy with an even flatter spectrum. This is followed by another increase in flux of around 30-50 mJy, with the rise being less at the higher frequencies, which leads to a steep spectrum. Epoch 4 (MJD 56014.17) yields a small peak or plateau, the flux remaining

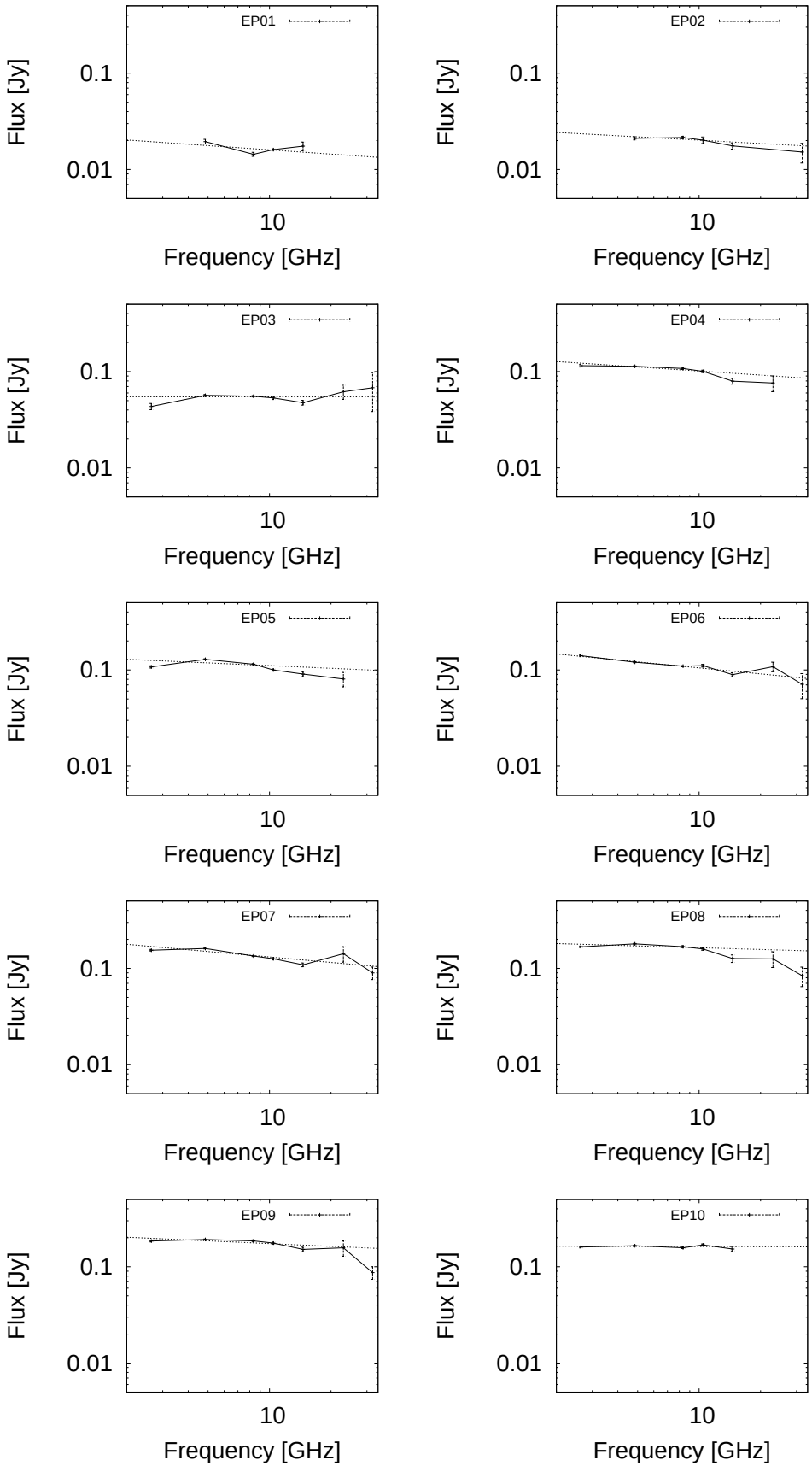

Figure 4.5: Effelsberg radio continuum spectra for Epoch 1-10 in Table 4.1.

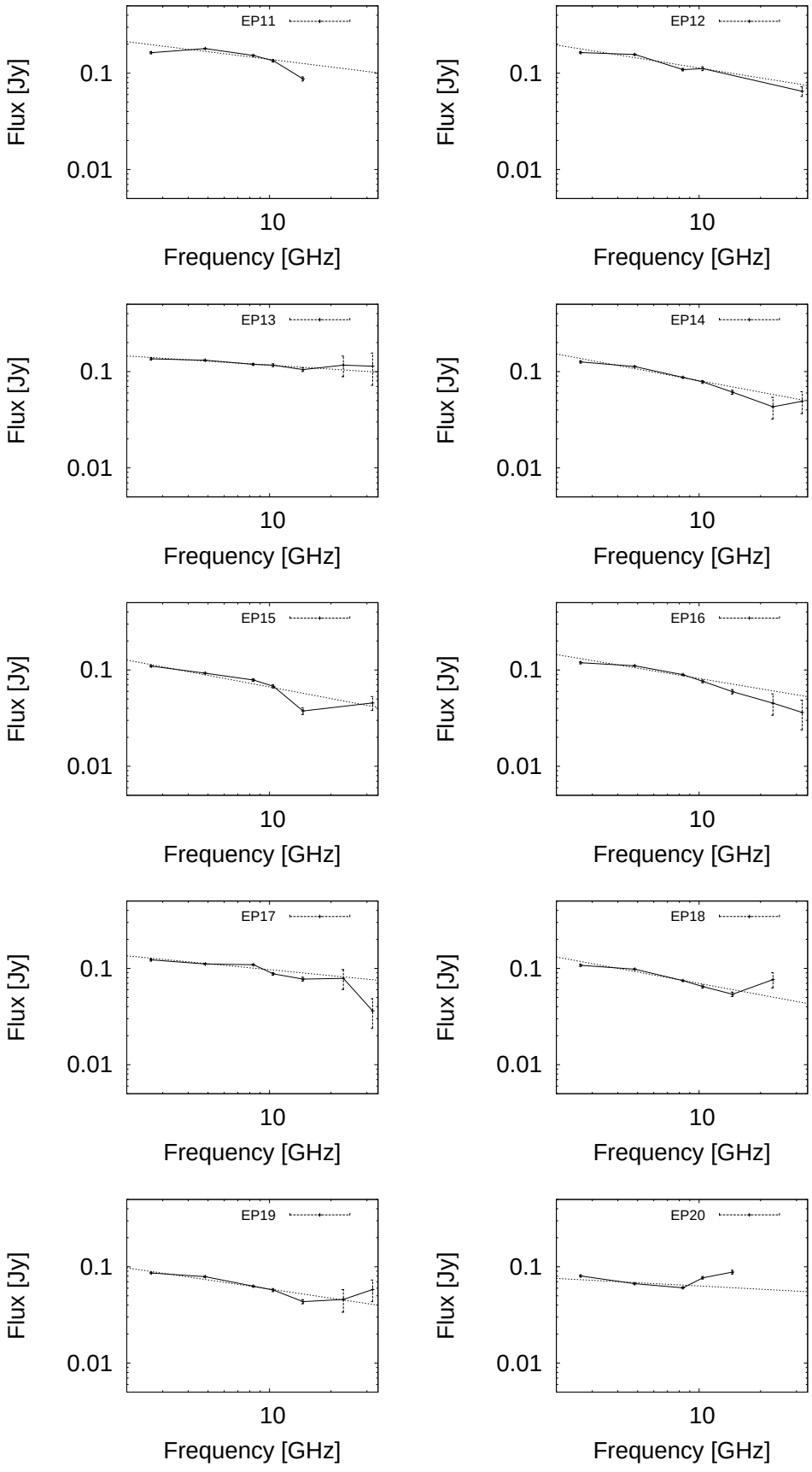

Figure 4.6: Effelsberg radio continuum spectra for Epoch 11-20 in Table 4.1.

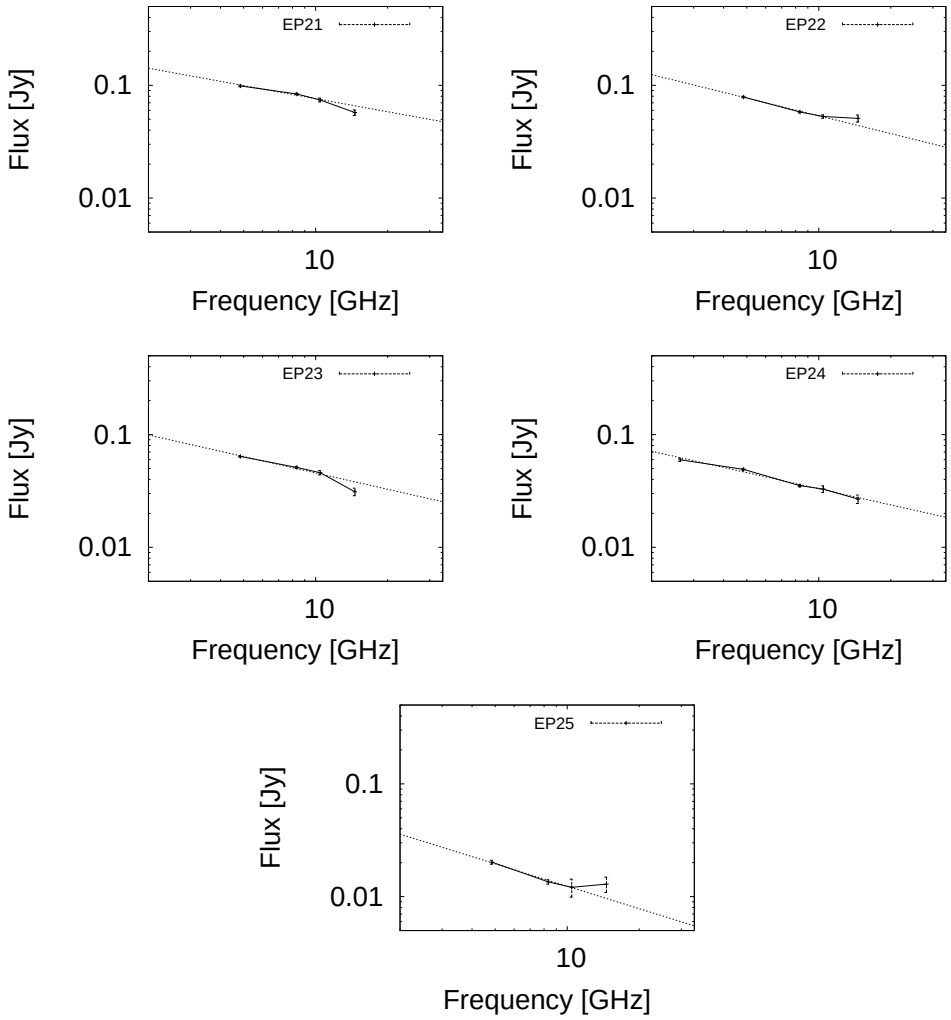

Figure 4.7: Effelsberg radio continuum spectra for Epoch 21-25 in Table 4.1.

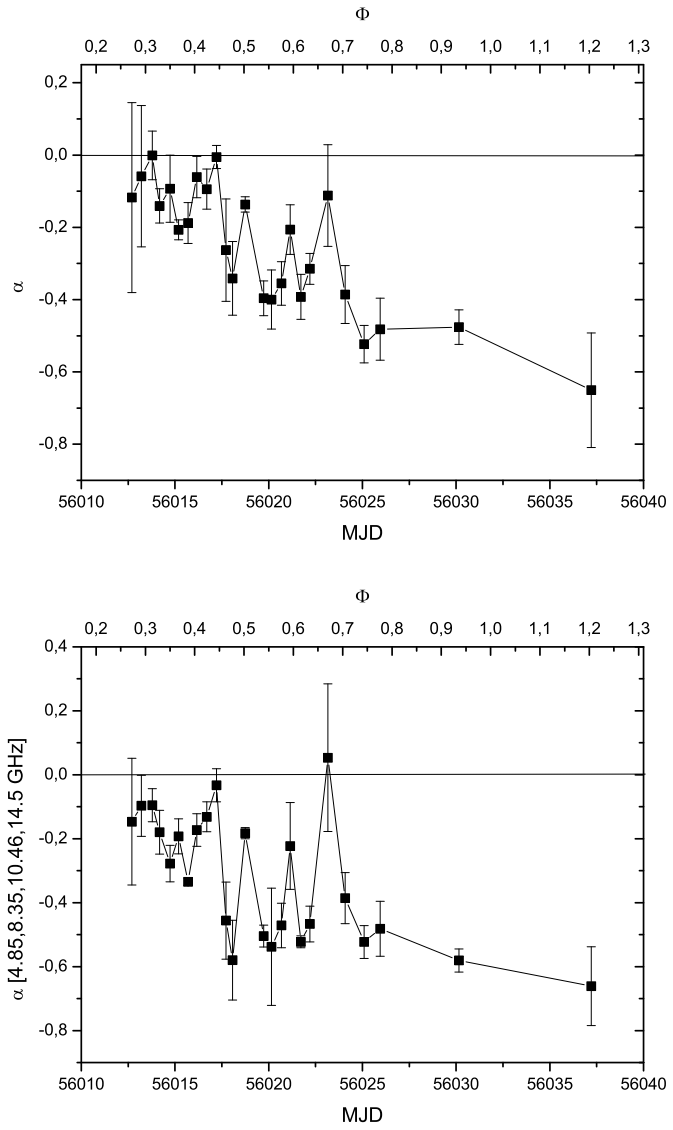

Figure 4.8: Top: Spectral index fitted over all frequencies against MJD and orbital phase Φ. Bottom: The same as above, but for the four main frequencies.

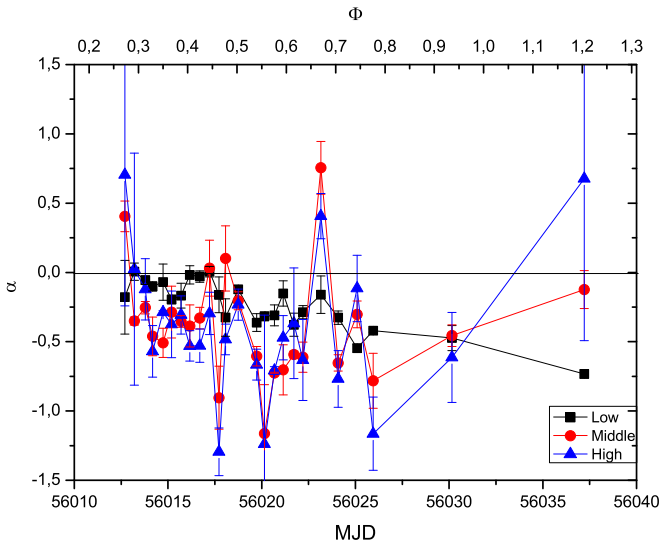

Figure 4.9: Spectral index evolution for high, middle and low against MJD and Φ.

around this level for 24 hours, before rising again. The decay of the small peak or small plateau is characterized by a steep spectrum. The following rise though shows an ever increasing spectrum, the flattest value being reached nevertheless shortly one epoch after the peak of the lightcurve. This suggests that the real flux peak happens between these two epochs.

To get a closer look at the possible nature of the flares, the flare amplitude (ΔS) is depicted against frequency for the pre-flare (Epoch 4, MJD 56014.17) and the main flare in Fig. 4.12 and for the three subflares (Epoch 13, 17, 20 (MJD 56018.74, 56021.14 and 56023.15)) in Fig. 4.14. ΔS was derived by subtracting from the highest peak value the minimum value. For the pre- and the main flare this underestimates ΔS for 2.6, 23 and 32 GHz (11, 1.3 and 0.9 cm), because the measurements for the minimum started 1-2 epochs after the other frequencies. Their values must therefore be seen as lower limits, while the respective upper limits are in principle given by their peak fluxes (for the main flare: 2.6 GHz: 184 mJy, 23 GHz: 157.3 mJy, 32 GHz: 87 mJy). The pre-flare remains a plateau at 23 and 32 GHz. For the main flare, at 23 and 32 GHz the epochs following the main peak are missing though, due to bad data. Therefore, the values at 23 and 32 GHz must not strictly be seen as upper limits, they might have reached even higher values in the missing epochs. All other frequencies peak in Epoch 9 (MJD 56016.68), apart from 10.5 GHz (2 cm), which peaks in Epoch 10 (MJD 56017.21), but lies within the error bars of Epoch 9.

The overall shape of ΔS is comparable for the pre- and the main flare. For the main flare, the spectrum is flat. Taking into account the uncertainties at 2.6, 23 and 32 GHz, a fit of only the four main frequencies was obtained, giving a spectral index of $\alpha \sim 0$ (shown in Fig. F5.11. This sets the main flare apart from the three subflares during the decay of the main flare. The first subflare is only seen at 8.4, 10.5 and 14.6 GHz (3.6, 2.8 and 2 cm). The second subflare shows a

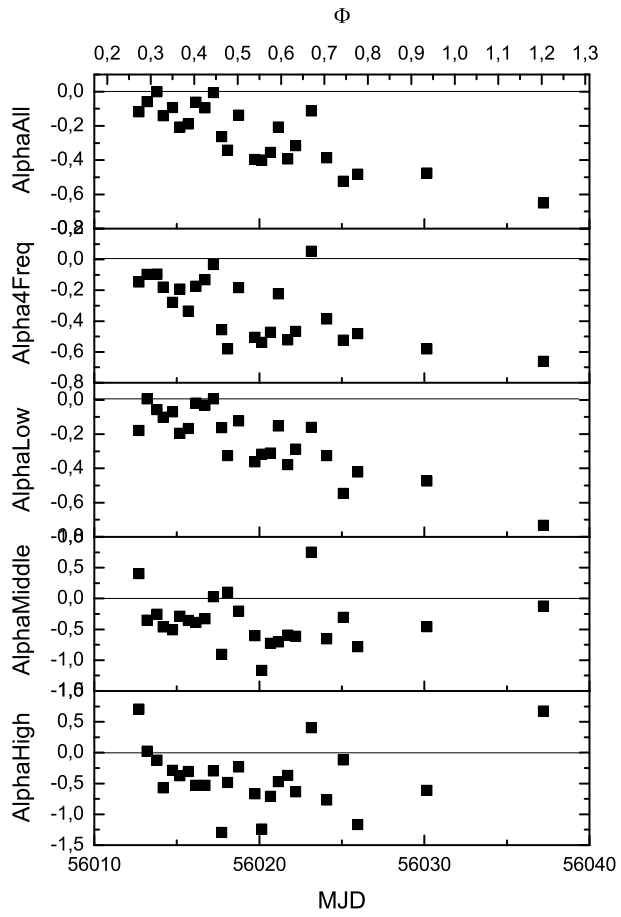

Figure 4.10: From bottom to top: spectral index evolution for high, middle, low, 4 frequencies and all frequencies plotted against MJD and Φ.

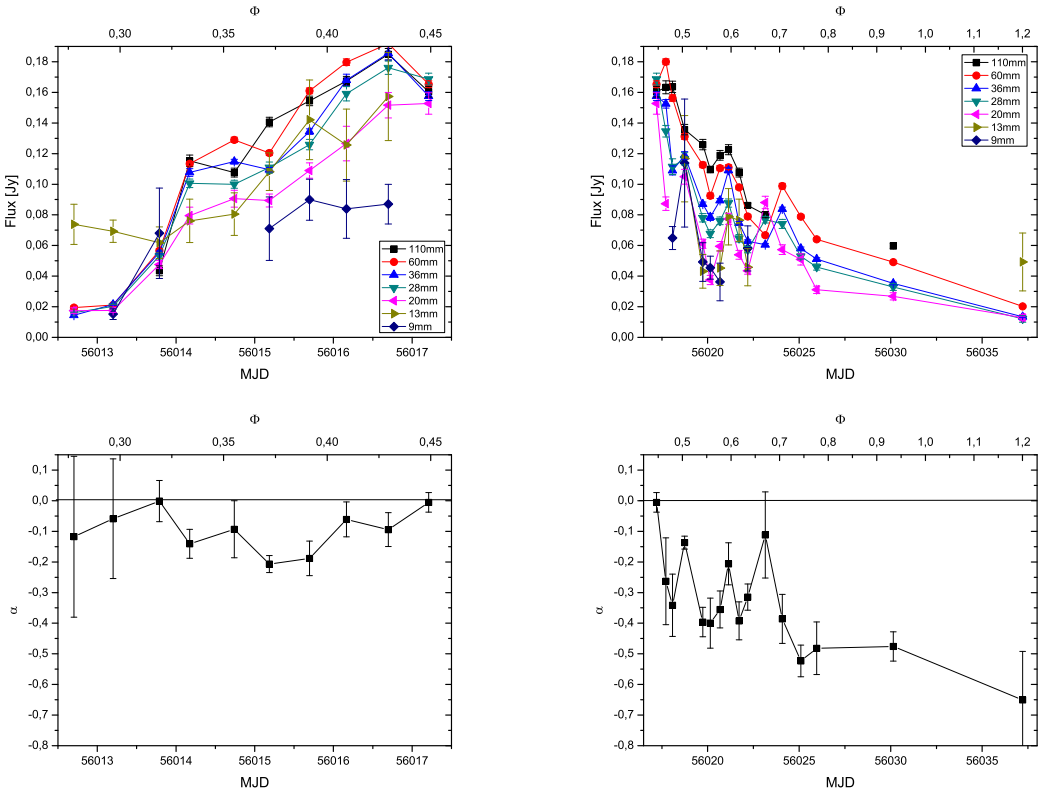

Figure 4.11: Left-Top: Radio light curve (Flux in Jy plotted against MJD and Φ) taken with the Effelsberg 100m telescope at 11, 6, 3.6, 2.8 and 2cm, 13 and 0.9 cm wavelength for the first ten epochs of Table 4.1. Left-Bottom: Spectral index fitted over all frequencies for the first ten epochs. Right: Radio light curve (Flux in Jy plotted against MJD and orbital Phase Φ) taken with the Effelsberg 100m telescope at 6, 3.6, 2.8 and 2cm wavelength.

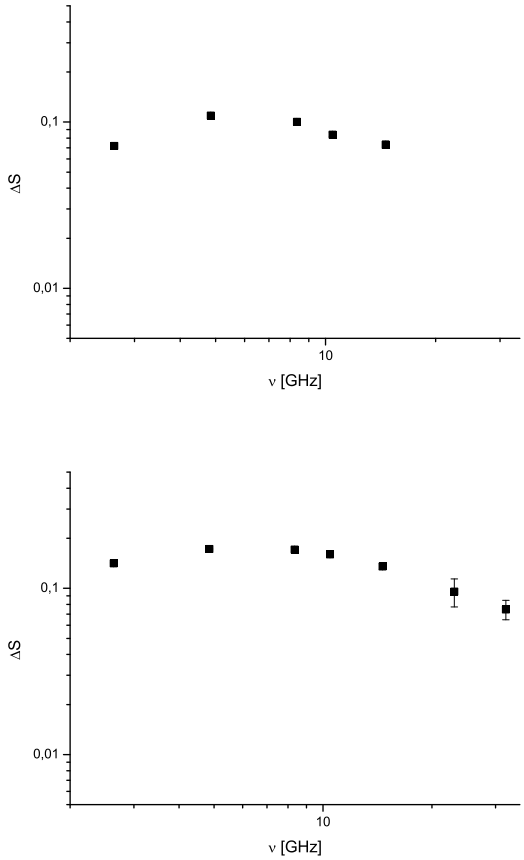

Figure 4.12: Top: Flux amplitude ΔS for the pre-flare. Bottom: Flux amplitude ΔS for the main radio flare.

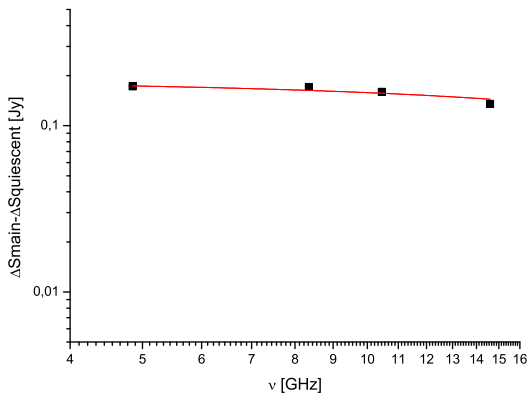

Figure 4.13: Fit of the flare seen at the four main frequncies. The spectral index is ~0.

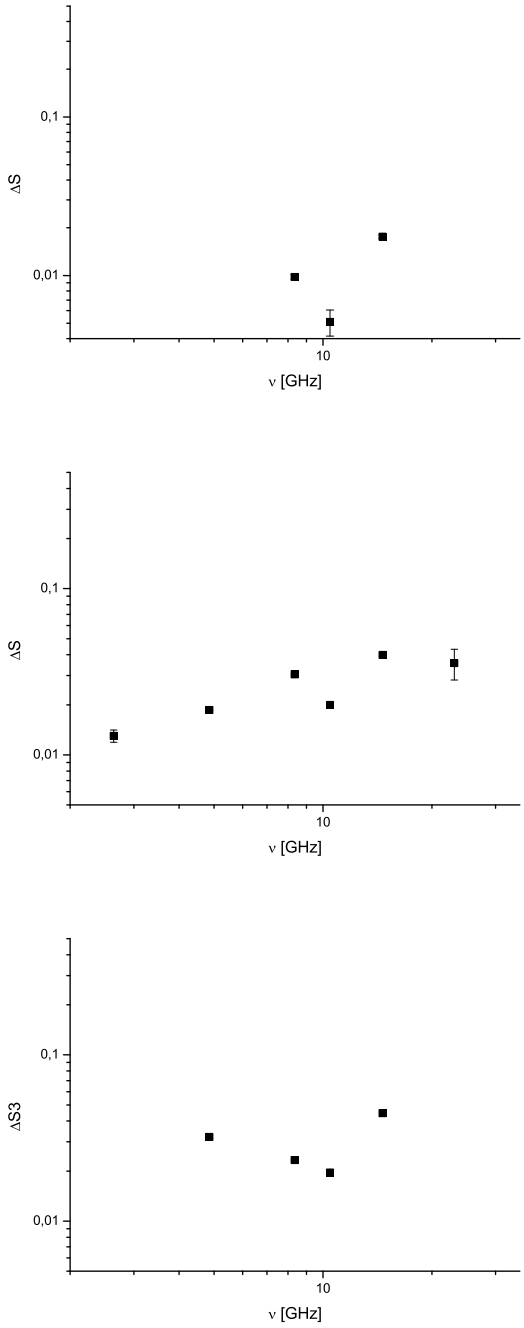

Figure 4.14: Top: Flux amplitude ΔS for the first subflare. Middle: Flux amplitude ΔS for the second subflare. Bottom: Flux amplitude ΔS for the third subflare.

completely different trend with ΔS declining strongly from higher to lower frequencies, yielding an inverted spectrum, only at 10.5 GHz (2cm) the value lies below the trend. The third subflare shows ΔS declining from lower to higher frequencies, but with the highest frequency showing the strongest amplitude. This looks again similar to the first subflare. At this point, though, also the time delays between the peaks at different frequencies must be looked at. The pre-flare peaks first at 11 cm, one epoch before the other frequencies. For the main flare the time delays are all zero, only the 10.5 GHz (2.cm) peak could have a delay of one epoch, as already noted above. The first and second subflare show zero time delays. The third subflare though has a time delay of one day at 4.85 and 8.4 GHz with respect to the peaks at 14.6 and 10.5 GHz (after Epoch 20, MJD 56023.15, measurements were only taken once a day).

4.4 Comparison with Fermi data

The flux measurements of LS I +61°303 from the Fermi-LAT during the Effelsberg observations are given in Fig. 4.15. The data are given in 24 hour bins. Although the data is of course not taken strictly simultaneously and is not as resolved (24 h bins against measurements every 12 h with Effelsberg), its evolution can still be compared with the radio data from Effelsberg to investigate a relation between high energy and radio emission in LS I +61°303.

At the beginning of the Effelsberg observations, the counts measured by Fermi-Lat start to decrease first then exhibit a small rise and then fall continuously as the radio flux density rises. For the first subflare, a small rise preceeds the radio flux density and lies still within errorbars (around MJD 56018 and MJD 56020). The third subflare takes a special role, the gamma-ray flux rise lying clearly outside the errors. It is only in one point, which means that the rise and decay have taken place within 24 hours, which is the binning time of the Fermi-Lat observations. Unfortunately, a better time resolution cannot be obtained. The Fermi point overlaps with Epoch 20 of the Effelsberg observations. The integration time of the Fermi point (MJD 56023-56024) is longer than Epoch 20 (start MJD 56023,152, duration 2-3 hours) though, so one cannot infer the order of appearance of the flares in gamma and in radio, but this subflare clearly distinguished from the other outbursts. This is a strong argument for a dense monitoring at gamma and radio to shed light upon such events.

4.5 Comparison with GBI data

As explained in the beginning, monitoring a source such as LS I +61°303 with a single-dish like Effelsberg bears the possible problem, that due to the low resolution a lot of extended emission is sampled as well. For LS I +61°303, this is a particular problem, as it lies close to a large HII region. It is therefore neccessary to compare the fluxes measured with Effelsberg with fluxes measured with an interferometer like GBI. Even though these observations are of course not

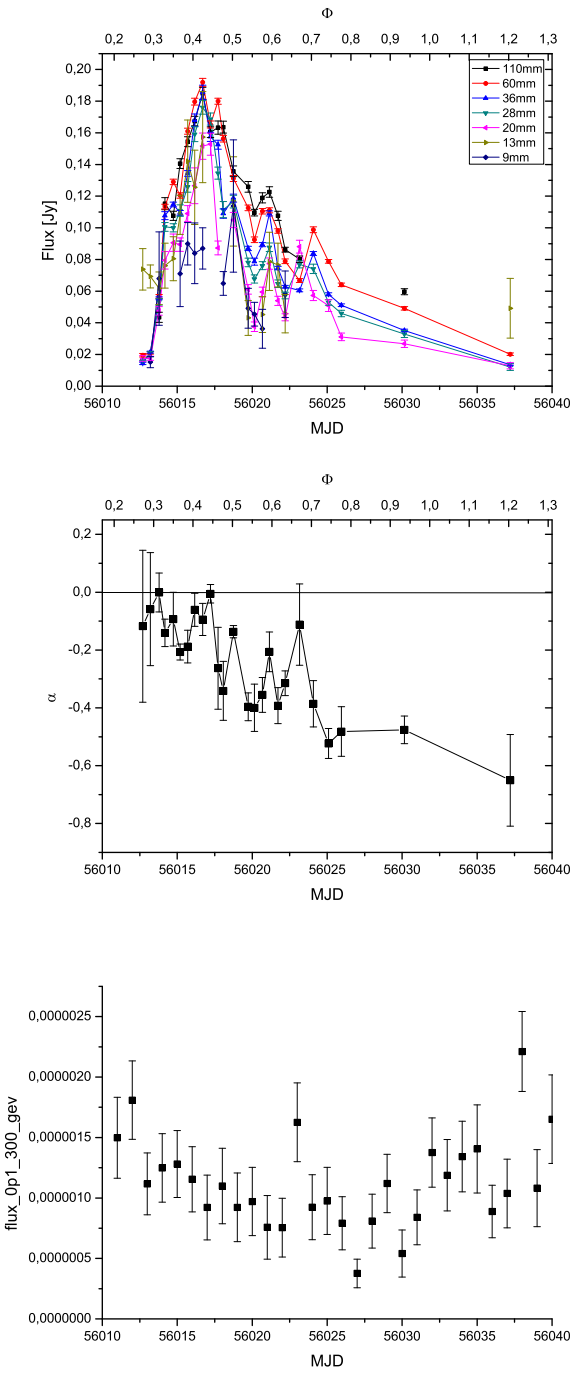

Figure 4.15: Top: Flux for the Effelsberg observations of LS I +61°303 against MJD and Φ. Middle: Spectral index for the Effelsberg observations of LS I +61°303 against MJD and Φ. Bottom: Fermi Flux (0-300GeV) of LS I +61°303 against MJD.

simultaneous, due to the periodicities in LS I +61°303, the overall flux density level during the respective superorbital period should be indicative. In Fig. 4.16 the GBI light curves at 2.2 and 8.3 GHz are given for different epochs with superorbital period around 0.5 and 0.6. The flux density levels are comparable and there seems to be no underestimation of the flux density measured with the Effelsberg 100m telescope. Nevertheless, at 11 cm the large beam from the telescope samples additional emission, which is seen in flux profiles as an asymmetric baseline.

4.6 Results

The main results from the flux density and spectral analysis are then: 1) a main flare is detected and several subflares, one during the onset and three during the decay, 2) the flare spectrum is flat (α ~0) and its rise mostly achromatic, 3) during the decay, the spectrum becomes optically thinner and 4) the subflares during the decay are accompanied with a rise in the spectral index.

The observations are comparable to flux density measurements from the GBI for the same interval of the superorbital period. A comparison with high energy data from the Fermi-LAT, a decay of the flux during the outburst is seen and a high point possibly connected to one of the subflares. After the radio outburst, the high energy flux rises again. All these facts will be taken into account for the two main scenarios proposed for LS I +61°303.

4.7 In the microquasar context

In the context of the two-peak accretion microquasar model with a precessing jet (precession period P2=26.9 days), as proposed for LS I +61°303 from former analysis (Massi, Ros & Zimmermann 2012), the flux density and spectral evolution should show both accretion and precession components. Several processes are then involved:

- Variable Doppler boosting of a weak steady precessing jet always present (radio and gamma-ray emission is observed all around the orbit) (i.e., variations only depending on Doppler boosting or P2).
- Intrinsic variation of flux density due to increased ejection at a specific phase of the orbital period (P1) (following the two peak model).
- This can be followed by a shock.

These variations depend on P1 and P2.

The spectral index characteristics from accretion would be expected as the typical change from optically thick emission to an optically thin outburst during an accretion event (Fender et al

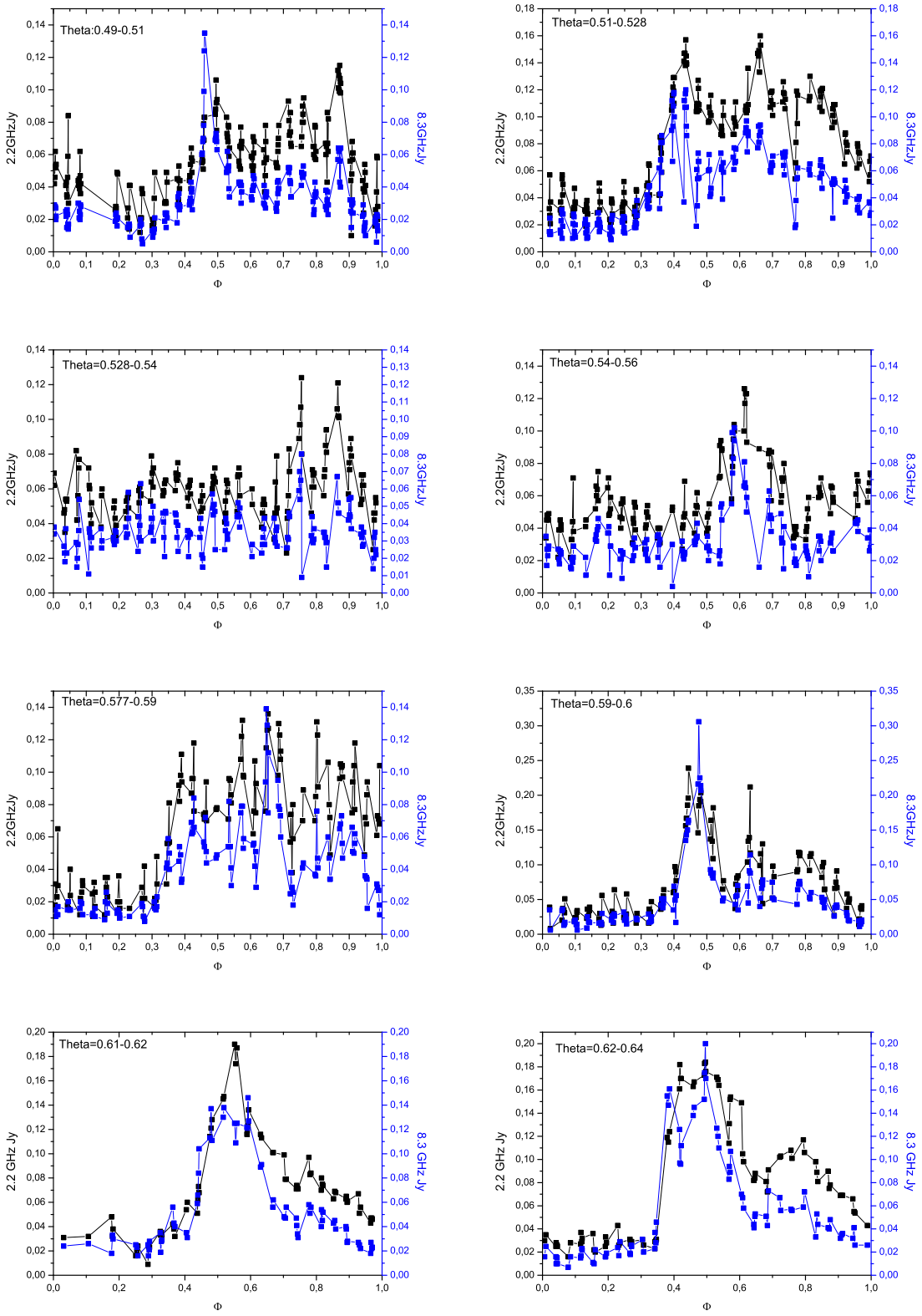

Figure 4.16: GBI orbital lightcurves of LS I +61°303 at 2.2 (black) and 8.3 GHz (blue) for different Θ intervals. The Effelsberg observations were done in the interval 0.59-0.6. During/around this Θ interval, the GBI data (though not contemporary) show the onset of the flare around Φ=0.3-0.4, the same as in the Effelsbeg data.

2004, Massi & Kaufman Bernado 2009). For precession, the flux should undergo Doppler boosting (Massi & Jaron 2013), which should be strongest when the jet passes closest to our line of sight. The rise in flux should be accromatic following $S \propto \nu^3$ (Marscher 2009). Inspecting again the flux evolution, it starts around $\Phi \sim 0.3$ and shows a sharp rise (within 3 days) and a long decay, which lasts until the end of the period. The rise and decay are not smooth, but show multiple subflares, one during the onset (Epoch 5, MJD 56014.74)) and three during the decay (Epoch 13, 17 and 20, MJD 56018.74, 56021.14 and 56023.15). During the quiescent phase in the beginning, the spectrum is flat within the errorbars, consistent with a steady jet, as proposed for LS I +61°303 by Massi & Zimmermann (2010). During the onset of the flare the spectrum remains flat, but the first sub-flare, in Epoch 5, is optically thinner. The following rise towards the main flare becomes again ever flatter reaching the highest spectral index though shortly after the main flux peak. This could be an indicator, that the real flux density peak lies between the two epochs, Epoch 9 and 10, with the spectral index peaking there as well. When subtracting the quiescent spectrum from the main flare spectrum, the spectral index is zero. The decay is then characterized by an ever steeper spectrum, only interrupted by three rises in the index, which correspond to the three subflares.

Occurence of the peak

From the two-peak model with Compton losses around periastron, the occurence of the accretion/ejection peak is expected towards apastron (Marti & Paredes 1995, Bosch-Ramon et al. 2006, Romero et al 2007, Massi & Bernado 2009). Massi & Jaron (2013) show that the accretion process and precession are only synchronized in the maximum of the 4.6 years period, around Θ=0.9. Synchronized means an increase of the periodical (P1) ejection of relativistic electrons in the steady jet, when the jet is at the most favourable angle with respect to the line of sight, i.e., maximum Doppler boosting. Therefore an offset between the two effects is expected for all other superorbital phase. The Effelsberg observations were done during Θ=0.6 so closer to the minimum, Θ=0.4-0.5, where the ejection occurs at the most unfavourable angle with respect to the line of sight (i.e., minimum Doppler boosting).

From the onset alone, a distinction between amplification of the flux due to Doppler boosting and amplification due to an intrinsic mechanism is not possible, a comparison of the light curve with light curves from the GBI at 2.2 and 8.3 GHz for the same superorbital phases shows that the onset is compatible (see Fig. 4.16) and looking at the surrounding phases it is quite stable. For most of the light curves, the peak rise begins around Φ=0.3 as in our observations, only at Θ=0.52 and 0.56, the main rise is later. The overall flux around Φ=0.3 is for these two Θ phases higher than during the other orbits. This could be an indicator for this flux coming from the precession alone and could yield an upper limit for the flux from precession induced Doppler boosting of around 40 to 60 mJy. Interestingly, this is the same value reached by the first rise of the flare in the Effelsberg observations. Nevertheless, there is no distinctable flare shape for these flux values in the GBI data.

Flare profile

An outburst is mostly characterized by a rapid onset and an adiabatic decay (Fender et al 2004). The precession peak should be symmetric, as it is created only by a geometrical effect. To possibly disentangle the processes, the strength of the Doppler boosting needs to be discussed. With a mixing of processes, it is well possible, that it is visible during the onset and then gets overshone by the accretion event, or the other way around. As a first-order estimate of the precession part of the flux, we can look at the GBI lightcurves from corresponding Θ phases. The precession part should be a quite stable part of the lightcurve, because it is almost purely geometrically induced depending on the viewing angle of the jet, but also on its velocity and spectral index. Furthermore, the offset between accretion and precession peak should follow a smooth modulation of the orbital occurrence. If the onset of the outburst varies too strongly, then precession cannot play a big role, because in this case the precessional peak should be observable independently of the accretion peak.

The onset of the flare is therefore compatible both with an accretion/ejection event and precession. The decay looks like adiabatic expansion of an ejection. The subflares are indicative of transient events i.e. shocks and not precession (Marscher 2009, Tuerler 2011). Precession is then likely a smaller part of the flux. Subtracting a Doppler boosting profile could yield some insight.

Flare spectra

The flare rise is achromatic within the errorbars, which suggests precession, although an optically thick outburst/optically thick emission is expected for accretion/ejection (before the transient event) as well. The average spectral index is higher for the rise than for the decay (compare Bottom-Left and -Right in Fig. 4.11). The clear difference in the steepness of the spectrum for rise and decay makes an argument against precession being responsible for both rise and decay. The subflares during the decay, associated with rises in the spectral index, can only come from transient events, e.g. shocks. The timescales are so short and the change in spectral index so strong, that precession cannot be responsible. Small accretion events can not be excluded, because of the lack of measurements on timescales shorter than 12 hours.

Summing up, the spectrum shows a flat outburst followed by muliple small optically thin outbursts. The sequence seen in the GBI, the RATAN600 and the VLBA data, where an optically thick is followed by an optically thin outburst with an amplitude higher than the optically thick one (so not attributable to adiabatic expansion), is not observed. All these observations use 13 cm wavelength as well, and the optically thin outburst is only observed at this wavelength. Our longest wavelength is 11 cm, and due to the extended emission detected at this wavelength with Effelsberg, the flux values can only be seen as lower limits.

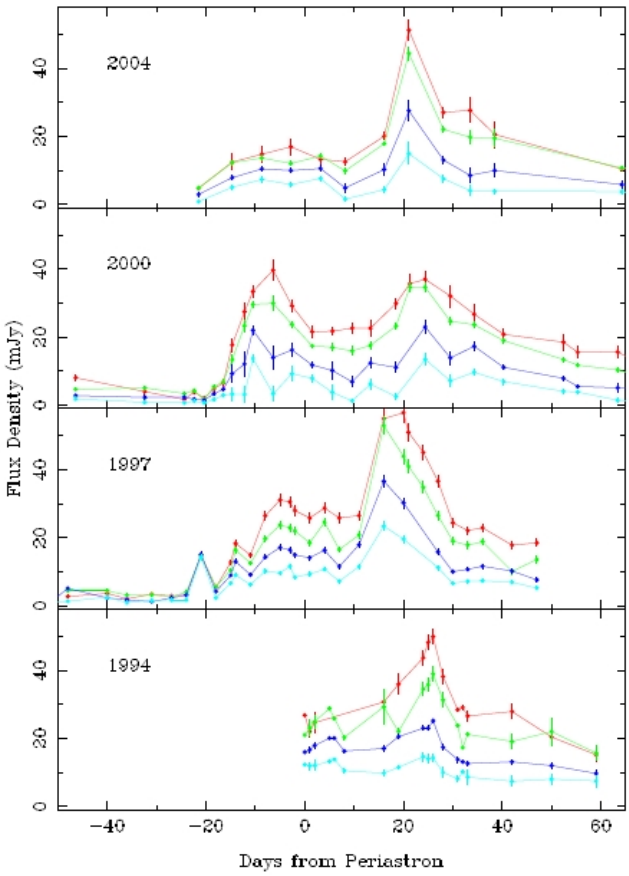

Figure 4.17: Lightcurves of periastron passages of PSR 1259-63 (Abdo et al 2011).

4.8 In the millisecond pulsar context

There are several variaties of the colliding wind scenario for LS I +61°303, none of them though, are yet conform with or addressing the radio spectral index evolution as shown by Massi & Kaufman Bernado (2009) (see Zdziarski et al. 2010, Chernyakova et al. 2006, Dubus 2006, Bosch-Ramon et al. 2012). A first step should therefore be the direct comparison with the only source known to be a colliding wind binary, PSR 1259-63. With its well defined period of 3.4 years, its periastron passages have been well monitored in radio since 1994, some of these lightcurves are shown in Fig. 4.17 (Connors et al 2002, Johnston et al 2005, Abdo et al 2011). All of the radio light curves are compatible with the pulsar crossing the disk of the Be star around periastron. This creates one strong peak after periastron and sometimes a small peak before periastron (of differing magnitude from period to period as seen in Fig. 4.17, explained by changes in the wind density). If both are observed, they are arranged symmetrically around periastron (Johnston et al. 2005). This event is accompanied by the disappearance of the radio pulses (~16 days before to 15 days after periastron, see Johnston et al 2005), which are probably lost due to free-free absorption (Connors et al. 2002, Johnston et al. 2005). The spectral index of these two peaks is

always optically thin (Connors et al. 2002, Johnston et al. 2005). When the pulsar crosses the disk, the colliding winds accelerate continuously particles to relativistic energies, which then escape along the magnetic field lines and produce optically thin synchrotron emission. The shock area expands later on and produces an adiabatic decay of the emission.

When comparing LS I +61°303 with PSR B1259-63, one has to keep in mind though that LS I +61°303 is a much smaller system, with its period of only 26.5 days. The compact object therefore travels within the wind of its companion during the entire orbit. This means that particles are accelerated continuously all the time, with the spectral index being optically thin all the time, which does not seem to be the case in LS I +61°303. The continuously expected radio emission along the orbit is actually compatible with the observed radio emission in LS I +61°303, the changes in the spectral index and the recurring outbursts towards apastron though, are not yet explained. As in the microquasar model, the orbital motion of the compact object should have an effect on the stellar wind structure (Romero et al 2007, Zabalza et al. 2011b). Zabalza et al. (2011b) connect the orbit to orbit instabilities in VHE and X-rays to wind instabilities that can cause the shock regions to appear and disappear.

In direct comparison with PSR B1259-63, LS I +61°303 shows only one radio outburst every orbital revolution, and it is always seen towards apastron, and never at periastron. A second peak before periastron is also never seen. Now, emission around periastron could be upscattered to higher energies with the same argumentation as for the missing periastron peak in the microquasar model. But why does the second peak survive? It could survive, because is it seen so far from periastron, but why does it occur so far from periastron? Taking into account the smaller orbit, the compact object in LS I +61°303 will not really cross the stellar disk as in PSR B1259-63, but only move into a higher density of the stellar companion towards periastron. But then why should a shock with such a pronounced outburst occur only after (and so far from) periastron? The same argumentation as for PSR B1259-63 holds in this case. Concerning the subflares seen in the light curve of LS I +61°303, multiple shocks could explain those, but are so far not modelled in detail.

Taking into account also gamma-rays, PSR B1259-63 was detected with Fermi-LAT after its periastron passage 2010 (no corresponding peak in X-rays or radio), but the gamma-rays flared after the radio and X-rays. Summing up, a comparison around periastron yields symmetrically around periastron radio and X-ray flux in PSR B1259-63, and after the radio and X-ray flares a gamma-ray flare is seen. The TeV light curve of PSR B1259-63 measured with HESS (High Energy Stereoscopic System) shows a peak before and around 20 days after periastron (Aharonian et al. 2005, 2009). In contrast, no discernible radio and X-ray flux is seen in LS I +61°303, but, depending on some long-term period, a gamma-ray peak in GeV or at least strong gamma-ray emission is always seen around periastron. The TeV curve peaks towards apastron, and LS I +61°303 was only once detected in TeV around periastron during the minimum Θ phase (Acciari et al 2011a). Strong gamma-rays in the GeV range are then never seen together with X-rays and radio peaks, but only in the TeV range.

4.9 Comparison with other sources

Besides PSR B1259-63 , not many other X-ray binaries are known to emit in gamma-rays as well. LS5039 is a high mass X-ray binary with an orbital period of 3.9 days. It exhibits radio, high and very high energy emission, modulated by the orbital period. Morphologically, it has been resolved into one and two-sided structures (Moldon 2012). Other gamma-ray binaries candidates are HESS J0632+057, AGL J2241+4454. In Fig. 4.18, radio light curves (or detections) at 1.6 GHz are compared for the three confirmed gamma-ray binaries, emitting in GeV as well as TeV: LS I +61°303, LS5039 and PSR B1259-63 and a gamma-ray binary candidate HESS J0632+057 (Moldon 2012). Moldon (2012) derived these light curves by averaging over different data bases. This explains the broad peak for LS I +61°303, because flares from different superorbital periods get mixed. For LS5039 hardly any modulation is visible. This is because in comparison to the other sources the modulation is rather weak (< 30%) (Moldon 2012).

Looking at these lightcurves it is obvious that all three main sources behave quite differently. The gamma-ray binary candidate HESS J0632+057 yields too small a data base to make any substantial comparison. LS I +61°303 and PSR B1259-63 exhibit the differences as explained in the previous section. LS 5039 changes its flux on a much smaller amplitude scale. A microquasar model has been proposed for LS 5039 as well, it shows changes from one to two-sided structures and no pulses are observed. As in LS I +61°303, this is attributed to free free absorption, its orbit is even smaller (3.9 days) then in LS I +61°303. The numerous details in the systems that can have an effect on the light curves as well as the spectral index in both main models must in any case lead to huge differences, when the measurements are compared. Therefore, each source needs to be modelled with both models.

There remains an X-ray binary, which has not yet been detected in gamma-rays, but exhibits in radio a very similar behaviour as LS I +61°303: Circinus X-1. It is a low or high mass X-ray binary (Jonker 2006) with a pronounced radio peak at periastron (Tudose et al. 2008, Fender et al. 2012) and a second peak towards apastron has been found during active periods (Tudose et al. 2008). Morphologically, jet structures are resolved (one and two-sided), sometimes bent and with changing position angle (Fender et al. 1998). It is proposed that the two peaks are caused by accretion processes and that the changing morphological structures come from a precessing jet. It remains to be understood, why, if this model applies indeed for LS I +61°303, gamma-rays are so far seen only in LS I +61°303 and not in Circinus X-1. Assuming they are produced as well, then why are they not Doppler boosted enough to be detected? Concerning the absence of EIC of stellar photons in Circinus X-1, it could be that because the companion is of spectral type B2 or even cooler in Circinus X-1, there are not enough UV photons (as for the B0V in LS I +61°303) (see Massi & Kaufman Bernado 2009). The Doppler boosting on the other side depends strongly on the jet velocity and the angle of the jet to the line of sight.

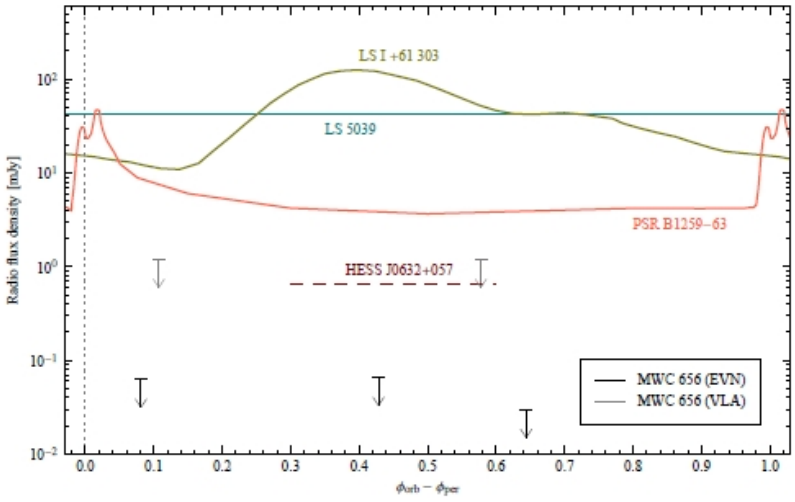

Figure 4.18: Radio lightcurves of gamma-ray binaries at 1.6 GHz (Moldon 2012), the flux is given against the post-periastron orbital phase.

4.10 Conclusions and discussion

During the Effelsberg campaign in March and April 2012, LS I +61°303 was monitored at a minimum of four frequencies every 12 hours covering the complete radio outburst.

The key results from this campaign are then:

- Effelsberg as a large single dish telescope can be used at wavelengths ≤6 cm for observations of a weak and variable source such as LS I +61°303. Owing to the integration time neccessary for one epoch, spectral variabilities of down to 2 hours are detected. From the observations, we have learned that the highest time resolution for LS I +61°303 with Effelsberg should be around half an hour for 4-6 frequencies, depending on the source brightness and weather conditions.

- The results of the spectral analysis confirm former results that in LS I +61°303 the optically thin spectrum starts already at 6 cm. Because of the difficulties at 11 cm, which will be even more severe at lower frequencies, it can not be determined whether the break lies between 13 cm and 11 cm or between 11 cm and 6 cm. But it must lie between 13 cm and 6 cm.

- The main flare has a flat spectrum indicative of a slow conical outflow, i.e., a steady jet.

- Small subflares are detected, reminiscient of shocks, all are accompanied by a rise in the spectral index, especially interestingly is the third subflare during the decay (Epoch 20, MJD 56023.152). It peaks at higher frequencies first and then moves to lower frequencies. This subflare is also accompanied with a rise in gamma-rays, observed by Fermi-LAT.

- Variability of below 12 hours clearly exists, as is seen in the subflares and the discrepancy between the main peak in spectral index and in flux, which points to us missing the real flux and spectral peak between Epoch 9 and 10.
- The comparison of observing results with different models can neiter discard or confirm the interpretation of a microquasar model with a precessing jet or a millisecond pulsar.

Chapter 5

Conclusions and Discussion

Summing up, the main results of this thesis are:

- The high energy and radio spectral index analysis can explain the absence of a high energy cut-off observed in LS I +61°303.

- Massi & Zimmermann (2010) noted already that the correlation coefficient between the X-ray and the VHE flux in LS I +61°303 is the same as known in Blazars. Here, it is shown now that the spectral indices found in LS I +61°303 for correlated X-rays and VHE are also the same as seen in Blazars, i.e., LS I +61°303 could be a microblazar. The X-rays could then be attributed to synchrotron and the VHE emission to synchrotron self-Comptonization (SSC) as in Blazars. Furthermore, X-ray synchrotron emission could be mistaken as emission from the low hard state, because the spectral index is the same. This could also explain the missing black-body component during the transitional state in LS I +61°303, if the synchrotron emission overshines the disk component.

- Re-analysis of high resolution radio observations with the VLBA show double-sided structures in LS I +61°303.

- Astrometry of the peak fluxes shows that the peaks trace a closed structure (an ellipse) with a period of ∼27 days.

- The double-sided structures, the fast switches to one-sided structures, the change in the position angle and the astrometry results can be explained by microblazar model with a precessing jet.

- Radio flux and spectral analysis of the VLBA data reveal again an optically thick peak followed by an optically thin one as expected for a microquasar.

- Component fitting of the radio maps give an estimate of $\beta \cos \Theta < 0.65$ for the maps with double-sided structures.

- The single-dish 100m radio telescope in Effelsberg can be used up to 6 cm for the observations of such a weak source as LS I +61°303. The scan technique allows for the correct determination of a baseline.
- A complete spectrum during a radio flare of LS I +61°303 was fitted for the first time, by removing the quiescent spectrum. The spectrum is flat. This shows that the main flare happens during the steady jet, because the flat part of the spectrum can only arise from a conical structure.
- The break of the flat spectrum lies in the GHz regime for LS I +61°303.
- All subflares following the main outburst show a rise in the spectral index.
- One of these subflares can be associated with a corresponding rise in GeV emission, seen by the Fermi-LAT. The radio spectrum of this subflare is clearly inverted at the higher frequencies.

At the beginning of my PhD in 2010, the evidence surrounding the nature of LS I +61°303 was ambiguous, but Massi & Kaufman Bernado (2009) had revealed the radio spectral index to be a key tool for the understanding of LS I +61°303, yielding strong evidence for a two-peak accretion/ejection microquasar and against a pulsar scenario. In 2010, Massi & Zimmermann made a comparison of the existing observations with the two main scenarios. The comparison used the two-peak microquasar model by Marti & Paredes (1995), Bosch-Ramon et al (2006) and Romero et al (2007) and for the pulsar model the characteristics observed in PSR B1259-63 (Connors et al 2002, Johnston et al 2005). The comparison included the existence of radio pulses, the X-ray luminosity, the orbital occurrence of the large outburst, the radio spectral index characteristics and the orbital occurrence of the gamma-ray peak. The results are shown in Table 1 in Massi & Zimmermann (2010). The conclusion reached was that the microquasar model explains all these features as seen in LS I +61°303, while the pulsar model so far does not explain the spectral characteristics, the radio peak towards apastron and the two peaks seen in gamma-rays.

Still, as a clear lack of the microquasar model were seen the X-ray characteristics of LS I +61°303. Massi & Zimmermann (2010) explain the lack of the black-body component with LS I +61°303 going from a low hard to a transitional (steep power law) and then immediately back to the low hard state. This explains as well the radio emission seen all along the orbit. This switch happens twice in LS I +61°303, because of the two accretion/ejection events predicted by the two-peak microquasar model. Similar behaviour has been observed in other sources. Cygnus X-1, one of the brightest X-ray binaries, remains most of the time in the low hard state and then suddenly goes via the transitional state to the high soft state. Sometimes though, only a switch to the transitional state is observed and the source then goes back to the low hard state. This is called a failed state transition (Pottschmidt et al 2001). Also GRS 1915+105 is known to not always reach the high soft state after moving to the transitional state. In GRS 1915+105 and in Cygnus X-1 though, this happens at much higher (super Eddington) X-ray luminosities than in LS I +61°303. Nevertheless, the X-ray spectral characteristics of the low hard state predict a power law with a spectral

index Γ ~1.7 and a high energy cut-off. Furthermore, the transitional state should show a much softer spectral index and no cut-off. But so far, only a hard spectral index and non-detections of the high energy cut-off were reported (Chernyakova et al 2006, Zhang et al. 2010). In Zimmermann & Massi (2012), it is shown that these observations are nonetheless compatible with the two peak microquasar model. Due to the low luminosity of the X-rays, the resulting neccessary long integration times and the folding over the periods without respect to the mixing of the X-ray states and their spectral characteristics, neither a high energy cut-off during the low hard nor a soft spectral index during the transitional state can be detected. A path for analysing forthcoming and existing data is given using radio spectral index data, and the first results of these analysis shown in Chapter 2 are quite promising.

The analysis in Zimmermann & Massi (2012) also revealed a number of clues corroborating a microblazar scenario, where the jet is pointed close to our line of sight. The correlation between X-rays and VHE observed by Anderhub et al. (2009) and its similarity to correlations seen in blazars fit into the scenario. A synchrotron component in the soft X-rays with a photon index comparable to that seen in the low hard state could explain the lack of a blackbody component during the transitional (steep power law) state. Furthermore, this component could be the origin of the very high component, creating it via external inverse Comptonization or synchrotron self-Comptonization. A microblazar scenario had been proposed before (Kaufman Bernado et al. 2002, Massi et al. 2004), due to the morphology seen in radio maps. The new findings now led to the re-analysis by Massi, Ros & Zimmermann (2012) of the longest existing VLBA data set of LS I +61°303, taken in 2006 by Dhawan and collaborators. The original maps showed a clear two-sided structure already in one of the ten maps, nevertheless the remaining nine maps with one-sided structures were taken as evidence for a pulsar scenario (Dhawan et al. 2006). In the re-analysis the dynamic range was improved with careful self-calibration, not applied before by Dhawan et al (2006). These re-analysis clearly revealed two-sided structures in additional four maps due to the increased signal-to-noise ratio of a factor four. Furthermore, the flux peak in these maps trace a clear ellipse in ~27 days. A microblazar model with a precessing jet can on the one hand explain the fast switches from one- to two-sided structures by variable Doppler boosting and on the other hand explains the ellipse via the core-shift effect of a precessing steady jet. The radio emission is further analysed with respect to the spectral characteristics. This shows again very nicely an optically thick outburst followed by an optically thin one. The analysis of the jet velocity by modelling the jet components gives a low velocity outflow with $\beta \cos\theta$ <0.65, compatible with the source not showing superluminal ejections (these can only be detected for β >0.73, not even reachable for θ=0). The re-analysis of this VLBA data set then not only corroborated again the microquasar model in general, but also in particular yielded a very strong argument for a precessing jet pointing close to our line of sight and even a first estimate of its precession period. Massi & Jaron (2013) then performed a timing analysis of the longest radio data base (6.7 yr of GBI data) and confirmed the existence of this period, 26.9 days, in the data. Even more, they found that this period together with the orbital period creates the observed long term period of 4.6 yr as a beat frequency, possibly solving this phenomenon, often attributed to periodic shell ejections from the Be star.

The radio spectral index was now established as a valuable instrument to investigate this high energy source. Inspecting the existing radio data sets, i.e., the GBI data, covering 6.7 yr at two frequencies and the VLBA data set, covering only one orbit, but at high resolution, it became clear that a dense monitoring of an orbit at several frequencies, yielding a broad-band radio spectrum, was still missing. This could now be used to disentangle precession and accretion events in LS I +61°303 and shed a light on the nature of the main outburst. Strickman et al (1998) reported on broad-band VLA observations, but the gaps in the data, especially during the flare, left too much room for speculation. Trushkin et al (2010) monitored the source at several frequencies with the RATAN-600 radio telescope, but again, the gaps between measurements were quite big, and, as seen from our observations, miss information on smaller time scales. To overcome the time sampling problem, LS I +61°303 was observed with the Effelsberg 100m telescope during an entire orbit, covering densely the radio outburst at several frequencies. The observations reveal that the main flare has a flat spectrum, which can be explained by a steady jet. The achromatic rise prefer precession as the origin. Nevertheless, the fast rise and the slow decay speak against precession and for accretion, which would yield a long adiabatic decay. Several substructures are seen in the flare. A small pre-flare with a similar spectrum as the main flare, and three subflares during the decay. These three subflares show different spectral characteristics then the main flare. Especially the last subflare exhibits an evolution reminiscent to those known from flares in blazars. It peaks first at the high frequencies with an inverted spectrum (Compton stage) and then at the lower frequencies, where the flux density rises even higher (synchrotron stage) (Marscher 2009, Tuerler 2011). Interestingly, this subflare is possibly correlated to a flux increase in the gamma-rays seen with the Fermi-LAT. The analysis prove that dense broad band radio monitoring is a useful tool to investigate the origin of the flares in LS I +61°303.

Now that it has become clearer that a microblazar scenario could apply for LS I +61°303, a comparison with extra-galactic sources, i.e., with blazars could also help understand the production of gamma-rays in microquasars. Blazars are very active in gamma-rays and monitored continuously with, e.g., Fermi-LAT. As shown in this thesis, multiwavelength campaigns for LS I +61°303 at high frequencies with the VLBA and Fermi-LAT and broad band spectral analysis with the Effelsberg 100m telescope and Fermi-LAT could give further information about the physical processes behind the outbursts and help identify the origin of the gamma-ray emission possibly discriminating between leptonic and hadronic models.

Bibliography

Abdo, A. A., et al. 2009, ApJ, 701, L123

Abdo, A. A., Ackermann, M., Ajello, M., et al. 2011, ApJL, 736, L11

Acciari, V. A., Aliu, E., Arlen, T., et al. 2009, ApJ, 700, 1034

Acciari, V. A., Aliu, E., Arlen, T., et al. 2011a, ApJ, 738, 169

Acciari, V. A., Aliu, E., Arlen, T., et al. 2011b, ApJ, 738, 3

Aharonian, F., et al. 2005, Science 309, 746

Aharonian, F., et al. 2009, A&A, 507, 389

Albert, J. et al. 2006, Science, 312, 1771

Albert, J., et al. 2009, ApJ, 693, 303

Aleksić, J., Alvarez, E. A., Antonelli, L. A., et al. 2012, ApJ, 746, 80

Anderhub, H., et al. 2009, ApJL, 706, L27

Aragona, C., McSwain, M. V., Grundstrom, E. D. et al. 2009, ApJ, 698, 514

Baars, J. W. M., Genzel, R., Pauliny-Toth, I. I. K., & Witzel, A. 1977, A&A, 61, 99

Belloni, T. M. 2010, Lecture Notes in Physics, Berlin Springer Verlag, 794, 53

Bondi, H. 1952, MNRAS, 112, 195

Bosch-Ramon, V. et al. 2006, A&A, 459, L25

Bosch-Ramon, V., Barkov, M. V., Khangulyan, D., & Perucho, M. 2012, A&A, 544, A59

Caballero-García, M. D., Miller, J. M., Trigo et al. 2009, ApJ, 692, 1339

Casares, J. et al. 2005, MNRAS, 360, 1105

Chernyakova, M., Neronov, A., & Walter, R. 2006, MNRAS, 372, 1585

Chernyakova, M., Neronov, A., Molkov, S., et al. 2012, ApJL, 747, L29

Connors, T. W. et al. 2002, MNRAS, 336, 1201

Corbel, S., Tomsick, J. A., & Kaaret, P. 2006, ApJ, 636, 971

Corbel, S., Koerding, E., & Kaaret, P. 2008, MNRAS, 389, 1697

Cornwell, T. & Fomalont, E. B. 1999, Synthesis Imaging in Radio Astronomy II, 180

Dhawan, V., Mioduszewski, A., & Rupen, M. 2006, Proceedings of the VI Microquasar Workshop, p. 52.1

Dubus, G. 2006, A&A, 456, 801

Fender, R., Spencer, R., Tzioumis, T., et al. 1998, ApJL, 506, L121

Fender, R. P., Belloni, T. M., & Gallo, E. 2004, MNRAS, 355, 1105

Fender, R., & Maccarone, T. 2004, Cosmic Gamma-Ray Sources, 304, 205

Fender, R. 2010, Lecture Notes in Physics, Berlin Springer Verlag, 794, 115

Fender, R., & Belloni, T. 2012, Science, 337, 540

Fomalont, E. B., & Perley, R. A. 1999, Synthesis Imaging in Radio Astronomy II, 180, 79

Frail, D.A., & Hjellming, R.M. 1991, AJ, 101, 2126

Fuhrmann, L. 2004, PhD Thesis, University Bonn

Fuhrmann, L., Krichbaum, T. P., Witzel, A., et al. 2008, A&A, 490, 1019

Gallo, E. 2010, Lecture Notes in Physics, Berlin Springer Verlag, 794, 85

Gregory, P. C., Peracaula, M., & Taylor, A. R. 1999, ApJ, 520, 376

Gregory, P. C. 2002, ApJ, 575, 427

Gregory, P. C., Neish, C. 2002, ApJ, 580, 1133

Grinberg, V. 2010, Diplomarbeit, ECAP

Grove, J. E., Johnson, W. N., Kroeger, R. A. et al. 1998, ApJ, 500, 899

Grundstrom, E. D., Caballero-Nieves, S. M., Gies, D. R., et al. 2007, ApJ, 656, 437

Gupta, S. & Boettcher, M. 2006, ApJL, 650, L123

Hadasch, D., Torres, D. F., Tanaka, T., et al. 2012, ApJ, 749, 54

Hada, K., Doi, A., Kino, M., et al. 2011, Nature, 477, 185

Harrison, F. A., Ray, P. S., Leahy, D.A., Waltman, E. B., & Pooley, G. G. 2000, ApJ, 528, 454

Heeschen, D. S., Krichbaum, T., Schalinski, C. J., & Witzel, A. 1987, AJ, 94, 1493

Hermsen, W., & Kuiper, L. 2007, in First GLAST Symposium

Hutchings, J. B., Crampton, D. 1981, PASP, 93, 486

Johnston, S., Lyne, A. G., Manchester, R. N., Kniffen, D. A., D'Amico, N., Lim, J., & Ashworth, M. 1992, MNRAS, 255, 401

Johnston, S., Ball, L., Wang, N., & Manchester, R. N. 2005, MNRAS, 358, 1069

Jonker, P. G., Nelemans, G., & Bassa, C. G. 2007, MNRAS, 374, 999

Kaufman Bernadó, M. M., Romero, G. E., & Mirabel, I. F. 2002, A&A, 385, L10

Katarzyński, K., et al. 2005, A&A, 433, 479

Katarzyǹski, K., Walczewska, K. 2010, A&A, 510, A63

Kraus, A., Krichbaum, T. P., Wegner, R., et al. 2003, A&A, 401, 161

Larwood, J. 1998, MNRAS, 299, L32

Lestrade, J.-F., Mutel, R. L., Preston, R. A., & Phillips, R. B. 1985, Radio Stars, 116, 275

Lestrade, J.-F., Preston, R. A., Jones, D. L., et al. 1999, A&A, 344, 1014

Li, J., Torres, D. F., Zhang, S., et al. 2013, IAU Symposium, 290, 255

Maraschi, L., Treves, A. 1981, MNRAS, 194, 1P

Markoff, S., Nowak, M. A., & Wilms, J. 2005, ApJ, 635, 1203

Markoff, S. 2010, Lecture Notes in Physics, Berlin Springer Verlag, 794, 143

Marscher, A. P. 1995, Proceedings of the National Academy of Science, 92, 11439

Marscher, A. P. 2009, arXiv:0909:2576

Marti, J., & Paredes, J. M. 1995, A&A, 298, 151

Marti, J., Peracaula, M., Paredes, J. M., Massi, M., & Estalella, R. 1998, A&A, 329, 951

Martí-Vidal, I. & J. M. Marcaide, J. M. 2008, A&A, 480, 289

Massi, M. 2007, The Multicolored Landscape of Compact Objects and Their Explosive Origins, 924, 729

Massi, M., Paredes, J.M., Estalella, R., & Felli, M. 1993, A&A, 269, 249

Massi, M., Ribó, M., Paredes, J. M., Peracaula, M., & Estalella, R. 2001, A&A, 376, 217

Massi, M. et al. 2004, A&A, 414, L1-L4

Massi, M., & Kaufman Bernadó, M. 2009, ApJ, 702, 1179

Massi, M., & Zimmermann, L. 2010, A&A, 515, A82

Massi, M. 2011a, Mem. Soc. Astron. It., 82, 24

Massi, M. 2011b, Mem. Soc. Astron. It., 82, 77

Massi, M., Ros, E., & Zimmermann, L. 2012, A&A, 540, A142

Massi, M., & Jaron, F. 2013, arXiv:1303.2007

McClintock, J. E., Remillard, R. A. 2004, arXiv:astro-ph/0306213v4

McClintock, J. E., & Remillard, R. A. 2006, Compact Stellar X-ray Sources, Cambridge University Press, p. 157

Mendelson, H., & Mazeh, T. 1994, MNRAS, 267, 1

Mirabel, I. F. 2006, Science, 312, 1759

Mirabel, I. F. 2010, Lecture Notes in Physics, Berlin Springer Verlag, 794, 1

Moldón, J. 2012, PhD Thesis, Universidad Barcelona

Ott, M., Witzel, A., Quirrenbach, A., et al. 1994, A&A, 284, 331

Paredes, J. M., et al. 1994, A&A, 288, 519

Paredes, J. M., Marti, J., Peracaula, M., & Ribo, M. 1997, A&A, 320, L25

Paredes, J. M., Massi, M., Estalella, R., & Peracaula, M. 1998, A&A, 335, 539

Peracaula, M., Gabuzda, D. C., & Taylor, A. R. 1998, A&A, 330, 612

Pottschmidt, K., Wilms, J., Nowak, M. A., et al. 2000, A&A, 357, L17

Pradel, N., Charlot, P., & Lestrade, J.-F. 2006, A&A, 452, 1099

Quirrenbach, A., Witzel, A., Kirchbaum, T. P., et al. 1992, A&A, 258, 279

Rickett, B. J. 1990, Annual Review A&A, 28, 561

Romero, G. E. et al. 2007, A&A, 474, 15

Russell, D. M., Fender, R. P., Hynes, R. I., Brocksopp, C., Homan, J., Jonker, P. G., & Buxton, M. M. 2006, MNRAS, 371, 1334

Shepherd, M. C. 1997, Astronomical Data Analysis Software and Systems VI, A.S.P. Conference Series Gareth Hunt and H. E. Payne, eds., 125, 77

Sidoli, L., Pellizzoni, A., Vercellone, S. et al. 2006, A&A, 459, 901

Strickman, M. S. et al. 1998, ApJ, 497, 419

Taylor, A. R., & Gregory, P. C. 1982, ApJ, 255, 210

Taylor, A. R., Kenny, H. T., Spencer, R. E., & Tzioumis, A. 1992, ApJ, 395, 268

Taylor, A.R., Dougherty, S.M., Scott, W.K., Peracaula, M., & Paredes, J.M. 2000, proc. of *Astrophysical Phenomena Revealed by Space VLBI*, eds. H. Hirabayashi, P.G. Edwards, and D.W. Murphy., pp. 223

Trushkin, S., & Nizhelskij, N. 2010, 38th COSPAR Scientific Assembly, 38, 2450

Tudose, V., Fender, R. P., Tzioumis, A. K., Spencer, R. E., & van der Klis, M. 2008, MNRAS, 390, 447

Tuerler, M. 2011, Mem. Soc. Astron. It, 82, 104

Ubertini, P., Lebrun, F., Di Cocco, G., et al. 2003, A&A, 411, L131

Vedrenne, G., Roques, J.-P., Schönfelder, V., et al. 2003, A&A, 411, L63

Winkler, C., Courvoisier, T. J.-L., Di Cocco, G., et al. 2003, A&A, 411, L1

Zamanov, R. K., Martí, J., Paredes, J. M., et al. 1999, A&A, 351, 543

Zamanov, R. K, & Martí, J. 2000, A&A, 358, L55

Zabalza, V., Paredes, J. M., & Bosch-Ramon, V. 2011, A&A, 527, A9

Zabalza, V., Bosch-Ramon, V., & Paredes, J. M. 2011, ApJ, 743, 7

Zdziarski, A. A., Neronov, A., & Chernyakova, M. 2010, MNRAS, 403, 1873

Zhang, S., Torres, D. F., Li, J. et al. 2010, MNRAS, 408, 642

Zimmermann, L., Grinberg, V., Massi, M., & Wilms, J. 2011, The X-ray Universe 2011, 308

Zimmermann, L., & Massi, M. 2012, A&A, 537, A82

Zimmermann, L., Massi, M., & Ros, E. 2012, American Institute of Physics Conference Series, 1505, 382

Acknowledgements

This work is partly supported by the German Excellence Initiative via the Bonn Cologne Graduate School and the International Max Planck Research School for Astronomy and Astrophysics. The Green Bank Interferometer is a facility of the National Science Foundation operated by the NRAO in support of NASA High Energy Astrophysics programs. The Very Long Baseline Array is operated by the National Radio Astronomy Observatory, a facility of the National Science Foundation operated under cooperative agreement by Associated Universities, Inc.